



Novel Liquid-Phase Synthesis of Two-Dimensional Transition Metal Compounds for Electrocatalytic Energy Conversion Applications

A thesis submitted in fulfilment of the requirements for the degree of Doctor of Philosophy

Md Mohiuddin

B.Sc. (Hons.) Industrial & Production Engineering, BUET, Bangladesh

M.Eng. Mechanical Engineering, Inha University, South Korea

School of Engineering

College of Science, Engineering and Health

RMIT University

September 2019

Declaration

I certify that except where due acknowledgement has been made, the work is that of the author alone; the work has not been submitted previously, in whole or in part, to qualify for any other academic award; the content of the thesis is the result of work which has been carried out since the official commencement date of the approved research program; any editorial work, paid or unpaid, carried out by a third party is acknowledged; and, ethics procedures and guidelines have been followed.

Md Mohiuddin

13 September 2019

Abstract

Ultrathin two-dimensional (2D) nanomaterials offer enormous potential from fundamental studies to applications owing to their unique properties. Among the wide range of 2D nanomaterials, layered semiconducting transition metal dichalcogenides (TMDs) and non-layered transition metal compounds are most promising due to their thickness-dependent properties. This PhD thesis explores the novel liquid-phase synthesis and fundamental properties of several most promising 2D transition metal layered and non-layered compounds and their potentials in electrocatalysis application. Overall, this thesis consists of four main studies.

The first part of this thesis explores the liquid-phase exfoliation technique of layered MoS₂ exploiting the piezoelectric nature, which leads to new opportunities for fast and efficient exfoliation processes. A surface acoustic wave (SAW) microcentrifugation device is utilised to apply concomitant electric field and mechanical shear force for the effective exfoliation of MoS₂ nanosheets. Using the developed exfoliation method, at least an order of magnitude larger overall yield per unit of time can be achieved than previously reported liquid-phase exfoliation methods. Simultaneously, the higher monolayer yield can also be achieved. Moreover, the effect of the electric field in increasing the efficiency of liquid-phase exfoliation is also demonstrated.

Second, in extension to the first study, an enhancement in the efficiency of agitative liquid-phase exfoliation of stratified WS₂ crystals under the influence of an electric field is studied. The exfoliation efficiency of WS₂ nanoflakes has successfully been increased by using co-applied alternating electric field and mechanical wave. The loss of centrosymmetry at the facial layers of WS₂, together with the matching between the dispersive component of this material and solvent that weakens the van der Waals forces, augment the exfoliation process. However,

this is not seen for MoS₂ and graphene. The outcomes provide the base for future investigations on the influence of electric field for the exfoliation of layered structures. As a proof-of-concept, the exfoliated 2D WS₂ nanosheets are evaluated for potential electrocatalytic hydrogen evolution reaction (HER).

Third, facile and scalable synthesis of ultrathin hematite using inexpensive and water-soluble template through annealing has been explored. 2D nanosheets with the thickness down to 1 nm and lateral dimension up to 5 μm is realised. Interestingly, the morphology can easily be transformed into anisotropic porous planar nanostructure by introducing the aging process. The lattice match growth of nanosheets and shape transformation to anisotropic nanostructure due to small lattice mismatch on the template is thoroughly examined and explained. Further, nanostructures are tested for possible electrocatalytic hydrogen production.

Finally, ultrathin nanostructures such as nanosheets, nanonets of iron phosphide (FeP) have successfully been synthesised from ultrathin hematite through one step phosphorisation. The nanostructures are explored as free-standing electrocatalysts considering their high electrochemically active surface area up to 20.5 mF cm^{-2} , which exhibit overpotential as low as 117 mV to achieve 10 mA cm^{-2} for hydrogen generation. The combination of ultrathin morphology and nanopores particularly in ultrathin FeP nanosheets are considered as key factors for high electrocatalytic activity.

Acknowledgement

It's been more than three years incredible journey, one of the best learning parts of my life so far. This thesis would not have been possible without the countless support and contributions of many wonderful individuals.

First and foremost, I would like to convey my sincere thanks to my research supervisors Dr. Jianzhen Ou, Dr. Nasir Mahmood, Dr. Amgad Rezk, Professor Kourosh Kalantar-zadeh and Dr. Torben Daeneke for the opportunity to undertake this exciting work and invaluable suggestions throughout all stages of this research, without their guidance and support, this PhD thesis would not have reached to the end.

I wish to acknowledge the support that I have received from all the members of the centre for advanced electronics and sensors (CADES) at RMIT University. To my friends and fellow colleagues, you have made my PhD journey memorable, Ali Zavabeti, Nitu Syed, Robi Datta, Nripen Dhar, Azmira Jannat, Farjana Haque, Kibret Messalea, Hareem Khan, Naresh Pillai, Turki Alkathiri, Muhammad Waqas Khan, Bao Yue Zhang, and Kai Xu.

I am also grateful to Professor Leslie Yeo for giving me access to Micro/Nanophysics Research Laboratory (MNRL) research facility at RMIT University and helping me by providing support to my first project. Special thanks to Professor Salvy Russo at RMIT University for helping me in performing the density functional theory (DFT) simulation.

Many appreciations to the state-of-the-art research facilities at RMIT University including the MicroNano Research Facility (MNRf), the RMIT Microscopy and Microanalysis Facilities (RMMF), and RMIT chemistry laboratories and I would like to thank the technical staffs, researchers and students in these facilities for all the help and support. My work would not have been possible without access to those research facilities and technical supports from them.

I would like to thank RMIT University for Australian postgraduate award (APA) and the top-up scholarship award through RMIT Vice-Chancellor's PhD Scholarship (VCPS) to pursue my postgraduate study and research.

Finally, I am very grateful to my parents and sisters for their great support. I would like to dedicate this work to my beloved wife, Samiha, for her unconditional love, encouragement and patience regardless of any situation throughout this PhD. No words could ever express my sincerest gratitude to my wife for taking care of me, our kid and everything while I was busy completing my work.

Table of contents

Declaration.....	ii
Abstract.....	iii
Acknowledgement	v
Table of contents.....	vii
List of tables.....	x
List of figures.....	xi
List of abbreviations	xvi
Chapter 1: Introduction	1
1.1 Background and motivation.....	1
1.2 Objectives	4
1.3 Outline of the thesis	5
References	6
Chapter 2: Literature review	9
2.1 Layered materials	9
2.1.1 2D TMDs	9
2.1.1.1 Structure of TMDs	10
2.1.1.2 Electronic, mechanical and optical properties.....	12
2.2 Non-layered materials.....	14
2.2.1 Structure and properties of hematite	15
2.2.2 Structure and properties of iron phosphide.....	16
2.3 Synthesis of 2D materials	17
2.3.1 Top-down synthesis	18
2.3.1.1 Micromechanical exfoliation.....	18
2.3.1.2 Liquid-phase exfoliation	19
2.3.2 Bottom-up synthesis.....	21
2.3.2.1 Chemical vapour deposition (CVD).....	21
2.3.2.2 Wet-chemical synthesis.....	22
2.4 Applications of 2D materials	25
2.4.1 Electronics and catalytic applications of 2D TMDs	25
2.4.2 Catalytic applications of iron compounds.....	26
References	28

Chapter 3: Liquid phase acoustic wave exfoliation of layered MoS ₂ : Critical impact of electric field in efficiency	46
3.1 Introduction	46
3.2 Experimental section	48
3.2.1 Fabrication of the SAW device.....	48
3.2.2 Preparation of PDMS reservoir.....	49
3.2.3 Sample preparation and characterisation	49
3.2.4 Computational methods	50
3.3 Results and discussion	51
3.4 Conclusions	66
References	67
Chapter 4: Exploring electric field assisted van der Waals weakening of stratified crystals ..	74
4.1 Introduction	74
4.2 Experimental section	75
4.2.1 Materials	75
4.2.2 Synthesis	75
4.2.3 Characterisations.....	75
4.2.4 Electrochemical measurements.....	76
4.3 Results and discussion	77
4.4 Conclusions	93
References	93
Chapter 5: Facile and scalable template-assisted synthesis of ultrathin hematite nanosheets and nanonets	98
5.1 Introduction	98
5.2 Experimental section	100
5.2.1 Materials	100
5.2.2 Preparation of nanosheets and nanonets	100
5.2.3 Characterisations.....	101
5.2.4 Electrochemical measurements.....	101
5.3 Results and discussion	102
5.4 Conclusions	112
References	113
Chapter 6: Ultrathin iron phosphide nanostructures towards hydrogen evolution reaction ..	117
6.1 Introduction	117
6.2 Experimental section	118

6.2.1 Materials	118
6.2.2 Synthesis	118
6.2.3 Characterisations.....	118
6.2.4 Electrochemical measurements.....	119
6.3 Results and discussion	120
6.4 Conclusions	130
References	130
Chapter 7: Conclusions and future work	134
7.1 Conclusions	134
7.1.1 Phase 1	134
7.1.2 Phase 2	135
7.1.3 Phase 3	136
7.1.4 Phase 4	136
7.2 Future work.....	137
7.3 List of publications	139

List of tables

Table 3-1 Comparison of exfoliation efficiency. Comparison of the exfoliation efficiency of MoS ₂ prepared in this work with that produced from selected other comparable single-step liquid exfoliation methods.	66
Table 4-1 Surface tension components of solvents and 2D materials.	83
Table 6-1 Comparison of the HER activity of free-standing single metal phosphide based electrocatalysts in acidic media (0.5 M H ₂ SO ₄).....	129

List of figures

Figure 2-1 Schematics of the three TMDs polytypes (2H, 3R and 1T) with lattice constant (a) 3.1-3.7Å and interlayer spacing of ~6.5Å ¹	11
Figure 2-2 Micromechanical exfoliation of graphene to ultrathin nanosheet from bulk crystal ⁷⁸	19
Figure 2-3 Mechanisms of the main liquid-phase exfoliation. (a) Ion intercalation. (b) Ion exchange. (c) Sonication-assisted exfoliation ⁷⁶	20
Figure 2-4 Schematic of the CVD process of MoS ₂ and WS ₂ ⁹⁵	22
Figure 2-5 The schematic shows the concept of soft template synthesis of ultrathin 2D metal oxide nanosheets on polymer surfactant ¹⁰²	23
Figure 2-6 Scheme illustrating the synthesis of α-Fe ₂ O ₃ nanosheets using hard template ¹⁰⁷ . ..	24
Figure 3-1 SAW device configuration. Details configuration of the developed microcentrifugation SAW device (offset). There are two IDTs, each composed of 20 electrode pairs. The imposed wavelength of SAW device is 200 μm; therefore, the operating frequency of the transducer was ~19.2 MHz. 20 parallel metal strips positioned behind the IDTs act as reflectors to increase energy efficiency.	48
Figure 3-2 Reflection coefficient of the developed SAW device. Reflection coefficient (S ₁₁) of developed device measured by vector network analyser (VNA). The device delivers best performance at ~19.2 MHz. Reflection coefficient in dB indicates only negligible amount of power has been reflected by the device at the resonance frequency, thus optimum device performance.	48
Figure 3-3 SEM of bulk MoS ₂ . SEM (taken at 30kV) of the bulk MoS ₂ which has 0.8 to 1.2 μm flakes size.	50
Figure 3-4 Illustration and photographs of microcentrifugation SAW devices. (A) Illustration of an asymmetric micro-exfoliation SAW device constituting the lithium niobate chip with a PDMS reservoir bonded onto it. The insets show the IDTs, reflectors and their dimensions. (B) Illustration of monolayer MoS ₂ structure. (C) Centred droplet aligned with a single IDT on the device giving rise to two stable acoustic streaming vortices in the droplet. (D) Azimuthal acoustic streaming circulation in the droplet as a consequence of the asymmetric positioning of the droplet confined in the reservoir, which is placed off-centre with respect to the two opposing IDTs.....	53

Figure 3-5 Characterisation of thickness distribution. Thickness distribution histograms of the exfoliated MoS ₂ nanoflakes, obtained from the AFM measurements, along with typical images and height profile at different SAW exposure durations of (A) 1 (B) 5 (C) 10 (D) 15 (E) 20 and (F) 25 min. It can be seen that the SAW exfoliation process requires at-least 25 min to produce monolayers of MoS ₂ nanoflakes effectively. M represents the median thickness in the resolution of 0.1 nm.	54
Figure 3-6 Microscopic characterisation of exfoliated nanoflakes. TEM images of the MoS ₂ nanoflakes exfoliated from bulk 2H-MoS ₂ for different SAW exposure durations. (A) 1 min (B) 5 min (C) 10 min (D) 15 min (E) HRTEM of the 20 min sample with corresponding SAED and TEM image represented in the inset. (F) HRTEM of the 25 min sample with TEM and SAED (inset).	56
Figure 3-7 Structural characterisation of exfoliated nanoflakes. (A) Raman spectra of the exfoliated MoS ₂ nanoflakes at different exfoliation durations. (B) Wavenumber difference of the E _{2g} ¹ and A _{1g} Raman modes as a function of SAW exposure time.	57
Figure 3-8 XPS of MoS ₂ . (A) Bulk powder and (B) 25 min SAW exfoliated samples. In both cases, carbon 1s peak located at 284.50 eV used as a reference to align the spectra.	58
Figure 3-9 TGA of 2D MoS ₂ flakes prepared after 25 min of SAW exfoliation in the presence of nitrogen gas. The final concentration was calculated at 400 °C.	59
Figure 3-10 Computational estimation and validation of exfoliation. (A) Illustration of centrosymmetric and non-centrosymmetric MoS ₂ layers. (B) The number of layers in the 25 min SAW exposed sample obtained from the AFM thickness distribution estimation compared with (C) exfoliation of 9-layer nanoflakes under the influence of electric field in the computational estimation.	60
Figure 3-11 Exfoliation from a 9 layer nanoflake through to a 1 layer. The possible pathways of exfoliation can proceed through 4 successive exfoliation steps (branch layers 1-4). No further exfoliation for even number nanoflakes (labelled in red in the diagram) is considered once created.	61
Figure 3-12 Comparison of shear force only exfoliation with electric field-assisted exfoliation. (A) AFM Thickness distribution histograms of MoS ₂ flakes (25 min) with (black) and without (red) the presence of electric field. Inset shows microcentrifugation SAW device coated with Au layer underneath the PDMS reservoir and device without any metallic layer. (B) Flakes lateral dimension histograms.	65
Figure 4-1 (a) SEM microstructure of the as-purchased bulk WS ₂ powder. (b) AFM thickness profile of a typical WS ₂ grain with the inset showing the AFM image.	77

Figure 4-2 Electric field-assisted liquid-phase exfoliation. (a) Schematic illustration of the experimental procedure for synthesising nanoflakes by liquid-phase exfoliation using simultaneous electric field and probe sonication. HDPE container is used to exfoliate 20 ml solution. (b) Assembled device and HDPE container, device is used to apply electric field has two concentric electrodes with a gap 7 mm between the electrodes. (c) Disassembled outer and inner electrodes.	78
Figure 4-3 (a, c) Exfoliated WS ₂ , MoS ₂ suspensions and (b, d) UV-vis spectra of exfoliated WS ₂ , MoS ₂ suspensions.	79
Figure 4-4 The concentrations of the WS ₂ suspensions for no field and with an applied electric field as a function of sonication time.	80
Figure 4-5 UV-vis spectra of exfoliated WS ₂ for different volume ratios of IPA and DI water.	81
Figure 4-6 (a) Images of the suspensions of exfoliated graphene. (b) UV-vis spectra of graphene.	83
Figure 4-7 AFM characterisation of the exfoliated nanoflakes. AFM thickness distribution histogram of (a) no field (b) 0.1 kV mm ⁻¹ and (c) 0.2 kV mm ⁻¹ and correspondent original AFM images shown in (c), (d) & (f), respectively. 50 randomly selected nanoflakes of each sample were analysed by AFM to obtain thickness distribution histogram, and <i>M</i> represents median number of layers.	84
Figure 4-8 TEM and HRTEM with visible crystalline spacing images of typical (a, b) no field, (c, d) 0.1 kV mm ⁻¹ , and (e, f) 0.2 kV mm ⁻¹ of 2D WS ₂ nanoflakes, respectively.	85
Figure 4-9 Lateral dimension distributions of 2D WS ₂ nanoflakes determined from TEM images: (a) no field (b) 0.1 kV mm ⁻¹ (c) 0.1 kV mm ⁻¹ . Here, <i>N</i> represents the number of nanoflakes for the construction of flakes distributions.	86
Figure 4-10 (a) Raman spectra of WS ₂ nanoflakes exfoliated with phonon vibrational modes indicated. Inset depicts the peak intensity ratio between 2LA (<i>M</i>) and A _{1g} modes as a function of electric field. (b) PL signal of the samples prepared on gold coated Si substrates. Peaks intensity increased with the introduction of electric field.	88
Figure 4-11 XRD patterns for bulk WS ₂ and exfoliated 2D WS ₂ nanoflakes.	89
Figure 4-12 Zeta potential spectra for WS ₂ nanoflakes for three samples: (a) no field (b) 0.1 kV mm ⁻¹ (c) 0.2 kV mm ⁻¹	90
Figure 4-13 Zeta potential spectra for WS ₂ nanoflakes for three samples: (a) no field (b) 0.1 kV mm ⁻¹ (c) 0.2 kV mm ⁻¹ after six months.	90

Figure 4-14 (a) LSV curves of bare CP, sonication only and electric field exfoliated WS ₂ in 0.5 M H ₂ SO ₄ and (b) the corresponding Tafel slopes.....	91
Figure 4-15 Cyclic voltammetry (CV) curves for (a) electric field-assisted exfoliated WS ₂ , (b) sonication only exfoliated WS ₂ in the region of 0.10 ~ 0.20 V vs. RHE at five different scan rates.....	92
Figure 4-16 Capacitive currents at 0.15 V vs RHE as a function of scan rate for nanosheets electric field-assisted and sonication only exfoliated WS ₂	92
Figure 5-1 (a) Iron precursor (b) precursor and template mixture (left-immediately after preparation, right – after aging).	100
Figure 5-2 (a) Schematic of the synthesis procedure of nanosheets, step I, FeOOH nanosheets were obtained by filtering the initially formed FeOOH on the template (FeOOH@template), step II, shows the annealing of FeOOH@template to form α -Fe ₂ O ₃ . (b) The optical image shows the liquid suspension of α -Fe ₂ O ₃	102
Figure 5-3 (a, b) low- resolution TEM and SEM images of FeOOH nanosheets, respectively. The inset of b shows the SAED of FeOOH nanosheets. (c) AFM image of the FeOOH nanosheets with corresponding (d) thickness profile.....	104
Figure 5-4 (a-c) low-, high-resolution TEM images, and SAED pattern of α -Fe ₂ O ₃ nanosheets, respectively. (d) AFM images of α -Fe ₂ O ₃ nanosheets with corresponding (e) thickness profile.	104
Figure 5-5 (a) STEM image along with (b-d) C, Fe and O elemental mapping of α -Fe ₂ O ₃ nanosheets, respectively. STEM EDS spectrum of α -Fe ₂ O ₃ nanosheets shown in the inset of a.	105
Figure 5-6 Structure and surface characterisations. XPS spectrum of nanosheets (a) Fe 2p (b) O 1s of FeOOH (c) O 1s of α -Fe ₂ O ₃ (d) XRD pattern of FeOOH, α -Fe ₂ O ₃	106
Figure 5-7 FTIR spectrum of FeOOH which matches with the of β phase of FeOOH.....	107
Figure 5-8 Schematic illustrations and TEM images of the time-dependent evolution of nanonet from nanosheet. (a) original nanosheet formed at the initial stage (b) over time voids start to form (indicated in red arrows) on the nanosheet (c) amount of void space increased with time (indicated in red arrows) leading to the formation of nanonet (d) nanonet from nanosheet completely evolved to nanonet.	108
Figure 5-9 (a, b) low- resolution TEM and SEM images of FeOOH nanonet, respectively. The inset of b shows the zoom view of FeOOH nanonets. (c) SAED of FeOOH nanonet. (d) AFM image of the FeOOH nanonet with corresponding thickness profile shown in the inset of d.	109

Figure 5-10 (a-c) low-, high-resolution TEM images, and SAED pattern of α -Fe ₂ O ₃ nanonets, respectively. (d) AFM images of α -Fe ₂ O ₃ nanonet with corresponding (e) thickness profile.	110
Figure 5-11 (a) STEM image along with (b-d) C, Fe and O elemental mapping of α -Fe ₂ O ₃ nanonet, respectively. STEM EDS spectrum of α -Fe ₂ O ₃ nanonet shown in the inset of a....	110
Figure 5-12 XPS spectrum of nanonets (a) Fe 2p (b) O 1s of FeOOH (c) O 1s of α -Fe ₂ O ₃	111
Figure 5-13 (a) Polarisation curves of FeOOH and α -Fe ₂ O ₃ nanostructures measured in acidic media, (b) and the corresponding Tafel slopes of α -Fe ₂ O ₃ nanostructures.	112
Figure 6-1 (a-c) low-, high-resolution TEM images, and SAED pattern of FeP nanosheets, respectively. (d) AFM images of FeP nanosheets with corresponding (e) thickness profile. The liquid suspension of FeP shown in the inset of a.	121
Figure 6-2 (a) STEM image along with (b-d) C, Fe and P elemental mapping of FeP nanosheet, respectively. STEM EDS spectrum of FeP nanosheets shown in the inset of a.	121
Figure 6-3 Structure and surface characterisations. XPS spectrum of FeP nanosheets (a) Fe 2p (b) P 2p (c) O 1s and (d) XRD pattern.	123
Figure 6-4 (a-c) low-, high-resolution TEM images, and SAED pattern of FeP nanonets, respectively. (d) AFM images of FeP nanonet with corresponding (e) thickness profile.	124
Figure 6-5 (a) STEM image along with (b-d) C, Fe and O elemental mapping of α -Fe ₂ O ₃ nanonet, respectively. STEM EDS spectrum of α -Fe ₂ O ₃ nanonet shown in the inset of a....	124
Figure 6-6 Nitrogen sorption isotherms and pore size distribution curves (inset) of FeP nanosheets and nanonets.	125
Figure 6-7 Electrochemical HER performances of FeP nanosheets and nanonets measured in acidic media. (a) Polarisation curves, (b) and their corresponding Tafel slopes, (c) Electrochemically active surface area as a function of scan rate of FeP nanosheets and nanonets, (d) The polarisation curve before and after the 15 h of stability test of FeP nanosheets.	126
Figure 6-8 EIS Nyquist plot, showing charge transfer resistance of FeP nanosheets and nanonets.	127
Figure 6-9 Cyclic voltammetry (CV) curves in 0.5 M H ₂ SO ₄ for (a) FeP nanosheets, (b) FeP nanonets in the region of 0.10~0.20 V vs. RHE at various scan rates.	128
Figure 6-10 Time-dependent HER current density of FeP (a) nanosheets (b) nanonets.	129

List of abbreviations

2D	Two-dimensional
AFM	Atomic force microscopy
Au	Gold
CVD	Chemical vapour deposition
DFT	Density functional theory
DI	Distilled water
DMF	N,N-dimethylformamide
EDLC	Electrical double-layer capacitor
EDX	Energy dispersive X-ray spectroscopy
Fe ₂ O ₃	Iron(III) oxide
FeOOH	Iron oxyhydroxide
FeP	Iron phosphide
FTIR	Fourier-transform infrared spectroscopy
HER	Hydrogen evolution reaction
HRTEM	High-resolution transmission electron microscopy
IPA	Isopropyl alcohol
MoS ₂	Molybdenum disulphide
N ₂	Nitrogen
PDMS	Polydimethylsiloxane
PL	Photoluminescence
SAED	Selected area electron diffraction
SAW	Surface acoustic waves
SEM	Scanning electron microscopy
SiO ₂	Silicon dioxide
TEM	Transmission electron microscopy
TGA	Thermal gravimetric analysis
TMDs	Transition metal dichalcogenides
TMPs	Transition metal phosphides
UV-Vis	Ultraviolet-visible
W	Tungsten
WS ₂	Tungsten disulphide
XPS	X-ray photoelectron spectroscopy
XRD	X-ray diffraction

Chapter 1

Introduction

1.1 Background and motivation

Isolation of two-dimensional (2D) graphene from its parent crystal graphite in 2004 by Novoselov and Geim triggered the intense research towards 2D materials which unlocked the enormous potential of ultrathin materials for electronics and energy applications¹. Such discovery advances the research on the synthesis, characterisation, and applications of carbon and non-carbon based intrinsic layered and non-layered 2D materials²⁻⁵. Apart from carbon-based materials, large range of compounds are also in the portfolio of 2D layered and non-layered materials including metal oxides, chalcogenides, and pnictogens. Such variations in the portfolio give rise to the diversities in unique properties for fundamental applications in electronics, optoelectronics and novel devices⁶⁻⁸.

The method of synthesis of 2D layered materials is particularly important due to the layer and size-dependent properties; therefore, numerous methods have been developed and investigated. Liquid-phase exfoliation is a promising method for scalable production of 2D materials. Unfortunately, the synthesis of 2D layered materials with a higher percentage of ultrathin layers in liquid media in a short period still remains a major challenge despite tremendous research efforts. Moreover, a complete understanding of the intrinsic properties of 2D semiconductors is needed in developing efficient synthesis methods. Thus, piezoelectricity of 2D transition metal dichalcogenides (TMDs) has become a recent significant area of interest, which emerges with the breaking of inversion symmetry in ultrathin layers unlike their bulk counterparts^{9, 10}. The mechanism of piezoelectric properties in ultrathin layers is extensively studied

theoretically and experimentally¹⁰⁻¹⁵. For instance, the development of novel optoelectronic devices exploiting the coupling between piezoelectricity and photogenerated carriers have been reported¹⁶; moreover, the tuning of the photoluminescence due to the strong piezoelectricity in molybdenum disulphide (MoS₂) through strain-induced electric fields by using SAW¹⁷ has also been investigated. Despite all the reports and the potential applications of piezoelectric properties in the area of 2D piezoelectric materials, no report has been demonstrated the utilisation of such intrinsic piezoelectric properties to expedite the exfoliation process and to obtain the higher percentage of ultrathin layers yield in liquid media using a microcentrifugation SAW device. Therefore, a major part of this thesis will investigate and understand the synthesis of 2D MoS₂ using SAW device exploiting the piezoelectric nature and the mechanism.

On the other hand, the synergy between the surface tension of layered materials and the solvent has a significant influence on the efficiency of agitation exfoliation¹⁸. While Shen et al. suggested that the closeness of the ratio of surface tension components (dispersive and polar components) play a more critical role in defining the effectiveness of liquid-phase exfoliation for a solvent¹⁹. It is suggested that the presence of small ionic entities in the solvent during the exfoliation process can increase the exfoliation rate²⁰. Instead of using any external insertions, the fundamentals of the exfoliation of MoS₂ and tungsten disulphide (WS₂) considering the match of surface tension dispersive component of layered material and exfoliation media under the simultaneous application of electric field and mechanical shear wave has not yet been carried out, and there is a need for research into the mechanisms of such system. Consequently, the knowledge gap regarding the practical aspects of utilising fundamental piezoelectric properties of ultrathin nanosheet for the exfoliation is necessary to improve the exfoliation efficiency. Thus, the exfoliation of piezoelectric 2D TMDs in the presence of an external

electric field by considering the surface tension component of solvent and exfoliated non-centrosymmetry layered materials will be investigated.

The individual layers are bonded weakly by van der Waals forces in layered materials; therefore, 2D ultrathin nanostructures can be obtained straightforwardly from intrinsically layered materials through well-established methods. However, such ultrathin structures are considerably complex to produce naturally non-layered materials due to the intrinsic three-dimensional bulk crystals structures⁵. High yield exfoliation is a prerequisite for many applications, particularly, energy storage and conversions^{21, 22}; therefore, there is a need for a large scale synthesis of non-layered 2D nanostructures through simple steps in a short period. The quest for large scale synthesis method is particularly important for the industrial-scale hydrogen production using electrode materials. Platinum (Pt)-based catalysts are best in performance towards low overpotential. Unfortunately, high cost and the earth scarcity of Pt made it difficult for the application of large-scale electrochemical energy conversion. Therefore, highly active, earth-abundant and stable catalysts are highly desirable for the electrochemical energy conversion.

Particularly, transition metal oxides and phosphides have widely been investigated due to effectiveness, low cost, and high stability. Unfortunately, the majority of those materials suffer from poor conductivity and insufficient active sites for the reaction. So far, various nanostructures have been developed to improve the reaction potential by increasing the edges and defect active sites. 2D ultrathin nanostructured materials are attractive as hydrogen evolution reaction (HER) catalysts due to abundant active sites and high surface-to-volume ratio exposed to the reaction. Wet-chemical synthesis of 2D materials are favourable for high yield synthesis, a long list of ultrathin non-layered 2D structures are favourable to synthesis using wet-chemical synthesis approaches^{4, 5, 23}. Despite many advantages, the conventional wet-chemical synthesis techniques (e.g. hydrothermal and solvothermal) suffer from some key

limitations, such as expensive instruments, associated process risk, slow growth rate etc. To circumvent the limitations of conventional methods, template synthesis could be an excellent alternative to provide facile and versatile way to prepare unique nanostructures. More specifically, unique advantages (e.g. inexpensive processing, simple steps) of the template can overcome the fundamental limitations and key challenges of conventional wet-chemical synthesis techniques. Exploiting the lattice matching between the template and target nanomaterials, the ultrathin nanostructures can be grown on the template. The application of this method to produce large -scale 2D hematite ($\alpha\text{-Fe}_2\text{O}_3$) and its conversion to iron phosphide (FeP) nanostructures is an important step towards hydrogen evolution energy conversion application.

1.2 Objectives

The main aim of this research is to develop novel synthesis methods and gain a fundamental understanding of the exfoliation of layered and non-layered nanostructured transitional metal compounds. Moreover, catalysts based on exfoliated nanostructures are designed and characterised for the potential electrocatalytic hydrogen production. To examine the feasibility of the proposed research, the key objectives of this thesis are listed as follows:

1. Investigating the exfoliation of MoS_2 in liquid media using SAW micro-exfoliation system and understanding the impact of the electric field on the exfoliation using a statistical/density functional theory model to explore a theoretical prediction.
2. Understanding and investigating the possible mechanism behind the synergistic role of electric field/solvent nature for exfoliation of target stratified crystals to provide critical guidance regarding the choice of parameters in the exfoliation procedure in the presence of an electric field.

3. Large-scale synthesis of 2D α -Fe₂O₃ nanostructures using the inexpensive template and investigating the underlying mechanisms.
4. Atomic replacement and morphological transformation of 2D α -Fe₂O₃ to 2D FeP.
5. Fabricating and characterising the electrodes based on WS₂, α -Fe₂O₃ and FeP for hydrogen evolution reaction.

1.3 Outline of the thesis

This thesis consists of seven chapters, and an outline of each chapter is presented as follows:

Chapter 2 presents a detailed review of recent relevant literature. More specifically, the chapter will present various synthesis technologies and the applications of 2D layered and non-layered materials, with particular focus on 2D MoS₂, WS₂, α -Fe₂O₃ and FeP.

Chapter 3 illustrates a new exfoliation technique for piezoelectric 2D MoS₂ using a microcentrifugation SAW device. Exfoliation efficiency and the quality of produced nanosheets have been analysed in detail at different times. Moreover, a theoretical calculation using density function theory has also been described to validate the experimental outcome.

Chapter 4 describes a facile synthesis of layered WS₂ in presence of mechanical shear wave and external electric field exploiting the piezoelectric properties and surface tension component. The exfoliated materials have extensively analysed using optical properties. The author thoroughly characterises the synthesised nanosheets. Based on the outcomes and analysis, the author provides a detailed mechanism describing the synthesis procedure. Finally, the electrocatalytic hydrogen evolution properties of WS₂ are presented.

Chapter 5 presents a facile and scalable synthesis of 2D α -Fe₂O₃ using an inexpensive template. The author provides a detailed growth mechanism and a full set of characterisation of nanostructured nanosheets and nanonets of α -Fe₂O₃. Moreover, the developed nanostructures have also been tested for electrocatalytic hydrogen production.

Chapter 6 outlines and extends the novel synthesis method stated in Chapter 5 by converting 2D α -Fe₂O₃ to FeP, furthermore, the author thoroughly characterises the synthesised FeP. Based on the outcomes and analysis, provides a detailed hydrogen evolution describing the possibility of fulfilling the future energy requirements.

In chapter 7, the concluding remarks and the brief direction for the extension of future studies will be presented based on the outcomes of this thesis.

References

1. Novoselov, K. S., Geim, A. K., Morozov, S. V., Jiang, D., Zhang, Y., Dubonos, S. V., Grigorieva, I. V., Firsov, A. A., Electric field effect in atomically thin carbon films. *Science* **2004**, 306 (5696), 666-669.
2. Hernandez, Y., Nicolosi, V., Lotya, M., Blighe, F. M., Sun, Z., De, S., McGovern, I. T., Holland, B., Byrne, M., Gun'Ko, Y. K., et al., High-yield production of graphene by liquid-phase exfoliation of graphite. *Nat. Nanotechnol.* **2008**, 3, 563.
3. Nicolosi, V., Chhowalla, M., Kanatzidis, M. G., Strano, M. S., Coleman, J. N., Liquid exfoliation of layered materials. *Science* **2013**, 340 (6139), 1226419.
4. Tan, C., Zhang, H., Wet-chemical synthesis and applications of non-layer structured two-dimensional nanomaterials. *Nat. Commun.* **2015**, 6, 7873.
5. Wang, F., Wang, Z., Shifa, T. A., Wen, Y., Wang, F., Zhan, X., Wang, Q., Xu, K., Huang, Y., Yin, L., et al., Two-dimensional non-layered materials: synthesis, properties and applications. *Adv. Funct. Mater.* **2017**, 27 (19), 1603254.
6. Wang, Q. H., Kalantar-Zadeh, K., Kis, A., Coleman, J. N., Strano, M. S., Electronics and optoelectronics of two-dimensional transition metal dichalcogenides. *Nat. Nanotechnol.* **2012**, 7, 699.

7. Huo, C., Yan, Z., Song, X., Zeng, H., 2D materials *via* liquid exfoliation: a review on fabrication and applications. *Sci. Bull.* **2015**, *60* (23), 1994-2008.
8. Choi, W., Choudhary, N., Han, G. H., Park, J., Akinwande, D., Lee, Y. H., Recent development of two-dimensional transition metal dichalcogenides and their applications. *Mater. Today* **2017**, *20* (3), 116-130.
9. Cui, C., Xue, F., Hu, W.-J., Li, L.-J., Two-dimensional materials with piezoelectric and ferroelectric functionalities. *NPJ 2D Mater. Appl.* **2018**, *2* (1), 18.
10. Wu, W., Wang, L., Li, Y., Zhang, F., Lin, L., Niu, S., Chenet, D., Zhang, X., Hao, Y., Heinz, T. F., et al., Piezoelectricity of single-atomic-layer MoS₂ for energy conversion and piezotronics. *Nature* **2014**, *514*, 470.
11. Duerloo, K.-A. N., Ong, M. T., Reed, E. J., Intrinsic piezoelectricity in two-dimensional materials. *J. Phys. Chem. Lett.* **2012**, *3* (19), 2871-2876.
12. Blonsky, M. N., Zhuang, H. L., Singh, A. K., Hennig, R. G., *Ab initio* prediction of piezoelectricity in two-dimensional materials. *ACS Nano* **2015**, *9* (10), 9885-9891.
13. Dong, L., Lou, J., Shenoy, V. B., Large in-plane and vertical piezoelectricity in janus transition metal dichalcogenides. *ACS Nano* **2017**, *11* (8), 8242-8248.
14. Lee, J.-H., Park, J. Y., Cho, E. B., Kim, T. Y., Han, S. A., Kim, T.-H., Liu, Y., Kim, S. K., Roh, C. J., Yoon, H.-J., et al., Reliable piezoelectricity in bilayer WSe₂ for piezoelectric nanogenerators. *Adv. Mater.* **2017**, *29* (29), 1606667.
15. Gupta, M. K., Lee, J.-H., Lee, K. Y., Kim, S.-W., Two-dimensional vanadium-doped ZnO nanosheet-based flexible direct current nanogenerator. *ACS Nano* **2013**, *7* (10), 8932-8939.
16. Wu, W., Wang, L., Yu, R., Liu, Y., Wei, S.-H., Hone, J., Wang, Z. L., Piezophototronic effect in single-atomic-layer MoS₂ for strain-gated flexible optoelectronics. *Adv. Mater.* **2016**, *28* (38), 8463-8468.

17. Rezk, A. R., Carey, B., Chrimes, A. F., Lau, D. W. M., Gibson, B. C., Zheng, C., Fuhrer, M. S., Yeo, L. Y., Kalantar-zadeh, K., Acoustically-driven trion and exciton modulation in piezoelectric two-dimensional MoS₂. *Nano Lett.* **2016**, *16* (2), 849-855.
18. Cunningham, G., Lotya, M., Cucinotta, C. S., Sanvito, S., Bergin, S. D., Menzel, R., Shaffer, M. S. P., Coleman, J. N., Solvent exfoliation of transition metal dichalcogenides: dispersibility of exfoliated nanosheets varies only weakly between compounds. *ACS Nano* **2012**, *6* (4), 3468-3480.
19. Shen, J., He, Y., Wu, J., Gao, C., Keyshar, K., Zhang, X., Yang, Y., Ye, M., Vajtai, R., Lou, J., et al., Liquid phase exfoliation of two-dimensional materials by directly probing and matching surface tension components. *Nano Lett.* **2015**, *15* (8), 5449-5454.
20. Wang, Y., Carey, B. J., Zhang, W., Chrimes, A. F., Chen, L., Kalantar-zadeh, K., Ou, J. Z., Daeneke, T., Intercalated 2D MoS₂ utilizing a simulated sun assisted process: reducing the HER overpotential. *J. Phys. Chem. C* **2016**, *120* (4), 2447-2455.
21. Chung, D. Y., Jun, S. W., Yoon, G., Kim, H., Yoo, J. M., Lee, K.-S., Kim, T., Shin, H., Sinha, A. K., Kwon, S. G., et al., Large-scale synthesis of carbon-shell-coated FeP nanoparticles for robust hydrogen evolution reaction electrocatalyst. *J. Am. Chem. Soc.* **2017**, *139* (19), 6669-6674.
22. Xiao, X., Yu, H., Jin, H., Wu, M., Fang, Y., Sun, J., Hu, Z., Li, T., Wu, J., Huang, L., et al., Salt-templated synthesis of 2D metallic MoN and other nitrides. *ACS Nano* **2017**, *11* (2), 2180-2186.
23. Vaughn, D. D., In, S.-I., Schaak, R. E., A precursor-limited nanoparticle coalescence pathway for tuning the thickness of laterally-uniform colloidal nanosheets: the case of SnSe. *ACS Nano* **2011**, *5* (11), 8852-8860.

Chapter 2

Literature review

In this thesis, the novel liquid-phase synthesis of several 2D transition metal compounds and relevant catalysis application will be explored; therefore, in this chapter, a brief literature review of unique properties, common synthesis methods and relevant electronics and catalytic application of the few most popular 2D layered and non-layered materials will be discussed. The Specific layered and non-layered 2D materials of interest in this thesis is molybdenum disulphide (MoS_2), tungsten disulphide (WS_2), hematite ($\alpha\text{-Fe}_2\text{O}_3$) and iron phosphide (FeP).

2.1 Layered materials

Layered materials are those that possess strong plane parallel covalent bonding but shows weak van der Waals interaction between adjacent planes in perpendicular direction. As such, a three-dimensional (3D) bulk MoS_2 crystal consists of weakly stacked ultrathin MoS_2 nanosheets. Due to weak van der Waals interaction between adjacent planes, layered materials can be exfoliated to desire thickness through simple exfoliation techniques. A large number of 2D layered materials have been studied extensively which includes 2D TMDs, graphene, hexagonal boron nitride etc. Considering the scope of this thesis, the layered materials of this thesis are narrowed down to 2D TMDs.

2.1.1 2D TMDs

TMDs represent a large family of layered materials, formed by three atom-thick layers where metal atom layers are sandwiched between two layers of chalcogen atoms (e.g. MoS_2 , WS_2)¹.

Each unit formula of TMDs can be described as MX_2 , where M stands for transition metal (e.g. Mo, W) and X is chalcogen (e.g. S, Se). Majority of the 2D TMDs exhibit direct bandgap in monolayer in contrast to their indirect bandgap in bulk crystal counterparts¹. When exfoliated to monolayer from bulk counterparts, unique properties evolve from the quantum confinement and surface effects due to the transition of indirect to direct bandgap. Atomically thin 2D TMDs are mechanically flexible; therefore, such properties make 2D TMDs very promising for the future electronics, optoelectronics and energy harvesting devices¹⁻³. In the remainder of this section, structural, electronics, optical properties and applications of two main members (MoS_2 and WS_2) of the TMDs will be elaborated.

2.1.1.1 Structure of TMDs

According to the stacking orders and arrangement of atoms, there are three polytypes of MX_2 (Figure 2-1): 2H (hexagonal symmetry, trigonal prismatic coordination, two layers in each repeat unit), 3R (rhombohedral symmetry, trigonal prismatic coordination, three layers in each repeat unit) and 1T (tetragonal symmetry, octahedral coordination, one layer in each repeat unit)¹. The electronic properties of TMDs vary with the polytypes, ranging from metallic to semiconducting¹.

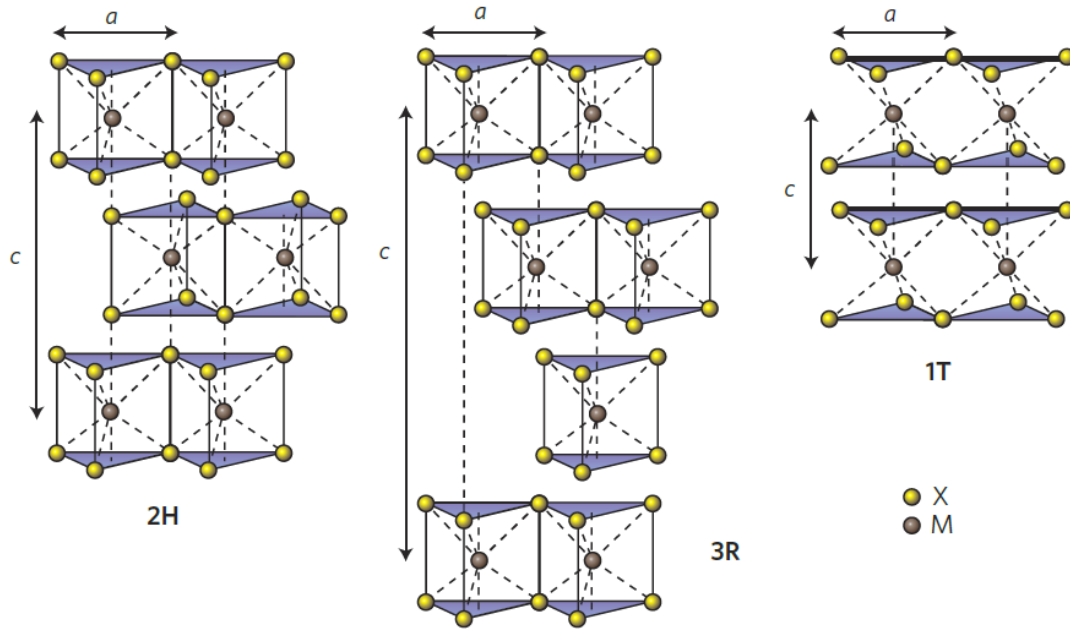


Figure 2-1 Schematics of the three TMDs polytypes (2H, 3R and 1T) with lattice constant (a) 3.1-3.7Å and interlayer spacing of $\sim 6.5\text{\AA}$.

Among the TMDs, MoS₂ considered most extensively studied in the research community due to its unique properties and multifunction applications. MoS₂ is proven to be effective in semiconductor, flexible electronics, biological, chemical and energy applications⁴⁻⁸. On the other hand, tungsten (W) is the heaviest transition metal⁹. Recently, W based compounds are also getting considerable attention due to the large W atom induced emerge of intrinsic properties compare to other TMDs. Except for the large atom, the lattice structure of WS₂ is similar to MoS₂. In compare to Mo, W is less toxic, more importantly, more abundant in the earth's crust⁹. Therefore, W is more favourable for numerous applications as well. Single-layer of MoS₂ or WS₂ consists of one metal (Mo/W) layer sandwiched between two S layers. In-plane atoms are covalently bonded whereas weak van der Waals forces exist in neighbouring layers. The thickness of single-layer MoS₂ is 0.65 nm which can be obtained in micro-mechanical exfoliation process¹⁰⁻¹². Similar to MoS₂, 1L of WS₂ has 0.65 nm thickness¹³. Hexagonal (H) structure of MoS₂ and WS₂ is generated by Mo/W and S atoms with a distance

of 0.23 nm⁷. Different morphologies of MoS₂ and WS₂ such as zero-dimensional (0D, e.g. quantum dots), one dimensional (1D, e.g. nanorods), two dimensional (2D, e.g. nanosheet) and three dimensional (3D, e.g. flower) can be obtained using different synthesis methods^{8, 14-19}.

2.1.1.2 Electronic, mechanical and optical properties

The transition from indirect to direct bandgap in the majority of TMDs is one of the key characteristics in 2D semiconducting form for electronic applications. Monolayer MoS₂ (WS₂) has direct band gap of 1.9 eV (2 eV), whereas more than 1L has indirect band gap^{18, 20, 21}. At room temperature, single-layer MoS₂ based top-gated (HfO₂) field-effect transistor (FET) device shows n-type semiconductivity with charge carrier mobility of ~200 cm²/V s²², where CVD grown WS₂ on SiO₂ has electron mobility in the range of 0.01–14 cm²/V s¹⁰. Numerous S vacancies in ultrathin WS₂ is found as n-type semiconductor^{23, 24}. WS₂ is also unique in terms of small effective mass, strong spin-orbit coupling, high third-order nonlinear susceptibility, and broadband light absorption²⁵⁻²⁹. However, doping of foreign element can effectively improve the charge carrier mobility as well as tune the properties to n or p-type semiconductor. As such, Re and Nb doping can module MoS₂ into n-type and p-type semiconductor, respectively^{30, 31}. Piezoelectricity in ultrathin TMDs is an excellent candidate for nanoenergy devices, flexible electronics and optoelectronics³². Piezoelectricity is an intrinsic property of non-centrosymmetric materials, generate electric output in response to an external mechanical force. The piezoelectric effect is a reversible process, the production of electricity when stress is applied (direct piezoelectric effect) and the production of stress and/or strain when an electric field is applied (converse piezoelectric effect). Piezoelectric materials are suitable for actuators, sensors, and energy harvesting systems^{33, 34}. 2D piezoelectric nanomaterials become popular due to ultrathin geometry and electromechanical conversion efficiency for promising applications in nanogenerator, nanoelectronics and smart robotics³⁵. Moreover, 2D

piezoelectric materials based energy harvester are crucial for future wireless nanosystems for environmental monitors, implantable medical sensors, and personal electronics. According to response direction, ultrathin piezoelectric materials can be divided into in-plane and out of plane piezoelectric materials³⁶. Piezoelectricity in 2D TMDs are predicted theoretically first time in 2012, and piezoelectric coefficient (d_{11}) of MoS₂ and WS₂ was predicted to be 3.73 and 2.19 pm V⁻¹, respectively³⁷. Experimental study of piezoelectricity in 2D MoS₂ is well documented so far than WS₂. Wu et al. demonstrated flexible MoS₂ piezoelectric nanogenerator energy harvester³². Interestingly, odd-layer MoS₂ which is an in-plane piezoelectric material does not have an inversion centre; therefore, such kind of noncentrosymmetric provides piezoelectric effect³², contrary, even-layer flakes no piezoelectric effect due to inversion symmetry³². Piezoelectricity of intrinsic non-piezoelectric materials can be tuned through certain doping by breaking the noncentrosymmetry³⁸. Han et al. and Lee et al. demonstrated MoS₂ and WSe₂ nanogenerator, respectively under mechanical vibration^{35, 39}.

Besides the electronics properties, TMDs, such as MoS₂ and WS₂ have excellent mechanical properties in terms of Young's modulus and pretension⁴⁰. Young's modulus of monolayer MoS₂ and WS₂ is ~270 GPa⁴¹. Moreover, monolayer MoS₂ and WS₂ have the pretension of 110 ± 40 and 150 ± 30 mN/m, respectively⁴¹.

Ultraviolet-visible (UV-vis), PL (photoluminescence), and Raman spectroscopy are common techniques to study the optical properties of 2D TMDs. In UV-vis, generally, two characteristic absorption peaks are observed in several semiconducting TMDs in between 500 to 900 nm known as A and B excitons which are associated with the energy split from valence band spin-orbital coupling^{42, 43}. Such as, A and B exciton absorption peaks are observed in monolayer MoS₂ at 670 nm and 627 nm respectively, in contrast, those peaks of 2D MoS₂ are not visible in bulk counterparts⁴². Moreover, bulk MoS₂ has an indirect bandgap of 1.3 eV and black in

colour due to the absorption of all visible light. However, with the decrease of number of layers and size, black colour of bulk MoS₂ changed to light yellow in N-Methyl-2-Pyrrolidone (NMP) solvent due to the widening of the band gap⁴⁴.

Raman spectroscopy is a non-destructive process which provides a convenient way to characterise 2D materials. For example, there are four first-order Raman active modes in MoS₂, namely, E_{1g} (286 cm⁻¹), E_{2g}¹ (383 cm⁻¹), A_{1g} (408 cm⁻¹), and E_{2g}² (32 cm⁻¹). E_{1g}, E_{2g}¹ and A_{1g} modes are vibrational modes within the S–Mo–S layer whereas only E_{2g}² mode is the result of the vibration of the adjoining rigid layers^{45, 46}. Raman active modes in WS₂ is similar to MoS₂⁴⁷. Interestingly, first-order Raman E_{2g}¹ and A_{1g} of MoS₂ and WS₂ are thickness-dependent modes and can be used to identify the layer number of ultrathin (4 or less number of layers) MoS₂ or WS₂ nanosheet^{45, 47}.

PL also emerges in semiconducting TMDs when exfoliating to ultrathin layers due to the transition from indirect to direct bandgap from bulk to monolayer⁴². For example, MoS₂ shows PL signal in single, double and trilayers⁴². Monolayer MoS₂ shows strong PL at 1.8 eV nm with a quantum yield of about 103 times of bulk, and the intensity of PL reduces proportionately with the increase of layer number; however, PL quantum yield of 1L WS₂ (6%) is higher than 1L MoS₂ (0.1%)⁴⁸. Optical properties of TMDs can be tuned by strain, ion interaction or doping⁴⁹⁻⁵¹. Moreover, optical properties of TMDs can also be manipulated by electrochemical ion intercalation between layers for potential bio-optical sensors or optical modulators or switches applications⁴⁹ and highly ion-doped MoS₂ induce plasmonic resonance in the visible and UV regions⁵¹.

2.2 Non-layered materials

Having strong in planes bond in layered materials, individual layers are bonded weakly by van der Waals forces; therefore, 2D ultrathin nanostructures can be obtained straightforwardly from

intrinsically layered materials through well-established methods; however, such ultrathin structures are considerably complex to produce for naturally non-layered materials due to the intrinsic three-dimensional bulk crystals structures^{52, 53}. Although having remarkable properties, non-layered materials have received relatively less attention compare to 2D layered materials. Owing to the diversified structural, chemical and physical properties, 2D non-layered materials are highly favourable for diversified applications. Similar to layered materials, 2D non-layered materials also exhibit unique properties in contrast to their bulk counterparts. Particularly, reduction in dimensional thickness, non-layered materials show applications in optics, electronics, sensors, catalysis, energy storage and conversion⁵⁴⁻⁵⁷.

Iron oxides and its compounds are one of the most fascinating and diversified groups of non-layered materials, which have been intensely investigated and are already employed in various fields^{58, 59}. Interestingly, iron oxides are present in various states such as ferromagnetic, ferrimagnetic, semiconductor⁶⁰. A significant portion of this PhD research will be based on hematite and iron phosphide for catalytic application; therefore, a brief review of this materials is presented in the sections below.

2.2.1 Structure and properties of hematite

Iron oxides are the most common form of iron found in nature. There are total six iron oxides, FeO (iron (II) oxide, wüstite, face-centred cubic), Fe₃O₄ (iron (II, III) oxide, magnetite, cubic) and four polymorphs of Fe₂O₃. The four polymorphs of Fe₂O₃ are α -Fe₂O₃ (Hematite, Rhombohedral), β -Fe₂O₃ (body-centred cubic), γ -Fe₂O₃ (Maghemite, Cubic), ϵ -Fe₂O₃ (Orthorhombic)⁶¹. Amongst, hematite is the most important due to natural abundance, environment friendliness, stable structure and electronic properties. Hematite is the most stable form of iron oxide in ambient condition and its an n-type semiconductor with a favourable bandgap of 1.8 eV in bulk which increases to ~2.2 eV for nanostructures^{56, 62}. Usually, bulk

hematite shows total seven Raman active phonon modes within 1000 cm^{-1} . The two peaks at 229 and 500 cm^{-1} represent A_{1g} modes, and other five peaks appear at 249 , 295 , 302 , 414 , and 615 cm^{-1} are assigned to the E_g modes⁶³. However, one weak peak at 660 cm^{-1} also been observed which believe to arise from disorder within the hematite crystal lattice⁶⁴. Interestingly, the intensity of first A_{1g} and second E_g modes are thickness dependent, the intensity ratio of these two peaks reduces with the reduction of thickness⁵⁶. Moreover, the position of A_{1g} modes redshift whereas E_g modes undergo blueshift when exfoliated to ultrathin hematite layers with respect to its bulk counterparts⁵⁶. The optical absorption bands of hematite spread between the near-infrared and UV region⁶⁵ and the absorption peak of the ultrathin structure shows blueshift in comparison to the bulk hematite⁵⁶. The Fourier transform infrared (FTIR) spectra of Fe–O bond stretching vibrations of hematite shows at 520 , and 433 cm^{-1} are the A_{2u}/E_u and E_u bands, respectively⁶⁶. Hematite is weakly ferromagnetic at room temperature; however, transit to an antiferromagnetic state at 265 K ⁵⁶. To date, considerable efforts have been made by the researchers to synthesis the nanostructures of hematite with different morphologies; therefore, 0D, 1D, 2D and 3D nanostructures of hematite have been successfully synthesised using various synthesis routes^{56, 67-69}.

2.2.2 Structure and properties of iron phosphide

Transition metal phosphides (TMPs) have attracted diversified applications owing to their excellent mechanical strength, stability and electronic conductivity, especially TMPs are promising alternates of the noble metal electrocatalysts. Properties of electrons and related mobility of such materials reformed accordingly when synthesised into nanostructures. Abundant active sites in nanostructures enhancing overall performance, moreover, hybridisation can also improve the performance. Low-band gap iron phosphides semiconductors are an interesting class of low cost, earth-abundant compound materials for magnetic, catalytic

and energy storage and conversion materials^{59, 70-73}. There are variety of phases of iron phosphide, such as Fe₂P, Fe₃P, FeP, FeP₂ etc. FeP is one of the most studied iron phosphides which has orthorhombic crystal structure and belongs to *Pna2₁* space group. Lattice constants of FeP are $a = 5.193$, $b = 5.792$ and $c = 3.099$ Å. The Curie temperature of FeP is about -58 °C and antiferromagnetic at 120 K⁷⁴. FeP is considered as a very good catalyst for HER process. The HER reaction mechanism generally consists of three steps⁷¹. In the first step, discharging of protons occurs on the electrode surface to form adsorbed hydrogen denoted as H_{ads}. This step is known as Volmer step ($H^+ + e^- \rightarrow H_{ads}$). If the coverage of H_{ads} on the catalyst surface is relatively low and the electrode surface has sufficient active sites, the adsorbed H atoms will preferably join with a proton and an electron simultaneously to evolve a H₂ molecule ($H_{ads} + H^+ + e^- \rightarrow H_2$). This is called the Heyrovsky reaction. However, if the coverage of H_{ads} is high then two adjacent H_{ads} will join together chemically and evolve to H₂. This is known as Tafel reaction. The H_{ads} on the cathode is always involved in the HER. In iron phosphide, localised partial negative charges on P centres attract protons and make their discharge step faster, promoting the HER easily⁵⁸. Besides trapping the protons by acting as a base, these P centres enhance the hydrogen desorption at high H_{ads} coverage⁵⁸. Phosphorus in iron phosphide not only act as a proton acceptor but also weaken the bond strength of metal part of iron phosphide to adsorbed hydrogen which is known as ensemble effect.

2.3 Synthesis of 2D materials

To attain the practical applications requirements, either high quality-large area or industrial-scale production of 2D materials are needed in a cost-effective way for various applications. So far, numerous methods have been devolved to synthesis of those materials including but not limited to mechanical exfoliation, liquid-phase exfoliation, chemical vapour deposition, wet-chemical etc^{52, 53, 75-79}. In general, synthesis methodologies of 2D materials can be divided into

two broad categories- top-down and bottom-up approaches. A brief description of both approaches with their pros and cons will be provided in subsequent sections.

2.3.1 Top-down synthesis

In the top-down approach, exfoliation of bulk crystals into ultrathin nanosheets can be achieved by external physical or chemical driving forces. In this section, a brief description will be provided on common top-down synthesis approaches.

2.3.1.1 Micromechanical exfoliation

Micromechanical exfoliation, mainly known as the scotch-tape method, is a simple way to exfoliate bulk stratified crystal into single- or few-layer^{22, 80}. In this method nanosheet produced on a substrate using sticky tapes where the starting material is bulk stratified crystal peeled off with the tape and pressed again the substrate; therefore, upon the release of the tape, part of the bulk crystal stays on the substrate due to the van der Waals attraction between materials and the substrate. Repeating the process produces ultrathin layers on the substrate. The exfoliation is performed by mechanically overcoming the interlayer weak van der Waals force by peeling off the layers of the initial bulk materials, the process can ultimately produce single atomic layer crystalline nanosheet, the procedure of micromechanical exfoliation is represented in Figure 2-2⁷⁸. Large area ultrathin sheet can be obtained using this method without compromising the intrinsic crystal structure and properties. Micromechanical exfoliation is very convenient, versatile and inexpensive for the fundamental understanding of 2D materials intrinsic properties. Unfortunately, micromechanical exfoliation is not scalable therefore not possible for industrial-scale production^{32, 81} and has less control over the lateral dimension and thickness of produced nanosheet. Moreover, the method is only applicable to stratified crystal; therefore, not suitable for non-layered materials.

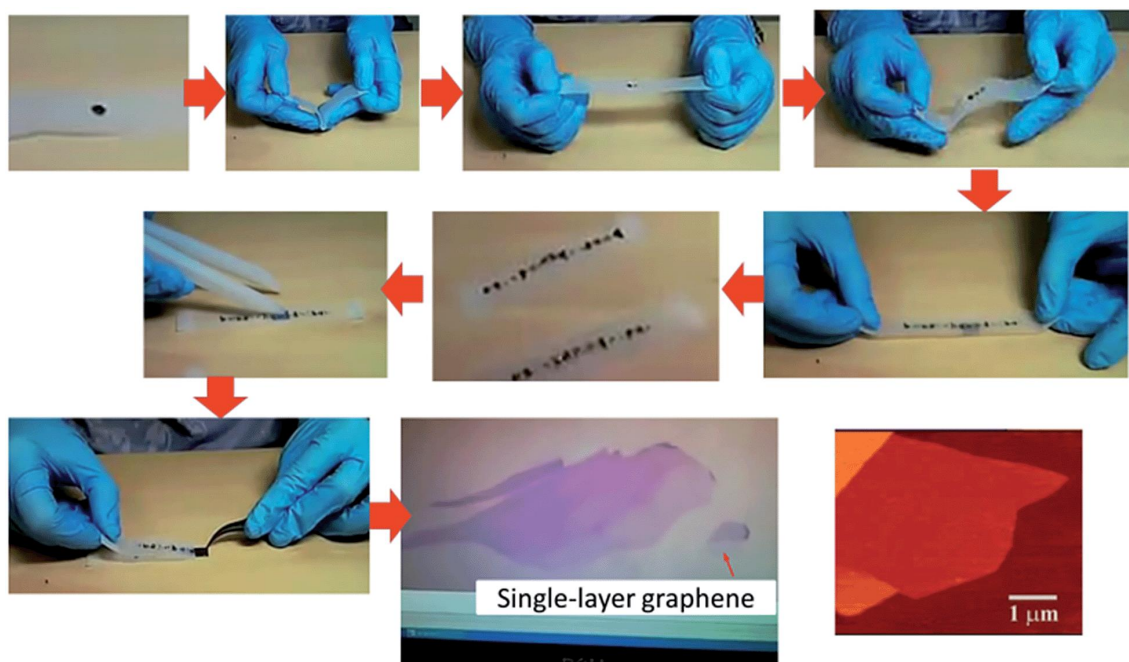


Figure 2-2 Micromechanical exfoliation of graphene to ultrathin nanosheet from bulk crystal⁷⁸.

2.3.1.2 Liquid-phase exfoliation

Liquid-phase exfoliation of layered bulk crystals is one of the most popular and established procedures to synthesise layered 2D materials in large-scale production and easy control the exfoliation parameters (Figure 2-3). Intercalation of lithium ions (Li^+) in layered crystals is effective for high-yield and large scale production of large range of TMDs (e.g. MoS_2 , TaS_2 , TiS_2 , WS_2 , ZrS_2 , NbSe_2 , WSe_2 , Sb_2Se_3 , Bi_2Te_3 , BN etc)^{76, 82}. Some intercalation process can lead to phase transformation resulting in different electronic properties, as such, intercalation of lithium ions in semiconducting 2H- MoS_2 transformed to metallic 1T- MoS_2 phase⁸³. Acid-based liquid-exfoliation also been developed for the exfoliation of MoS_2 and WS_2 nanosheets, which has an obvious advantage of processing using only air and water^{84, 85}. Moreover, exfoliation process can be optimised considering matching the surface tension components ratio between 2D materials and solvent^{15, 86}.

Solvent assisted exfoliation also a popular method for the preparation of 2D materials from bulk counterparts in solvent media by applying external mechanical wave (e.g. sonication).

Through the consistent energy input, the interlayer weak van der Waals of layered crystals allow to peeling-off to mono- and few layers. Many 2D layered materials such as graphene, MoS₂, WS₂, MoSe₂, MoTe₂, BN, Bi₂Te₃ can be exfoliated using this method^{87, 88}. Selecting a specific solvent is critical for solvent assisted exfoliation to minimise the surface energies for achieving efficient exfoliation outcome. Solvents with the surface energy of $\sim 40 \text{ mJ m}^{-2}$ are suitable for MoS₂ and WS₂⁸⁷. In addition to organic solvent, surfactants can also be incorporated to improve the stability of nanosheets in liquid media. Industrial-scale production along with low cost and process simplicity are the key advantages of liquid-phase exfoliation. Unfortunately, the lateral dimension of the liquid-phase exfoliation process is relatively small than mechanical exfoliation and induce defects in the produced nanosheets. Low yield of single layers and uncontrollable layer number in liquid-phase exfoliation sometimes outweigh the advantages for some specific applications (e.g. electronics). Moreover, the process uses various solvents, surfactant which are difficult to remove after the exfoliation.

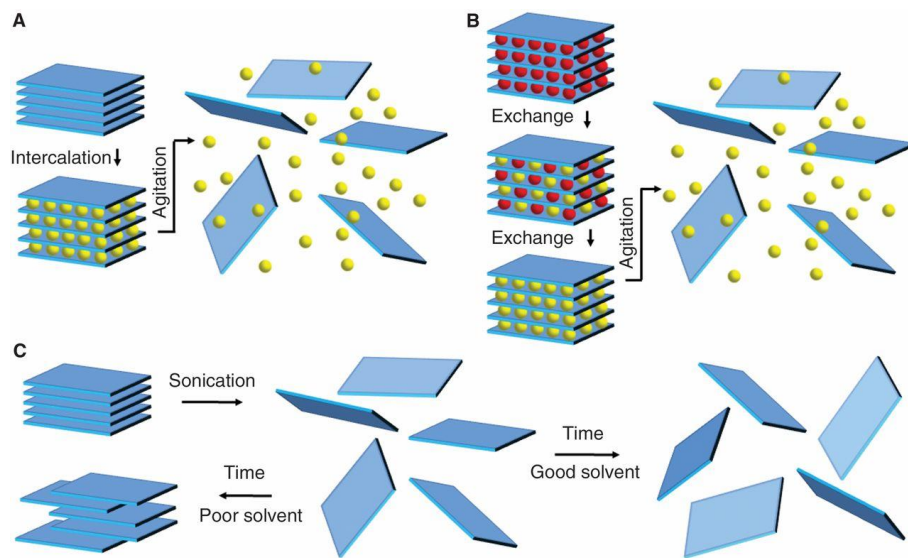


Figure 2-3 Mechanisms of the main liquid-phase exfoliation. (a) Ion intercalation. (b) Ion exchange. (c) Sonication-assisted exfoliation⁷⁶.

2.3.2 Bottom-up synthesis

The top-down approaches only applicable for layered bulk materials, consecutively, bottom-up approach is also widely used for the preparation of both layered and non-layered 2D materials. Chemical vapour deposition, wet-chemical, are widely used bottom-up synthesis approach of 2D materials.

2.3.2.1 Chemical vapour deposition (CVD)

Large area high-quality atomic thickness nanosheet and controlled morphology can be produced using CVD method through the control of different process parameters^{23, 89, 90}. CVD growth of 2D materials involves chemical reactions of precursors in a specially-designed environment under controlled conditions (Figure 2-4). Conditions like atmospheres, precursors, growth substrate are the key parameters to control the quality of the 2D materials. The precursors undergo pyrolysis followed by the reaction at vapour phase on the substrate which located in the hot zone of the reactor to form the nanosheet. For example, using CVD method single-layer MoS₂ nanosheet can be deposited on SiO₂ substrate at 850 °C using MoO₃ and S precursor powder⁹¹. Combining different precursors, 2D nanostructures, and their hybrids can easily be formed^{92, 93}. Moreover, synthesised nanosheets can easily be doped and functionalised only by introducing additional precursor⁹⁴. CVD process offers high-quality 2D materials with controllable thickness and properties. This method is suitable for large-area device fabrication but not suitable for energy applications where large volume is highly desirable. Limited pattern-ability of CVD method has been observed due to random nucleation on the substrate. Moreover, controlling stoichiometry and defects are also challenging in the growth of CVD method. Relatively complicated experiments and associated high cost for maintaining high temperature and vacuum are the few significant challenges in the CVD processes.

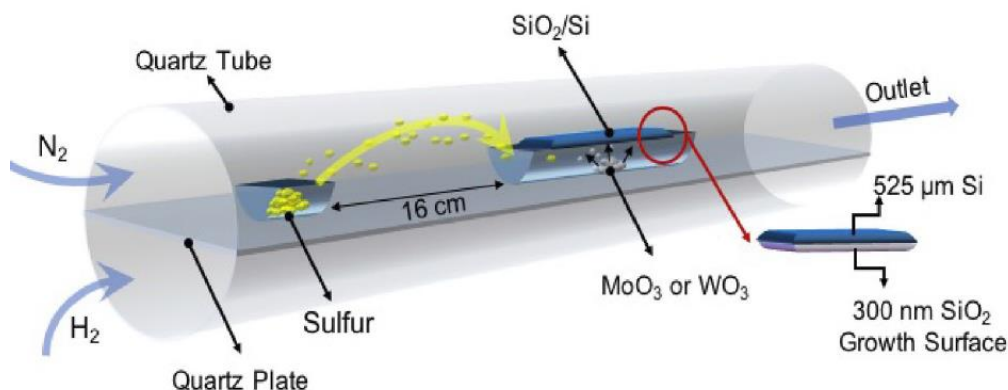


Figure 2-4 Schematic of the CVD process of MoS₂ and WS₂⁹⁵.

2.3.2.2 Wet-chemical synthesis

Wet-chemical synthesis is a common synthesis method for cost-effective and scalable synthesis of either layered or non-layered materials. Majority of the non-layer ultrathin structures (e.g. metals, metal chalcogenides, metal oxides) can be synthesised using wet-chemical synthesis methods^{52, 53}. High controllability of wet-chemical method is useful to produce controlled size and thickness for scalable industrial applications⁹⁶⁻⁹⁸. Nonlayered nanostructures cannot be prepared by top-down approaches thus wet-chemical is suitable for non-layered nanostructures. However, layered materials can also be prepared by wet-chemical^{99, 100}. Hydro/solvothermal synthesis and template synthesis are most common wet-chemical synthesis methods. Hydro/solvothermal method is generally suitable for synthesis inorganic materials at relatively low temperature (100 to 240 °C)¹⁰¹⁻¹⁰³. Conditions, like reaction temperature, growth time and reactants amounts are the key factors for the growth of nanostructures.

On the other hand, compared to the traditional (e.g. hydro/solvothermal) wet-chemical synthesis, template synthesis provides effective control to the synthesis of 2D materials. Template synthesis supports the growth of nanostructures which are confined by the template, subsequently template removed by either washing, heating or adjusting pH^{61, 104}. Various nanostructures such as 0D, 1D and 2D can be prepared by template method¹⁰⁴⁻¹⁰⁶. 2D materials

such as MoO_3 , Fe_2O_3 , CuInS_2 etc. can easily be synthesised by template method^{104, 107, 108}. The entire template synthesis method can generally be divided into three basic steps: first preparation of template then synthesis of nanostructures on the template and finally the removal of template. The template removal method is crucial and should be decided such a way so that the properties of the nanostructures remain unharmed. Based on the structure, template can be categorised into hard and soft templates.

Unrigid nanostructures formed by intramolecular interaction are the main basis of soft template method. The inorganic species are fashioned on the template-driven by weak non-covalent bonds (e.g. hydrogen bonds, van der Waals forces etc.) to form specific nanostructures shape and size (Figure 2-5). Surfactants, polymers, biopolymers are the common types of soft template. As an example, Wang et al. synthesised large area nanometre thick single-crystalline ZnO using surfactant monolayers which serve as soft templates. Unlike hard template which is needed to prepare before the reaction, soft template form within the reaction process. Therefore, soft templates are easy to remove without any complex post-processing.

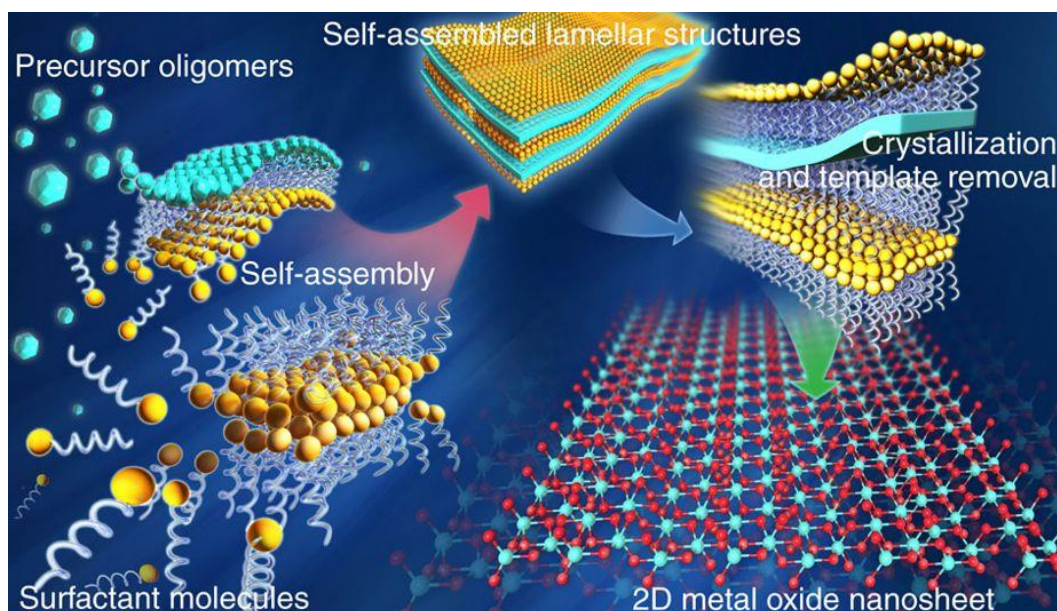


Figure 2-5 The schematic shows the concept of soft template synthesis of ultrathin 2D metal oxide nanosheets on polymer surfactant¹⁰².

Contrary, hard templates are solid structures and can control the produced nanostructures precisely. The structures of hard templates are less sensitive to the solution environment; therefore, the overall stability of hard templates is better in comparison to soft templates. Graphene oxide (GO), copper oxide (CuO), silicon dioxide (SiO₂), calcium carbonate (CaCO₃) are few popular choices of hard templates. For example, template-assisted oriented growth strategy was utilised to prepare ultrathin (0.59 nm) nanosheets of α -Fe₂O₃ on a CuO hard template (Figure 2-6)¹⁰⁷. Despite all advantages, the majority of the hard templates are difficult to remove and often involve complex processing and harsh chemicals. Difficulties of typical hard templates can be avoided by using salt templates. Salt templates (e.g. NaCl, KCl) are inexpensive, reusable, can be used for scalable large-area 2D materials synthesis and more importantly, templates can be removed easily simply by washing without using any expensive process and harsh chemicals. Nanomaterials are grown on the surface of salt template through lattice matching between the template and the target materials. So far, 1D nanorods, 2D ultrathin nanosheets, 3D porous architecture have been successfully prepared using salt template method^{104, 109-111}. In general, wet-chemical synthesis methods are processed in the solution; therefore, high production yield can be achieved in short period of time. Some wet-chemical synthesis methods require high temperature and long processing time.

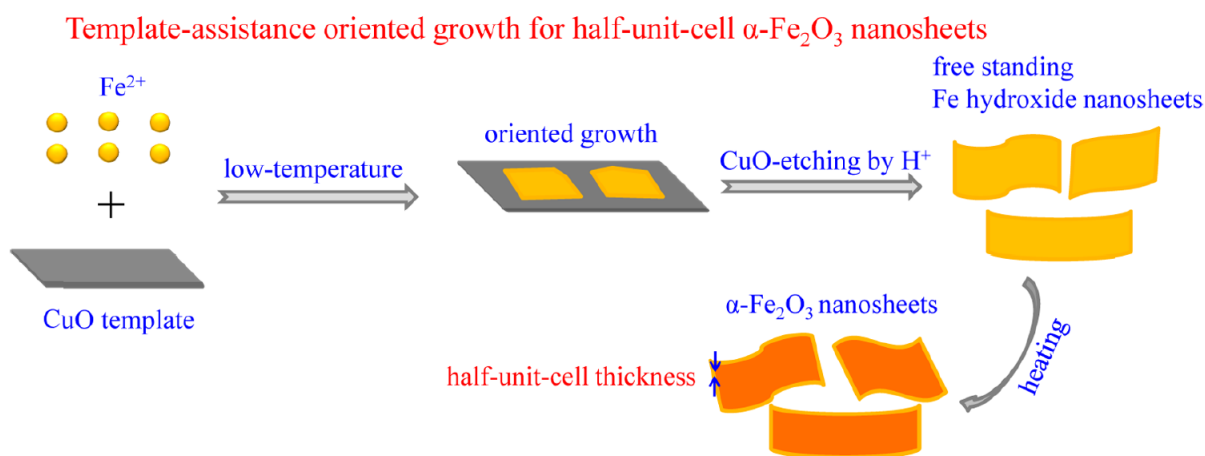


Figure 2-6 Scheme illustrating the synthesis of α -Fe₂O₃ nanosheets using hard template¹⁰⁷.

2.4 Applications of 2D materials

Due to the unique morphologies and electronic structures, 2D materials are suitable for various applications. In this section, the relevant electronic and catalytic application of 2D MoS₂, WS₂, hematite and iron phosphide have been summarised.

2.4.1 Electronics and catalytic applications of 2D TMDs

So far, MoS₂ has demonstrated the application in numerous fields, such as FETs, sensors/biosensors, catalysts etc^{4, 5, 7}. Integrated 2D morphology and tunable bandgap of 2D MoS₂ made it attractive for low-power photodiodes and phototransistors¹¹². Layered corresponding bandgap energies of MoS₂ 1L, 2L are suitable for green light detection, and 3L can be used for red light detection¹¹³. A typical 1L back gated MoS₂ FET shows n-type semiconductivity with charge carrier mobility of 0.5 to 3 cm² V⁻¹ s⁻¹ at room temperature²². However, with the addition of high-k dielectric material can enhance the charge carrier mobility and transport characteristics¹⁰. Moreover, doping can also enhance the transport characteristics properties of MoS₂³⁰. Unique photon–electron interaction of the direct bandgap 1L MoS₂ shows versatile characteristics under external illumination. Such that, under super-band gap illumination, single-layer MoS₂ phototransistors show photoresponsivity of 7.5 mA W⁻¹ up to 880 A W⁻¹ on-off ratio of 10³ and switching time of 50 ms which is six orders of magnitude higher than that of graphene^{17, 114}. Due to the direct bandgap of monolayer, MoS₂ monolayer exhibits photoconductivity whereas no photocurrent is observed other than monolayer due to indirect band gap¹¹⁵. In addition to electronics and optoelectronics devices, 1T metallic MoS₂ has significant application as electrocatalysts for the HER due to the superior catalytic activity and effective charge transport along the edge and basal planes, whereas 2H-MoS₂ has only active along the edges^{116, 117}. Photoelectrochemical conversion of MoS₂ is suitable for sensing based on the measurement of photogenerated charge carriers which is sensitive to the presence of an analyte¹¹⁸.

Similar to MoS₂ and other TMDs, WS₂ provide active sites for catalytic reactions, those active sites are located at the edges and absent in basal plane. The low charge transfer resistance at the electrode/electrolyte interface of metallic 1T phase WS₂ has higher electrocatalytic activity and strong supercapacitor performance than the 2H phase¹¹⁹⁻¹²³. Electrochemical accessibility is an important factor for the battery performance, ultrathin WS₂ is a potential candidate for the anode of lithium-ion batteries as the electrochemical accessibility of the diffusion channels are located along with the 2D layers in WS₂^{124, 125}. WS₂ has potentially been reported for sensors (e.g. bio, gas sensors) as well. WS₂ exhibits good selectivity and sensitivity for the detection of ethanol and ammonia. Probably the Lewis acidity on the surface of ultrathin WS₂ due to the presence of sulphide species responsible for the chemical response of ammonia¹²⁶. Owing covalent-network, 2D WS₂ also been employed as an active material for the immobilisation of biospecies for designing biosensors¹²⁷⁻¹²⁹. Apart from energy conversion and storage applications, owing to both semiconducting and catalytic properties, WS₂ has also been proved effective for photocatalytic water splitting, pollution photodegradation^{130, 131}. Quantum dots of WS₂ has excellent blue photoluminescence performance, moreover, tuning the luminescence properties also possible by combining some other photoactive materials^{132, 133}.

2.4.2 Catalytic applications of iron compounds

Nanostructure hematite is a promising candidate for photoelectrochemical cells, sensors, catalysts etc^{56, 68, 134, 135}. Favourable visible light absorption and chemical stability made hematite one of the most promising candidate for photoelectrochemical (PEC) photoanodes. However, the solar-to-hydrogen conversion efficiency of hematite is limited due to the short lifetime of photo-generated charge carriers, poor conductivity and the short hole diffusion length¹³⁶. Valance band position of hematite is favourable for water oxidation, but the conduction band is too low for water reduction to hydrogen production; therefore, large external bias is needed

for water splitting using hematite. Doping of hematite with a foreign element (e.g. Sn, Ti, Si) can lower the external bias significantly. For instance, Ti-doped hematite improving the photocurrent density and incident photon to current conversion efficiency at lower bias voltages¹³⁷. Moreover, induced defects in hematite can enhancement in photoelectrochemical performance as well. As such, Yang et al. reported the oxygen vacancies to improve the carrier generation of hematite¹³⁸.

Nanostructures of iron phosphides are not only low-cost, earth abundance non-noble metal, but also has a superior electrocatalytic activity for hydrogen and oxygen evaluation¹³⁹⁻¹⁴¹. The catalytic activity in hydrogen and oxygen evolution process is evaluated by overpotentials at fixed current density, Tafel slope, turnover frequency, and the Gibbs free energy of hydrogen adsorption. Various nanostructures such as nanowires, nanoparticles, nanotubes, nanosheets, nanorods etc. of iron phosphides have been investigated for electrocatalysts^{70, 104, 139, 141-144}. It has been reported that the HER activity of most popular TMPs follows the order $\text{FeP} > \text{CoP} > \text{MoP} > \text{WP} \approx \text{Ni}_2\text{P}$ at similar conditions (e.g. mass loading, similar synthesis method)⁵⁸. Iron phosphide with higher P content could enhance HER activity with more active sites; however, the increase of P content beyond a certain threshold reduces the HER activity by restraining the metal atoms electron delocalisation¹⁴⁵. In extend to P content, FeP grown on a substrate has better HER activity than free-standing FeP due to the superior charge transfer resulting from better adhesion of the catalyst to the substrate¹⁴⁶. Encapsulating the naked species of FeP with carbon not only ensures accelerating charge and the mass transport process but also protect the FeP from degradation and agglomeration¹⁴⁰. Moreover, doping of foreign elements, multimetal or hybrid complex of iron phosphides have also been explored and proven to be effective to enhance the overall electrocatalytic performance^{140, 145, 147-149}. For instance, Lu et al. systematically doped Ni into carbon hybridised FeP to obtain high HER performance and superior stability over the full pH range¹⁴⁸.

References

1. Wang, Q. H., Kalantar-Zadeh, K., Kis, A., Coleman, J. N., Strano, M. S., Electronics and optoelectronics of two-dimensional transition metal dichalcogenides. *Nat. Nanotechnol.* **2012**, 7, 699.
2. Chhowalla, M., Shin, H. S., Eda, G., Li, L.-J., Loh, K. P., Zhang, H., The chemistry of two-dimensional layered transition metal dichalcogenide nanosheets. *Nat. Chem.* **2013**, 5, 263.
3. Choi, W., Choudhary, N., Han, G. H., Park, J., Akinwande, D., Lee, Y. H., Recent development of two-dimensional transition metal dichalcogenides and their applications. *Mater. Today* **2017**, 20 (3), 116-130.
4. Song, I., Park, C., Choi, H. C., Synthesis and properties of molybdenum disulphide: from bulk to atomic layers. *RSC Adv.* **2015**, 5 (10), 7495-7514.
5. Wang, H., Li, C., Fang, P., Zhang, Z., Zhang, J. Z., Synthesis, properties, and optoelectronic applications of two-dimensional MoS₂ and MoS₂-based heterostructures. *Chem. Soc. Rev.* **2018**, 47 (16), 6101-6127.
6. Ou, J. Z., Chrimes, A. F., Wang, Y., Tang, S.-y., Strano, M. S., Kalantar-zadeh, K., Ion-driven photoluminescence modulation of quasi-two-dimensional MoS₂ nanoflakes for applications in biological systems. *Nano Lett.* **2014**, 14 (2), 857-863.
7. Li, X., Zhu, H., Two-dimensional MoS₂: properties, preparation, and applications. *J Materiomics* **2015**, 1 (1), 33-44.
8. Yadav, V., Roy, S., Singh, P., Khan, Z., Jaiswal, A., 2D MoS₂-based nanomaterials for therapeutic, bioimaging, and biosensing applications. *Small* **2019**, 15 (1), 1803706.
9. Eftekhari, A., Tungsten dichalcogenides (WS₂, WSe₂, and WTe₂): materials chemistry and applications. *J. Mater. Chem. A* **2017**, 5 (35), 18299-18325.

10. Radisavljevic, B., Radenovic, A., Brivio, J., Giacometti, V., Kis, A., Single-layer MoS₂ transistors. *Nat. Nanotechnol.* **2011**, *6*, 147.
11. Berkdemir, A., Gutiérrez, H. R., Botello-Méndez, A. R., Perea-López, N., Elías, A. L., Chia, C.-I., Wang, B., Crespi, V. H., López-Urías, F., Charlier, J.-C., et al., Identification of individual and few layers of WS₂ using Raman Spectroscopy. *Sci. Rep.* **2013**, *3*, 1755.
12. McCreary, K. M., Hanbicki, A. T., Singh, S., Kawakami, R. K., Jernigan, G. G., Ishigami, M., Ng, A., Brintlinger, T. H., Stroud, R. M., Jonker, B. T., The effect of preparation conditions on Raman and photoluminescence of monolayer WS₂. *Sci. Rep.* **2016**, *6*, 35154.
13. Wang, Z., Su, Q., Yin, G. Q., Shi, J., Deng, H., Guan, J., Wu, M. P., Zhou, Y. L., Lou, H. L., Fu, Y. Q., Structure and electronic properties of transition metal dichalcogenide MX₂ (M = Mo, W, Nb; X = S, Se) monolayers with grain boundaries. *Mater. Chem. Phys.* **2014**, *147* (3), 1068-1073.
14. Wu, Y.-c., Liu, Z.-m., Chen, J.-t., Cai, X.-j., Na, P., Hydrothermal fabrication of hyacinth flower-like WS₂ nanorods and their photocatalytic properties. *Mater. Lett.* **2017**, *189*, 282-285.
15. Shen, J., He, Y., Wu, J., Gao, C., Keyshar, K., Zhang, X., Yang, Y., Ye, M., Vajtai, R., Lou, J., et al., Liquid phase exfoliation of two-dimensional materials by directly probing and matching surface tension components. *Nano Lett.* **2015**, *15* (8), 5449-5454.
16. Xu, S., Li, D., Wu, P., One-pot, facile, and versatile synthesis of monolayer MoS₂/WS₂ quantum dots as bioimaging probes and efficient electrocatalysts for hydrogen evolution reaction. *Adv. Funct. Mater.* **2015**, *25* (7), 1127-1136.
17. Lopez-Sanchez, O., Lembke, D., Kayci, M., Radenovic, A., Kis, A., Ultrasensitive photodetectors based on monolayer MoS₂. *Nat. Nanotechnol.* **2013**, *8*, 497.

18. Jo, S., Ubrig, N., Berger, H., Kuzmenko, A. B., Morpurgo, A. F., Mono- and bilayer WS₂ light-emitting transistors. *Nano Lett.* **2014**, *14* (4), 2019-2025.
19. Tang, G., Tang, H., Li, C., Li, W., Ji, X., Surfactant-assisted hydrothermal synthesis and characterization of WS₂ nanorods. *Mater. Lett.* **2011**, *65* (23), 3457-3460.
20. Jiang, H., Electronic band structures of molybdenum and tungsten dichalcogenides by the GW approach. *J. Phys. Chem. C* **2012**, *116* (14), 7664-7671.
21. Elías, A. L., Perea-López, N., Castro-Beltrán, A., Berkdemir, A., Lv, R., Feng, S., Long, A. D., Hayashi, T., Kim, Y. A., Endo, M., et al., Controlled synthesis and transfer of large-area WS₂ sheets: from single layer to few layers. *ACS Nano* **2013**, *7* (6), 5235-5242.
22. Novoselov, K. S., Jiang, D., Schedin, F., Booth, T. J., Khotkevich, V. V., Morozov, S. V., Geim, A. K., Two-dimensional atomic crystals. *Proc. Natl. Acad. Sci. U.S.A.* **2005**, *102* (30), 10451-10453.
23. Gutiérrez, H. R., Perea-López, N., Elías, A. L., Berkdemir, A., Wang, B., Lv, R., López-Urías, F., Crespi, V. H., Terrones, H., Terrones, M., Extraordinary room-temperature photoluminescence in triangular WS₂ monolayers. *Nano Lett.* **2013**, *13* (8), 3447-3454.
24. Shang, J., Shen, X., Cong, C., Peimyoo, N., Cao, B., Eginligil, M., Yu, T., Observation of excitonic fine structure in a 2d transition-metal dichalcogenide semiconductor. *ACS Nano* **2015**, *9* (1), 647-655.
25. Zhang, W., Huang, Z., Zhang, W., Li, Y., Two-dimensional semiconductors with possible high room temperature mobility. *Nano Res.* **2014**, *7* (12), 1731-1737.
26. Zhu, Z. Y., Cheng, Y. C., Schwingenschlögl, U., Giant spin-orbit-induced spin splitting in two-dimensional transition-metal dichalcogenide semiconductors. *Phys. Rev. B* **2011**, *84* (15), 153402.

27. Li, S., Wang, S., Tang, D.-M., Zhao, W., Xu, H., Chu, L., Bando, Y., Golberg, D., Eda, G., Halide-assisted atmospheric pressure growth of large WSe₂ and WS₂ monolayer crystals. *Appl. Mater. Today* **2015**, *1* (1), 60-66.
28. Lee, Y.-H., Yu, L., Wang, H., Fang, W., Ling, X., Shi, Y., Lin, C.-T., Huang, J.-K., Chang, M.-T., Chang, C.-S., et al., Synthesis and transfer of single-layer transition metal disulfides on diverse surfaces. *Nano Lett.* **2013**, *13* (4), 1852-1857.
29. Liu, L., Kumar, S. B., Ouyang, Y., Guo, J., Performance limits of monolayer transition metal dichalcogenide transistors. *IEEE Trans. Electron. Devices* **2011**, *58* (9), 3042-3047.
30. Das, S., Demarteau, M., Roelofs, A., Nb-doped single crystalline MoS₂ field effect transistor. *Appl. Phys. Lett.* **2015**, *106* (17), 173506.
31. Zhang, K., Bersch, B. M., Joshi, J., Addou, R., Cormier, C. R., Zhang, C., Xu, K., Briggs, N. C., Wang, K., Subramanian, S., et al., Tuning the electronic and photonic properties of monolayer MoS₂ via in situ Rhenium substitutional doping. *Adv. Funct. Mater.* **2018**, *28* (16), 1706950.
32. Wu, W., Wang, L., Li, Y., Zhang, F., Lin, L., Niu, S., Chenet, D., Zhang, X., Hao, Y., Heinz, T. F., et al., Piezoelectricity of single-atomic-layer MoS₂ for energy conversion and piezotronics. *Nature* **2014**, *514*, 470.
33. Wang, Z. L., Song, J., Piezoelectric nanogenerators based on Zinc Oxide nanowire arrays. *Science* **2006**, *312* (5771), 242-246.
34. Masmanidis, S. C., Karabalin, R. B., De Vlaminck, I., Borghs, G., Freeman, M. R., Roukes, M. L., Multifunctional nanomechanical systems via tunably coupled piezoelectric actuation. *Science* **2007**, *317* (5839), 780-783.

35. Han, S. A., Kim, T.-H., Kim, S. K., Lee, K. H., Park, H.-J., Lee, J.-H., Kim, S.-W., Point-defect-passivated MoS₂ nanosheet-based high performance piezoelectric nanogenerator. *Adv. Mater.* **2018**, 30 (21), 1800342.
36. Cui, C., Xue, F., Hu, W.-J., Li, L.-J., Two-dimensional materials with piezoelectric and ferroelectric functionalities. *NPJ 2D Mater. Appl.* **2018**, 2 (1), 18.
37. Duerloo, K.-A. N., Ong, M. T., Reed, E. J., Intrinsic piezoelectricity in two-dimensional materials. *J. Phys. Chem. Lett.* **2012**, 3 (19), 2871-2876.
38. da Cunha Rodrigues, G., Zelenovskiy, P., Romanyuk, K., Luchkin, S., Kopelevich, Y., Kholkin, A., Strong piezoelectricity in single-layer graphene deposited on SiO₂ grating substrates. *Nat. Commun.* **2015**, 6, 7572.
39. Lee, J.-H., Park, J. Y., Cho, E. B., Kim, T. Y., Han, S. A., Kim, T.-H., Liu, Y., Kim, S. K., Roh, C. J., Yoon, H.-J., et al., Reliable piezoelectricity in bilayer WSe₂ for piezoelectric nanogenerators. *Adv. Mater.* **2017**, 29 (29), 1606667.
40. Castellanos-Gomez, A., Poot, M., Steele, G. A., van der Zant, H. S. J., Agraït, N., Rubio-Bollinger, G., Elastic properties of freely suspended MoS₂ nanosheets. *Adv. Mater.* **2012**, 24 (6), 772-775.
41. Liu, K., Yan, Q., Chen, M., Fan, W., Sun, Y., Suh, J., Fu, D., Lee, S., Zhou, J., Tongay, S., et al., Elastic properties of chemical-vapor-deposited monolayer MoS₂, WS₂, and their bilayer heterostructures. *Nano Lett.* **2014**, 14 (9), 5097-5103.
42. Splendiani, A., Sun, L., Zhang, Y., Li, T., Kim, J., Chim, C.-Y., Galli, G., Wang, F., Emerging photoluminescence in monolayer MoS₂. *Nano Lett.* **2010**, 10 (4), 1271-1275.
43. Dong, N., Li, Y., Feng, Y., Zhang, S., Zhang, X., Chang, C., Fan, J., Zhang, L., Wang, J., Optical limiting and theoretical modelling of layered transition metal dichalcogenide nanosheets. *Sci. Rep.* **2015**, 5, 14646.

44. Chang, K., Li, M., Wang, T., Ouyang, S., Li, P., Liu, L., Ye, J., Drastic layer-number-dependent activity enhancement in photocatalytic H₂ evolution over nMoS₂/CdS ($n \geq 1$) under visible light. *Adv. Energy Mater.* **2015**, 5 (10), 1402279.
45. Li, H., Zhang, Q., Yap, C. C. R., Tay, B. K., Edwin, T. H. T., Olivier, A., Baillargeat, D., From bulk to monolayer MoS₂: evolution of Raman scattering. *Adv. Funct. Mater.* **2012**, 22 (7), 1385-1390.
46. Lee, C., Yan, H., Brus, L. E., Heinz, T. F., Hone, J., Ryu, S., Anomalous lattice vibrations of single- and few-layer MoS₂. *ACS Nano* **2010**, 4 (5), 2695-2700.
47. Zhao, W., Ghorannevis, Z., Amara, K. K., Pang, J. R., Toh, M., Zhang, X., Kloc, C., Tan, P. H., Eda, G., Lattice dynamics in mono- and few-layer sheets of WS₂ and WSe₂. *Nanoscale* **2013**, 5 (20), 9677-9683.
48. Peimyoo, N., Shang, J., Cong, C., Shen, X., Wu, X., Yeow, E. K. L., Yu, T., Nonblinking, intense two-dimensional light emitter: monolayer WS₂ triangles. *ACS Nano* **2013**, 7 (12), 10985-10994.
49. Wang, Y., Ou, J. Z., Balendhran, S., Chrimes, A. F., Mortazavi, M., Yao, D. D., Field, M. R., Latham, K., Bansal, V., Friend, J. R., et al., Electrochemical control of photoluminescence in two-dimensional MoS₂ nanoflakes. *ACS Nano* **2013**, 7 (11), 10083-10093.
50. Castellanos-Gomez, A., Roldán, R., Cappelluti, E., Buscema, M., Guinea, F., van der Zant, H. S. J., Steele, G. A., Local strain engineering in atomically thin MoS₂. *Nano Lett.* **2013**, 13 (11), 5361-5366.
51. Wang, Y., Ou, J. Z., Chrimes, A. F., Carey, B. J., Daeneke, T., Alsaif, M. M. Y. A., Mortazavi, M., Zhuiykov, S., Medhekar, N., Bhaskaran, M., et al., Plasmon resonances of highly doped two-dimensional MoS₂. *Nano Lett.* **2015**, 15 (2), 883-890.

52. Wang, F., Wang, Z., Shifa, T. A., Wen, Y., Wang, F., Zhan, X., Wang, Q., Xu, K., Huang, Y., Yin, L., et al., Two-dimensional non-layered materials: synthesis, properties and applications. *Adv. Funct. Mater.* **2017**, 27 (19), 1603254.
53. Tan, C., Zhang, H., Wet-chemical synthesis and applications of non-layer structured two-dimensional nanomaterials. *Nat. Commun.* **2015**, 6, 7873.
54. Zhou, N., Gan, L., Yang, R., Wang, F., Li, L., Chen, Y., Li, D., Zhai, T., Nonlayered two-dimensional defective semiconductor γ -Ga₂S₃ toward broadband photodetection. *ACS Nano* **2019**, 13 (6), 6297-6307.
55. Dou, Y., Zhang, L., Xu, X., Sun, Z., Liao, T., Dou, S. X., Atomically thin non-layered nanomaterials for energy storage and conversion. *Chem. Soc. Rev.* **2017**, 46 (23), 7338-7373.
56. Puthirath Balan, A., Radhakrishnan, S., Woellner, C. F., Sinha, S. K., Deng, L., Reyes, C. d. l., Rao, B. M., Paulose, M., Neupane, R., Apte, A., et al., Exfoliation of a non-van der Waals material from iron ore hematite. *Nat. Nanotechnol.* **2018**, 13 (7), 602-609.
57. Wang, Q., Wen, Y., He, P., Yin, L., Wang, Z., Wang, F., Xu, K., Huang, Y., Wang, F., Jiang, C., et al., High-performance phototransistor of epitaxial PbS nanoplate-graphene heterostructure with edge contact. *Adv. Mater.* **2016**, 28 (30), 6497-6503.
58. Xiao, P., Chen, W., Wang, X., A review of phosphide-based materials for electrocatalytic hydrogen evolution. *Adv. Energy Mater.* **2015**, 5 (24), 1500985.
59. Zhou, W., Guo, L., Iron triad (Fe, Co, Ni) nanomaterials: structural design, functionalization and their applications. *Chem. Soc. Rev.* **2015**, 44 (19), 6697-6707.
60. Wu, W., Wu, Z., Yu, T., Jiang, C., Kim, W.-S., Recent progress on magnetic iron oxide nanoparticles: synthesis, surface functional strategies and biomedical applications. *Sci. Technol. Adv. Mater.* **2015**, 16 (2), 023501.

61. Liu, J., Hartono, S. B., Jin, Y. G., Li, Z., Lu, G. Q., Qiao, S. Z., A facile vesicle template route to multi-shelled mesoporous silica hollow nanospheres. *J. Mater. Chem.* **2010**, 20 (22), 4595-4601.
62. Hao, Q., Li, L., Yin, X., Liu, S., Li, Q., Wang, T., Anomalous conductivity-type transition sensing behaviors of n-type porous α -Fe₂O₃ nanostructures toward H₂S. *Mater. Sci. Eng. C* **2011**, 176 (7), 600-605.
63. Jubb, A. M., Allen, H. C., Vibrational spectroscopic characterization of hematite, maghemite, and magnetite thin films produced by vapor deposition. *ACS Appl. Mater. Interfaces* **2010**, 2 (10), 2804-2812.
64. Bersani, D., Lottici, P. P., Montenero, A., Micro-Raman investigation of iron oxide films and powders produced by sol-gel syntheses. *J. Raman Spectrosc.* **1999**, 30 (5), 355-360.
65. Murphy, A. B., Barnes, P. R. F., Randeniya, L. K., Plumb, I. C., Grey, I. E., Horne, M. D., Glasscock, J. A., Efficiency of solar water splitting using semiconductor electrodes. *Int. J. Hydrogen Energy* **2006**, 31 (14), 1999-2017.
66. Chernyshova, I. V., Hochella Jr, M. F., Madden, A. S., Size-dependent structural transformations of hematite nanoparticles. 1. Phase transition. *Phys. Chem. Chem. Phys.* **2007**, 9 (14), 1736-1750.
67. Xia, H., Hong, C., Li, B., Zhao, B., Lin, Z., Zheng, M., Savilov, S. V., Aldoshin, S. M., Facile synthesis of hematite quantum-dot/functionalized graphene-sheet composites as advanced anode materials for asymmetric supercapacitors. *Adv. Funct. Mater.* **2015**, 25 (4), 627-635.
68. Lindgren, T., Wang, H., Beermann, N., Vayssieres, L., Hagfeldt, A., Lindquist, S.-E., Aqueous photoelectrochemistry of hematite nanorod array. *Sol. Energy Mater. Sol. Cells* **2002**, 71 (2), 231-243.

69. Sajjadi, S. H., Goharshadi, E. K., Highly monodispersed hematite cubes for removal of ionic dyes. *J. Environ. Chem. Eng.* **2017**, 5 (1), 1096-1106.
70. Xiong, D., Wang, X., Li, W., Liu, L., Facile synthesis of iron phosphide nanorods for efficient and durable electrochemical oxygen evolution. *ChemComm* **2016**, 52 (56), 8711-8714.
71. Anantharaj, S., Ede, S. R., Sakthikumar, K., Karthick, K., Mishra, S., Kundu, S., Recent trends and perspectives in electrochemical water splitting with an emphasis on sulfide, selenide, and phosphide catalysts of Fe, Co, and Ni: a review. *ACS Catal.* **2016**, 6 (12), 8069-8097.
72. Sun, Y., Liu, Q., Gao, S., Cheng, H., Lei, F., Sun, Z., Jiang, Y., Su, H., Wei, S., Xie, Y., Pits confined in ultrathin cerium(IV) oxide for studying catalytic centers in carbon monoxide oxidation. *Nat. Commun.* **2013**, 4, 2899.
73. Du, Y., Yin, Z., Zhu, J., Huang, X., Wu, X.-J., Zeng, Z., Yan, Q., Zhang, H., A general method for the large-scale synthesis of uniform ultrathin metal sulphide nanocrystals. *Nat. Commun.* **2012**, 3, 1177.
74. Okamoto, H., The Fe-P (iron-phosphorus) system. *Bull. Alloy Phase Diagr.* **1990**, 11 (4), 404-412.
75. Yu, J., Li, J., Zhang, W., Chang, H., Synthesis of high quality two-dimensional materials via chemical vapor deposition. *Chem. Sci.* **2015**, 6 (12), 6705-6716.
76. Nicolosi, V., Chhowalla, M., Kanatzidis, M. G., Strano, M. S., Coleman, J. N., Liquid exfoliation of layered materials. *Science* **2013**, 340 (6139), 1226419.
77. Huo, C., Yan, Z., Song, X., Zeng, H., 2D materials via liquid exfoliation: a review on fabrication and applications. *Sci. Bull.* **2015**, 60 (23), 1994-2008.
78. Yi, M., Shen, Z., A review on mechanical exfoliation for the scalable production of graphene. *J. Mater. Chem. A* **2015**, 3 (22), 11700-11715.

79. Tao, H., Zhang, Y., Gao, Y., Sun, Z., Yan, C., Texter, J., Scalable exfoliation and dispersion of two-dimensional materials – an update. *Phys. Chem. Chem. Phys.* **2017**, *19* (2), 921-960.
80. Novoselov, K. S., Geim, A. K., Morozov, S. V., Jiang, D., Zhang, Y., Dubonos, S. V., Grigorieva, I. V., Firsov, A. A., Electric field effect in atomically thin carbon films. *Science* **2004**, *306* (5696), 666-669.
81. Magda, G. Z., Pető, J., Dobrik, G., Hwang, C., Biró, L. P., Tapasztó, L., Exfoliation of large-area transition metal chalcogenide single layers. *Sci. Rep.* **2015**, *5*, 14714.
82. Jung, Y., Zhou, Y., Cha, J. J., Intercalation in two-dimensional transition metal chalcogenides. *Inorg. Chem. Front.* **2016**, *3* (4), 452-463.
83. Fan, X., Xu, P., Zhou, D., Sun, Y., Li, Y. C., Nguyen, M. A. T., Terrones, M., Mallouk, T. E., Fast and efficient preparation of exfoliated 2H MoS₂ nanosheets by sonication-assisted lithium intercalation and infrared laser-induced 1T to 2H phase reversion. *Nano Lett.* **2015**, *15* (9), 5956-5960.
84. Pagona, G., Bittencourt, C., Arenal, R., Tagmatarchis, N., Exfoliated semiconducting pure 2H-MoS₂ and 2H-WS₂ assisted by chlorosulfonic acid. *ChemComm* **2015**, *51* (65), 12950-12953.
85. Yong, Y., Zhou, L., Gu, Z., Yan, L., Tian, G., Zheng, X., Liu, X., Zhang, X., Shi, J., Cong, W., et al., WS₂ nanosheet as a new photosensitizer carrier for combined photodynamic and photothermal therapy of cancer cells. *Nanoscale* **2014**, *6* (17), 10394-10403.
86. Shen, J., Wu, J., Wang, M., Dong, P., Xu, J., Li, X., Zhang, X., Yuan, J., Wang, X., Ye, M., et al., Surface tension components based selection of cosolvents for efficient liquid phase exfoliation of 2D materials. *Small* **2016**, *12* (20), 2741-2749.

87. Coleman, J. N., Lotya, M., O'Neill, A., Bergin, S. D., King, P. J., Khan, U., Young, K., Gaucher, A., De, S., Smith, R. J., et al., Two-dimensional nanosheets produced by liquid exfoliation of layered materials. *Science* **2011**, *331* (6017), 568-571.
88. Hernandez, Y., Nicolosi, V., Lotya, M., Blighe, F. M., Sun, Z., De, S., McGovern, I. T., Holland, B., Byrne, M., Gun'Ko, Y. K., et al., High-yield production of graphene by liquid-phase exfoliation of graphite. *Nat. Nanotechnol.* **2008**, *3*, 563.
89. Liu, K.-K., Zhang, W., Lee, Y.-H., Lin, Y.-C., Chang, M.-T., Su, C.-Y., Chang, C.-S., Li, H., Shi, Y., Zhang, H., et al., Growth of large-area and highly crystalline MoS₂ thin layers on insulating substrates. *Nano Lett.* **2012**, *12* (3), 1538-1544.
90. Song, L., Ci, L., Lu, H., Sorokin, P. B., Jin, C., Ni, J., Kvashnin, A. G., Kvashnin, D. G., Lou, J., Yakobson, B. I., et al., Large scale growth and characterization of atomic hexagonal boron nitride layers. *Nano Lett.* **2010**, *10* (8), 3209-3215.
91. Najmaei, S., Liu, Z., Zhou, W., Zou, X., Shi, G., Lei, S., Yakobson, B. I., Idrobo, J.-C., Ajayan, P. M., Lou, J., Vapour phase growth and grain boundary structure of molybdenum disulphide atomic layers. *Nat. Mater.* **2013**, *12*, 754.
92. Huang, C., Wu, S., Sanchez, A. M., Peters, J. J. P., Beanland, R., Ross, J. S., Rivera, P., Yao, W., Cobden, D. H., Xu, X., Lateral heterojunctions within monolayer MoSe₂–WSe₂ semiconductors. *Nat. Mater.* **2014**, *13*, 1096.
93. Zhang, X.-Q., Lin, C.-H., Tseng, Y.-W., Huang, K.-H., Lee, Y.-H., Synthesis of lateral heterostructures of semiconducting atomic layers. *Nano Lett.* **2015**, *15* (1), 410-415.
94. Li, H., Duan, X., Wu, X., Zhuang, X., Zhou, H., Zhang, Q., Zhu, X., Hu, W., Ren, P., Guo, P., et al., Growth of alloy MoS_{2x}Se_{2(1-x)} nanosheets with fully tunable chemical compositions and optical properties. *J. Am. Chem. Soc.* **2014**, *136* (10), 3756-3759.

95. Şar, H., Özden, A., Yorulmaz, B., Sevik, C., Kosku Perkgoz, N., Ay, F., A comparative device performance assesment of CVD grown MoS₂ and WS₂ monolayers. *J. Mater. Sci.: Mater. Electron.* **2018**, 29 (10), 8785-8792.
96. Yoo, D., Kim, M., Jeong, S., Han, J., Cheon, J., Chemical synthetic strategy for single-layer transition-metal chalcogenides. *J. Am. Chem. Soc.* **2014**, 136 (42), 14670-14673.
97. Xie, J., Zhang, J., Li, S., Grote, F., Zhang, X., Zhang, H., Wang, R., Lei, Y., Pan, B., Xie, Y., Controllable disorder engineering in oxygen-incorporated MoS₂ ultrathin nanosheets for efficient hydrogen evolution. *J. Am. Chem. Soc.* **2013**, 135 (47), 17881-17888.
98. Son, J. S., Yu, J. H., Kwon, S. G., Lee, J., Joo, J., Hyeon, T., Colloidal synthesis of ultrathin two-dimensional semiconductor nanocrystals. *Adv. Mater.* **2011**, 23 (28), 3214-3219.
99. Sasikala, S. P., Poulin, P., Aymonier, C., Advances in subcritical hydro-/solvothetmal processing of graphene materials. *Adv. Mater.* **2017**, 29 (22), 1605473.
100. Ramakrishna Matte, H. S. S., Gomathi, A., Manna, A. K., Late, D. J., Datta, R., Pati, S. K., Rao, C. N. R., MoS₂ and WS₂ analogues of graphene. *Angew Chem. Int. Ed.* **2010**, 49 (24), 4059-4062.
101. Ma, Z., Huang, X., Dou, S., Wu, J., Wang, S., One-pot synthesis of Fe₂O₃ nanoparticles on nitrogen-doped graphene as advanced supercapacitor electrode materials. *J. Phys. Chem. C* **2014**, 118 (31), 17231-17239.
102. Sun, Z., Liao, T., Dou, Y., Hwang, S. M., Park, M.-S., Jiang, L., Kim, J. H., Dou, S. X., Generalized self-assembly of scalable two-dimensional transition metal oxide nanosheets. *Nat. Commun.* **2014**, 5, 3813.

103. Zhang, X., Zhang, J., Zhao, J., Pan, B., Kong, M., Chen, J., Xie, Y., Half-metallic ferromagnetism in synthetic Co₉Se₈ nanosheets with atomic thickness. *J. Am. Chem. Soc.* **2012**, *134* (29), 11908-11911.
104. Xiao, X., Song, H., Lin, S., Zhou, Y., Zhan, X., Hu, Z., Zhang, Q., Sun, J., Yang, B., Li, T., et al., Scalable salt-templated synthesis of two-dimensional transition metal oxides. *Nat. Commun.* **2016**, *7*, 11296.
105. Wu, X.-J., Huang, X., Qi, X., Li, H., Li, B., Zhang, H., Copper-based ternary and quaternary semiconductor nanoplates: templated synthesis, characterization, and photoelectrochemical properties. *Angew Chem. Int. Ed.* **2014**, *53* (34), 8929-8933.
106. Son, J. S., Park, K., Kwon, S. G., Yang, J., Choi, M. K., Kim, J., Yu, J. H., Joo, J., Hyeon, T., Dimension-controlled synthesis of CdS nanocrystals: from 0D quantum dots to 2D nanoplates. *Small* **2012**, *8* (15), 2394-2402.
107. Cheng, W., He, J., Yao, T., Sun, Z., Jiang, Y., Liu, Q., Jiang, S., Hu, F., Xie, Z., He, B., et al., Half-unit-cell α -Fe₂O₃ semiconductor nanosheets with intrinsic and robust ferromagnetism. *J. Am. Chem. Soc.* **2014**, *136* (29), 10393-10398.
108. Chen, B., Chang, S., Li, D., Chen, L., Wang, Y., Chen, T., Zou, B., Zhong, H., Rogach, A. L., Template synthesis of CuInS₂ nanocrystals from In₂S₃ nanoplates and their application as counter electrodes in dye-sensitized solar cells. *Chem. Mater.* **2015**, *27* (17), 5949-5956.
109. Zhou, J., Qin, J., Zhao, N., Shi, C., Liu, E.-Z., He, F., Li, J., He, C., Salt-template-assisted synthesis of robust 3D honeycomb-like structured MoS₂ and its application as a lithium-ion battery anode. *J. Mater. Chem. A* **2016**, *4* (22), 8734-8741.
110. Ke, X., Cao, J., Zheng, M., Chen, Y., Liu, J., Ji, G., Molten salt synthesis of single crystal Co₃O₄ nanorods. *Mater. Lett.* **2007**, *61* (18), 3901-3903.

111. Meng, T., Zheng, L., Qin, J., Zhao, D., Cao, M., A three-dimensional hierarchically porous Mo₂C architecture: salt-template synthesis of a robust electrocatalyst and anode material towards the hydrogen evolution reaction and lithium storage. *J. Mater. Chem. A* **2017**, 5 (38), 20228-20238.
112. Yoon, Y., Ganapathi, K., Salahuddin, S., How good can monolayer MoS₂ transistors be? *Nano Lett.* **2011**, 11 (9), 3768-3773.
113. Lee, H. S., Min, S.-W., Chang, Y.-G., Park, M. K., Nam, T., Kim, H., Kim, J. H., Ryu, S., Im, S., MoS₂ nanosheet phototransistors with thickness-modulated optical energy gap. *Nano Lett.* **2012**, 12 (7), 3695-3700.
114. Yin, Z., Li, H., Li, H., Jiang, L., Shi, Y., Sun, Y., Lu, G., Zhang, Q., Chen, X., Zhang, H., Single-layer MoS₂ phototransistors. *ACS Nano* **2012**, 6 (1), 74-80.
115. Mak, K. F., Lee, C., Hone, J., Shan, J., Heinz, T. F., Atomically thin MoS₂: a new direct-gap semiconductor. *Phys. Rev. Lett.* **2010**, 105 (13), 136805.
116. Lukowski, M. A., Daniel, A. S., Meng, F., Forticaux, A., Li, L., Jin, S., Enhanced hydrogen evolution catalysis from chemically exfoliated metallic MoS₂ nanosheets. *J. Am. Chem. Soc.* **2013**, 135 (28), 10274-10277.
117. Lin, H., Wang, J., Luo, Q., Peng, H., Luo, C., Qi, R., Huang, R., Travas-Sejdic, J., Duan, C.-G., Rapid and highly efficient chemical exfoliation of layered MoS₂ and WS₂. *J Alloys Compd.* **2017**, 699, 222-229.
118. Hun, X., Wang, S., Wang, S., Zhao, J., Luo, X., A photoelectrochemical sensor for ultrasensitive dopamine detection based on single-layer NanoMoS₂ modified gold electrode. *Sensor Actuat. B-Chem.* **2017**, 249, 83-89.
119. Shang, X., Chi, J.-Q., Lu, S.-S., Gou, J.-X., Dong, B., Li, X., Liu, Y.-R., Yan, K.-L., Chai, Y.-M., Liu, C.-G., Carbon fiber cloth supported interwoven WS₂ nanoslates with highly enhanced performances for supercapacitors. *Appl. Surf. Sci.* **2017**, 392, 708-714.

120. Liu, Y., Wang, W., Huang, H., Gu, L., Wang, Y., Peng, X., The highly enhanced performance of lamellar WS₂ nanosheet electrodes upon intercalation of single-walled carbon nanotubes for supercapacitors and lithium ions batteries. *ChemComm* **2014**, 50 (34), 4485-4488.
121. Hu, B., Qin, X., Asiri, A. M., Alamry, K. A., Al-Youbi, A. O., Sun, X., WS₂ nanoparticles–encapsulated amorphous carbon tubes: A novel electrode material for supercapacitors with a high rate capability. *Electrochem. commun.* **2013**, 28, 75-78.
122. Choudhary, N., Li, C., Chung, H.-S., Moore, J., Thomas, J., Jung, Y., High-performance one-body core/shell nanowire supercapacitor enabled by conformal growth of capacitive 2D WS₂ layers. *ACS Nano* **2016**, 10 (12), 10726-10735.
123. Khalil, A., Liu, Q., He, Q., Xiang, T., Liu, D., Wang, C., Fang, Q., Song, L., Metallic 1T-WS₂ nanoribbons as highly conductive electrodes for supercapacitors. *RSC Adv.* **2016**, 6 (54), 48788-48791.
124. Qian, J., Peng, Z., Wang, P., Fu, X., Bulk fabrication of WS₂ nanoplates: investigation on the morphology evolution and electrochemical performance. *ACS Appl. Mater. Interfaces* **2016**, 8 (26), 16876-16884.
125. Huang, J., Wang, X., Li, J., Cao, L., Xu, Z., Wei, H., WS₂-Super P nanocomposites anode material with enhanced cycling stability for lithium ion batteries. *J Alloys Compd.* **2016**, 673, 60-66.
126. Li, X., Li, X., Li, Z., Wang, J., Zhang, J., WS₂ nanoflakes based selective ammonia sensors at room temperature. *Sensor Actuat. B-Chem.* **2017**, 240, 273-277.
127. Lin, T., Zhong, L., Song, Z., Guo, L., Wu, H., Guo, Q., Chen, Y., Fu, F., Chen, G., Visual detection of blood glucose based on peroxidase-like activity of WS₂ nanosheets. *Biosens. Bioelectron.* **2014**, 62, 302-307.

128. Qin, Y., Ma, Y., Jin, X., Zhang, L., Ye, G., Zhao, S., A sensitive fluorescence turn-on assay of bleomycin and nuclease using WS₂ nanosheet as an effective sensing platform. *Anal. Chim. Acta* **2015**, 866, 84-89.
129. Yuan, Y., Li, R., Liu, Z., Establishing water-soluble layered WS₂ nanosheet as a platform for biosensing. *Anal. Chem.* **2014**, 86 (7), 3610-3615.
130. Ho, W., Yu, J. C., Lin, J., Yu, J., Li, P., Preparation and photocatalytic behavior of MoS₂ and WS₂ nanocluster sensitized TiO₂. *Langmuir* **2004**, 20 (14), 5865-5869.
131. Sang, Y., Zhao, Z., Zhao, M., Hao, P., Leng, Y., Liu, H., From UV to near-infrared, WS₂ nanosheet: a novel photocatalyst for full solar light spectrum photodegradation. *Adv. Mater.* **2015**, 27 (2), 363-369.
132. Bayat, A., Saievar-Iranizad, E., Synthesis of blue photoluminescent WS₂ quantum dots via ultrasonic cavitation. *J. Lumin.* **2017**, 185, 236-240.
133. Ghorai, A., Bayan, S., Gogurla, N., Midya, A., Ray, S. K., Highly luminescent WS₂ quantum dots/ZnO heterojunctions for light emitting devices. *ACS Appl. Mater. Interfaces* **2017**, 9 (1), 558-565.
134. Chen, J., Xu, L., Li, W., Gou, X., α -Fe₂O₃ nanotubes in gas sensor and lithium-ion battery applications. *Adv. Mater.* **2005**, 17 (5), 582-586.
135. Cherepy, N. J., Liston, D. B., Lovejoy, J. A., Deng, H., Zhang, J. Z., Ultrafast studies of photoexcited electron dynamics in γ - and α -Fe₂O₃ semiconductor nanoparticles. *J. Phys. Chem. B* **1998**, 102 (5), 770-776.
136. Dias, P., Vilanova, A., Lopes, T., Andrade, L., Mendes, A., Extremely stable bare hematite photoanode for solar water splitting. *Nano Energy* **2016**, 23, 70-79.
137. Wang, G., Ling, Y., Wheeler, D. A., George, K. E. N., Horsley, K., Heske, C., Zhang, J. Z., Li, Y., Facile synthesis of highly photoactive α -Fe₂O₃-based films for water oxidation. *Nano Lett.* **2011**, 11 (8), 3503-3509.

138. Yang, T.-Y., Kang, H.-Y., Sim, U., Lee, Y.-J., Lee, J.-H., Koo, B., Nam, K. T., Joo, Y.-C., A new hematite photoanode doping strategy for solar water splitting: oxygen vacancy generation. *Phys. Chem. Chem. Phys.* **2013**, *15* (6), 2117-2124.
139. Callejas, J. F., McEnaney, J. M., Read, C. G., Crompton, J. C., Biacchi, A. J., Popczun, E. J., Gordon, T. R., Lewis, N. S., Schaak, R. E., Electrocatalytic and photocatalytic hydrogen production from acidic and neutral-pH aqueous solutions using iron phosphide nanoparticles. *ACS Nano* **2014**, *8* (11), 11101-11107.
140. Chung, D. Y., Jun, S. W., Yoon, G., Kim, H., Yoo, J. M., Lee, K.-S., Kim, T., Shin, H., Sinha, A. K., Kwon, S. G., et al., Large-scale synthesis of carbon-shell-coated FeP nanoparticles for robust hydrogen evolution reaction electrocatalyst. *J. Am. Chem. Soc.* **2017**, *139* (19), 6669-6674.
141. Xu, Y., Wu, R., Zhang, J., Shi, Y., Zhang, B., Anion-exchange synthesis of nanoporous FeP nanosheets as electrocatalysts for hydrogen evolution reaction. *ChemComm* **2013**, *49* (59), 6656-6658.
142. Son, C. Y., Kwak, I. H., Lim, Y. R., Park, J., FeP and FeP₂ nanowires for efficient electrocatalytic hydrogen evolution reaction. *ChemComm* **2016**, *52* (13), 2819-2822.
143. Yan, Y., Xia, B. Y., Ge, X., Liu, Z., Fisher, A., Wang, X., A flexible electrode based on iron phosphide nanotubes for overall water splitting. *Chem. Eur. J.* **2015**, *21* (50), 18062-18067.
144. Lv, C., Yang, Q., Huang, Q., Huang, Z., Xia, H., Zhang, C., Phosphorus doped single wall carbon nanotubes loaded with nanoparticles of iron phosphide and iron carbide for efficient hydrogen evolution. *J. Mater. Chem. A* **2016**, *4* (34), 13336-13343.
145. Yu, Y., Peng, Z., Asif, M., Wang, H., Wang, W., Wu, Z., Wang, Z., Qiu, X., Tan, H., Liu, H., FeP nanocrystals embedded in N-doped carbon nanosheets for efficient

- electrocatalytic hydrogen generation over a broad pH range. *ACS Sustain. Chem. Eng.* **2018**, 6 (9), 11587-11594.
146. Son, C. Y., Kwak, I. H., Lim, Y. R., Park, J., FeP and FeP₂ nanowires for efficient electrocatalytic hydrogen evolution reaction. *ChemComm* **2016**, 52 (13), 2819-2822.
147. Yao, Y., Mahmood, N., Pan, L., Shen, G., Zhang, R., Gao, R., Aleem, F.-e., Yuan, X., Zhang, X., Zou, J.-J., Iron phosphide encapsulated in P-doped graphitic carbon as efficient and stable electrocatalyst for hydrogen and oxygen evolution reactions. *Nanoscale* **2018**, 10 (45), 21327-21334.
148. Lu, X. F., Yu, L., Lou, X. W., Highly crystalline Ni-doped FeP/carbon hollow nanorods as all-pH efficient and durable hydrogen evolving electrocatalysts. *Sci. Adv.* **2019**, 5 (2), eaav6009.
149. Hu, K., Xiao, Z., Cheng, Y., Yan, D., Chen, R., Huo, J., Wang, S., Iron phosphide/N, P-doped carbon nanosheets as highly efficient electrocatalysts for oxygen reduction reaction over the whole pH range. *Electrochim. Acta* **2017**, 254, 280-286.

Chapter 3

Liquid phase acoustic wave exfoliation of layered MoS₂:

Critical impact of electric field in efficiency†

† The contents of this chapter is published in Mohiuddin et al., Liquid Phase Acoustic Wave Exfoliation of Layered MoS₂: Critical Impact of Electric Field in Efficiency, *Chemistry of Materials*, 2018, 30 (16), 5593-5601.

3.1 Introduction

Liquid-phase exfoliation is a common method for obtaining high yield suspensions of 2D transition metal dichalcogenide flakes¹⁻³. Different liquid-phase exfoliation methods including mechanical blending and grinding, and also shear mixing (or a combination of them) have been developed²⁻⁸. These techniques may require long processing time and sometimes a low proportion of monolayers are achieved⁷⁻¹⁰. High population of monolayers can be exfoliated by liquid-phase ion intercalation processes; however, such methods are still time-consuming, require hazardous solvents and contribute to phase transformation^{3, 11-15}.

A pathway to increase the efficiency of exfoliating non-centrosymmetric layered crystals is to devise a process based on surface acoustic wave (SAW). A SAW is a nanometer-order amplitude mechanical wave, accompanying an electric field, which propagates along the surface of a piezoelectric substrate. SAW devices have already been well demonstrated in diverse applications such as sensors, actuators, filters, microfluidics, etc. Bandpass filters, ladder filters, and resonators are some commercial applications of SAW devices in the electronics and telecommunication industries. Micromixing, pumping, jetting, atomisation, particle concentration, trapping, patterning, de-agglomeration are also some common implications of SAW microfluidics¹⁶⁻¹⁸. The extremely large surface acceleration along the

substrate as the SAW traverses is an efficient means for driving liquid actuation at the microscale¹⁶⁻¹⁸, including microcentrifugation flows that will be exploited in this work to exfoliate the flakes.

The concomitant electric field with the mechanical wave in that constitutes the SAW^{19,20}, can be advantageous for enhancing the exfoliation process of layered TMDs, such as 2H-MoS₂ under specific conditions. Adjacent planes of 2H-MoS₂ are held together by weak van der Waals forces to form the bulk of the crystal. Stacking arrangement of adjacent atomic layers in bulk 2H-MoS₂ makes it centrosymmetric which does not show piezoelectricity. In contrast, dimensionally reduced monolayered or odd layered MoS₂ exhibits strong piezoelectricity due to their non-centrosymmetric crystal structure^{21,22}. The piezoelectricity depends on the number of layers. For example, the piezoelectric coupling coefficient of monolayer MoS₂ is three times higher than that of trilayer²². Such non-centrosymmetric behaviour, hence the emergence of piezoelectricity, is also observed for the outer planes on each side the 2H-MoS₂ bulk.

Given the piezoelectricity of non-centrosymmetric 2H-MoS₂, SAW induced electric field exert a force on the top piezoelectric layer of the bulk 2H-MoS₂ or the flakes which are made of an odd number of layers. This is in addition to the mechanical shear imparted on the material, regardless of whether it is centrosymmetric or non-centrosymmetric, by the SAW and the flow it induces in the liquid. It is expected that the combination of the shear force and electric field make the exfoliation process much more efficient. Based on this assumption, a microcentrifugation process to exfoliate layered 2H-MoS₂ in this chapter. In particular, the thickness of layered MoS₂ can be tuned through controlled manipulation of the SAW exposure duration, and the experimental results for the number of layers are verified with a computational prediction.

3.2 Experimental section

3.2.1 Fabrication of the SAW device

Optically surface polished 500 μm thick single crystal 128° Y-rotated lithium niobate (128° YX LiNbO_3) wafer was used as the substrate on which two sets of interdigital transducers (IDTs - Figure 3-1) were patterned using a standard UV photolithography process²³. Each IDT comprised 20 finger pairs. Additionally, a reflector is patterned in parallel to each IDT to reflect the acoustic waves from the devices' edges back to the position where the liquid is deposited on the SAW device.

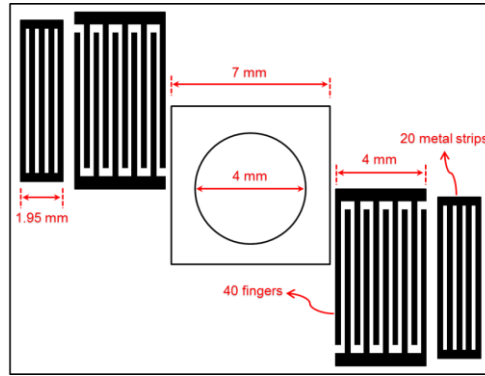


Figure 3-1 SAW device configuration. Details configuration of the developed microcentrifugation SAW device (offset). There are two IDTs, each composed of 20 electrode pairs. The imposed wavelength of SAW device is 200 μm ; therefore, the operating frequency of the transducer was ~ 19.2 MHz. 20 parallel metal strips positioned behind the IDTs act as reflectors to increase energy efficiency.

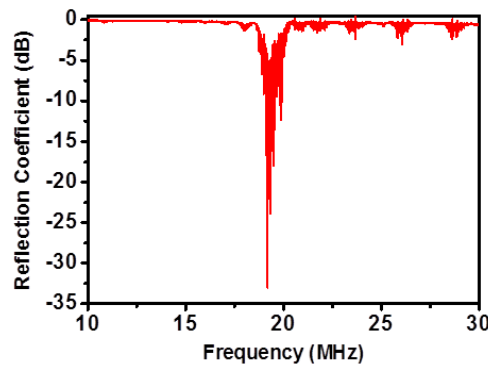


Figure 3-2 Reflection coefficient of the developed SAW device. Reflection coefficient (S_{11}) of the developed device measured by vector network analyser (VNA). The device delivers best performance at ~ 19.2 MHz. Reflection coefficient in dB indicates only negligible amount of power has been reflected by the device at the resonance frequency, thus optimum device performance.

These reflectors each comprise of 20 metal strips with each finger has possessed a width of 50 μm . As such, in IDTs, each metallic finger pairs and their associated spacing, has a width of 200 μm , resulting in a similar wavelength which excites the resonance frequency of ~ 19.2 MHz (Figure 3-2) for SAW travelling at 3850 m s^{-1} . A setup consisting of a RF signal generator (N10149, Agilent) and power amplifier (ZHL-5W-1) were used to drive the IDTs at the resonance frequency using an applied sinusoidal electric field.

3.2.2 Preparation of PDMS reservoir

The prepolymer of polydimethylsiloxane (PDMS) and curing agent (Dow Corning Corporation, USA) were mixed with a weight ratio of 10:1, and poured into a plastic petri dish to form ~ 1.5 mm height. This was then degassed in a vacuum desiccator and cured in a vacuum oven at 80°C . After the curing process, PDMS reservoir was prepared by punching a 4 mm diameter hole. For sealing of the PDMS reservoir onto the SAW substrate, oxygen plasma for 30 s at 400 mTorr in a pressurised chamber (Harrick Plasma, Max Power 200W). The PDMS reservoir was subsequently pressed against the substrate immediately after the surfaces treatment and then heated in an oven at 80°C for 1 h.

3.2.3 Sample preparation and characterisation

A sample of 20 mg of MoS_2 powder (99.9% purity, 0.8-1.2 μm size, US Research Nanomaterials, Inc.) was added to 10 mL of Milli-Q water (bulk MoS_2 powder; Figure 3-3). 0.05 mg mL^{-1} of Tween 20 (VWR) was then added into the mix to stabilise the dispersion. After exfoliation with the SAW, the MoS_2 nanoflakes in the supernatant were collected for further characterisation after centrifugation for 30 min at 2000 rpm. The TEM images were acquired using JEOL1010, whereas high-resolution TEM (HRTEM) imaging was performed in both JEOL2010 and JEOL2100F. Samples for TEM imaging were prepared by drop-casting

the water suspended 2D MoS₂ flakes onto TEM grids. Nanoflake thickness measurements were performed with Bruker Dimension Icon AFM in ScanAsyst (air) mode. Exfoliated MoS₂ was drop-casted onto gold-coated silicon substrates, and Raman analysis of the samples was performed under ambient conditions using a Jobin Yvon Horiba TRIAX 320 spectrometer fitted with a 100× magnification lens (60 s with 3 accumulations, 532 nm excitation wavelengths). The XPS measurements were performed using Thermo K-Alpha at pass energy of 100 eV for the peak scans. The instrument uses an aluminium K- α monochromated X-ray source (1486.7 eV), with a spot size of approximately 400 μ m.

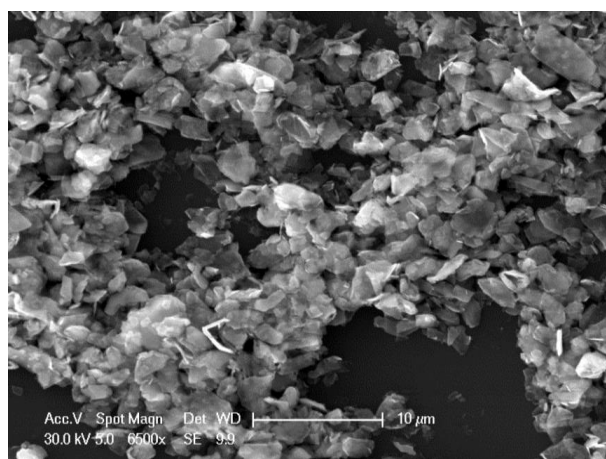


Figure 3-3 SEM of bulk MoS₂. SEM (taken at 30kV) of the bulk MoS₂ which has 0.8 to 1.2 μ m flakes size.

3.2.4 Computational methods

The Gaussian basis set *ab initio* package CRYSTAL14 was used in hybrid spin-dependent density functional theory (DFT) calculations^{24, 25}. The B3LYP hybrid exchange-correlation functional was employed augmented with an empirical London-type correction to the energy to include dispersion contributions to the total energy²⁶. The correction term is based on the Grimme method, which has been used with B3LYP for calculating cohesive energies in dispersion bonded molecular crystals^{27, 28}. For sulphur, the Durand Effective Core Pseudopotential (ECP) was used to account for the core electrons in sulphur and 1 31G* basis

sets for the valance electrons. For molybdenum, a Hay-Wadt small-core ECP was used in order to account for the 28 core electrons and a 311-31G basis set for the valance electrons²⁹. Periodically infinite, 1 to 9 layer MoS₂ nanoflakes were constructed from a geometry optimised MoS₂ bulk structure and their nanoflake energies, under an applied electric field (perpendicular to the surface of the nanoflake), were calculated using DFT (B3LYP) and the method described by Grimme to calculate the dispersion forces. 15×15×1 k-point sampling was used for converging the electronic ground state^{27, 28}. This method has already been successfully applied to MoS₂ and SnS₂ nanoflakes calculations^{30, 31}.

3.3 Results and discussion

Standard lithography was employed to pattern the SAW device, construct the PDMS reservoir and seal it onto the transducer as presented in the Experimental Section. Figure 3-4A shows a schematic diagram of the microcentrifugation SAW device that incorporates a PDMS reservoir for the exfoliation of MoS₂. A droplet (17 μ L) of 2H-MoS₂ nanoparticles (2 mg mL⁻¹) placed into the PDMS reservoir, and the SAW device is excited at ~3 W (14 V) and ~19.2 MHz. Illustration of a monolayer MoS₂ after the exfoliation process represented in Figure 3-4B.

When a high frequency propagating SAW encounters the liquid droplet in its path, as shown in Figure 3-4A, it leaks its energy into the liquid. This produces a compressional wave in the liquid, which, as a consequence of viscous attenuation in the liquid media, induces strong acoustic streaming within the droplet (as depicted by the blue arrows in Figure 3-4C and 3.4D)¹⁷. The in-plane component of the SAW beneath the liquid droplet suffers from minimal attenuation since the droplet actuation is mainly driven by the out-of-plane component³². The degree of symmetry associated with the droplet streaming is a function of the waves propagation direction, the droplet position and the boundaries of the reservoir^{18, 33}. A symmetric streaming pattern comprising, two quasi-steady vortices can be seen if the liquid droplet is

positioned in the centre of acoustic wave propagation path (Figure 3-4C), whereas an asymmetric pattern leading to azimuthal streaming is generated if the liquid droplet is placed off-centre with respect to the SAW radiation (Figure 3-4D). The latter configuration found to be more effective for exfoliation, due to the large streaming velocities $\sim 0.15 \text{ m s}^{-1}$ that can be attained. As discussed previously in Li et al., dispersion of the MoS_2 particles occurs under the intense streaming above a threshold velocity, RF (radio frequency) power, MoS_2 flakes properties and liquid surface tension are the dominant factors directly correlating the effective thickness-modulation of MoS_2 ³³. Powers lower than 0.3 W were insufficient to produce any streaming flows and beyond 3 W liquid atomisation was observed. As such, 3W RF power was consistently used throughout the experimental study. Low concentration surfactant was used in the experiments to stabilise the exfoliated flakes dispersions. The importance of this method is that the process can be scaled-up by using parallel arrays of devices. Parallel arrays of low-cost microcentrifugation SAW devices ($\sim \text{USD } \$1/\text{device}$) can be integrated for potential large-scale throughput as well as long-term device operation. The modules of those chips can be operated simultaneously. The idea of such scaling up has been demonstrated in a versatile modular plug-and-actuate concept of microarray titre plate³⁴ that can be adopted for the mass production of MoS_2 . The scaling up of the proof-of-concept work presented in this article utilising the intrinsic piezoelectric properties of MoS_2 using SAW devices, will be demonstrated in a future article. In order to investigate and obtain a better insight into the performance of the system, the exfoliated MoS_2 nanoflakes at different SAW exposure durations were experimentally characterised with AFM, TEM, and Raman spectroscopy.

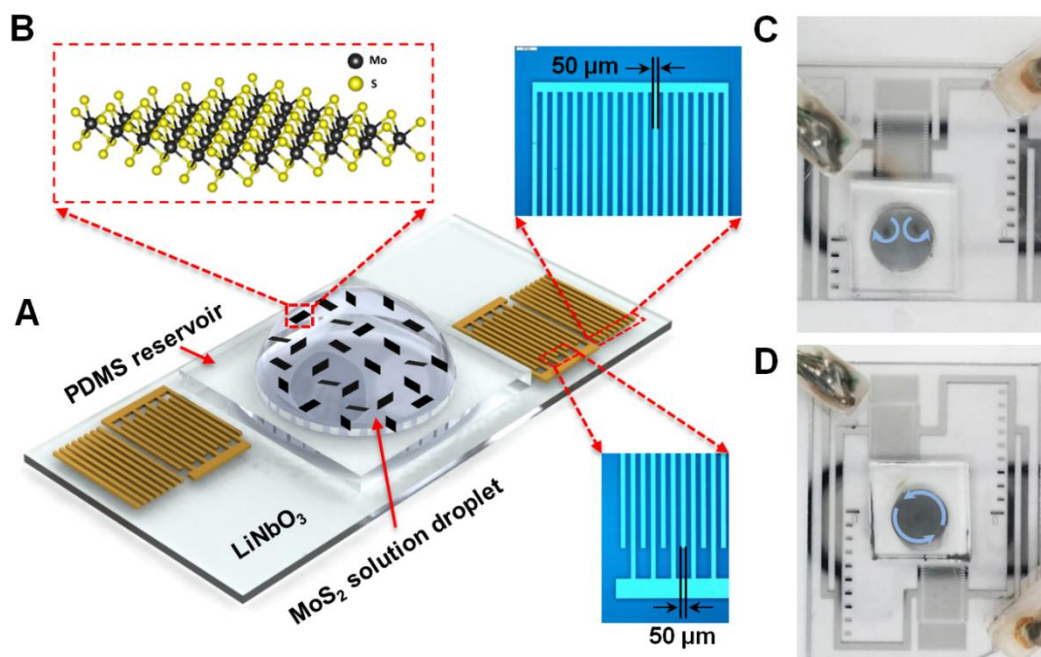


Figure 3-4 Illustration and photographs of microcentrifugation SAW devices. (A) Illustration of an asymmetric micro-exfoliation SAW device constituting the lithium niobate chip with a PDMS reservoir bonded onto it. The insets show the IDTs, reflectors and their dimensions. (B) Illustration of monolayer MoS₂ structure. (C) Centred droplet aligned with a single IDT on the device giving rise to two stable acoustic streaming vortices in the droplet. (D) Azimuthal acoustic streaming circulation in the droplet as a consequence of the asymmetric positioning of the droplet confined in the reservoir, which is placed off-centre with respect to the two opposing IDTs.

Approximately 10 μL of the supernatant solutions were drop-casted onto Si substrates and imaged by AFM to estimate the surface topography and thickness profile of the nanoflakes. Figure 3-5 represents the AFM images with thickness distribution histograms for the exfoliated nanoflakes obtained from 1 to 25 min SAW exposed samples.

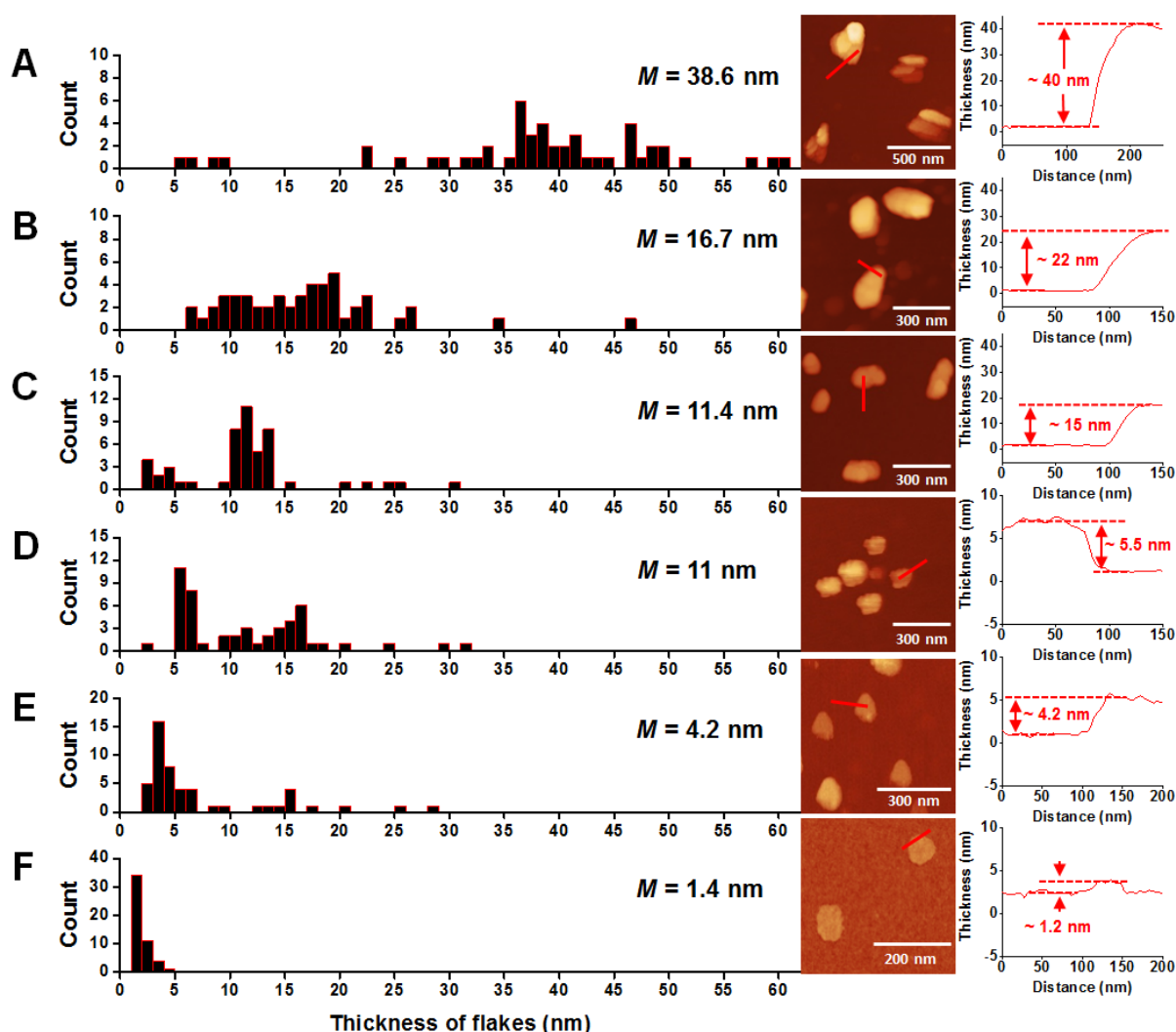


Figure 3-5 Characterisation of thickness distribution. Thickness distribution histograms of the exfoliated MoS₂ nanoflakes, obtained from the AFM measurements, along with typical images and height profile at different SAW exposure durations of (A) 1 (B) 5 (C) 10 (D) 15 (E) 20 and (F) 25 min. It can be seen that the SAW exfoliation process requires at-least 25 min to produce monolayers of MoS₂ nanoflakes effectively. M represents the median thickness in the resolution of 0.1 nm.

50 nanoflakes were used for the construction of the histograms for all cases. The flakes showed a large thickness distribution for the 1 min SAW exposed sample with a majority in the range of 36 to 42 nm (median of 38.6 nm). The median for the thickness distribution of nanoflakes continues to shift to lower values with increasing of exposure time (Figure 3-5). The SAW exfoliation process became monolayer dominant at 25 min exposure. After this exposure duration, the majority of the nanoflakes' thicknesses were ranged between ~1.2 to ~2 nm

corresponding to mono and double layer of MoS₂ with the presence of surfactant residual^{35, 36}. The frequency of monolayers obtained is relatively high (58%) for the 25 min case in comparison to other liquid exfoliation methods, and an analysis of performance is presented later in this text. Moreover, 25 min sample exhibits a constricted width normal distribution curve in comparison to more expanded distributions for other exfoliation durations. It is important to consider that the forces applied to the particles consist of electric field and also shear forces. These shear forces exist during the exfoliation and are generated by the SAW acoustic streaming. Even-numbered flakes that are not affected by electric field are exfoliated due to this shear force generated inside the droplet by the SAW streaming; therefore, thick even number of layers are absent in 25 min SAW exfoliated sample. The exfoliation trend is clearly seen in Figure 3-5 and the median thickness of the flakes constantly decreases from 1 to 25 min due to both SAW streaming and electric field. However, the monolayers, which are predicted based on the mathematical simulations (presented later in this text), are mostly seen at 25 min time and that's the duration that the electric field effect dominates the process.

To further investigate the exfoliation process, TEM of all samples were obtained and representative examples are shown in Figure 3-6 along with the HRTEM and selected area electron diffraction (SAED) of the long run samples (20 and 25 min). The TEM images are in general agreement with AFM topographies. Highly crystalline, defect-free MoS₂ nanoflakes are observed in HRTEM images. HRTEM together with the SAED show hexagonal lattice structure of single-crystalline MoS₂ with fringe spacing of ~ 0.27 nm corresponding to the (100) lattice planes³⁰. The layer spacing in samples with several in-registry planes is 0.7 nm.

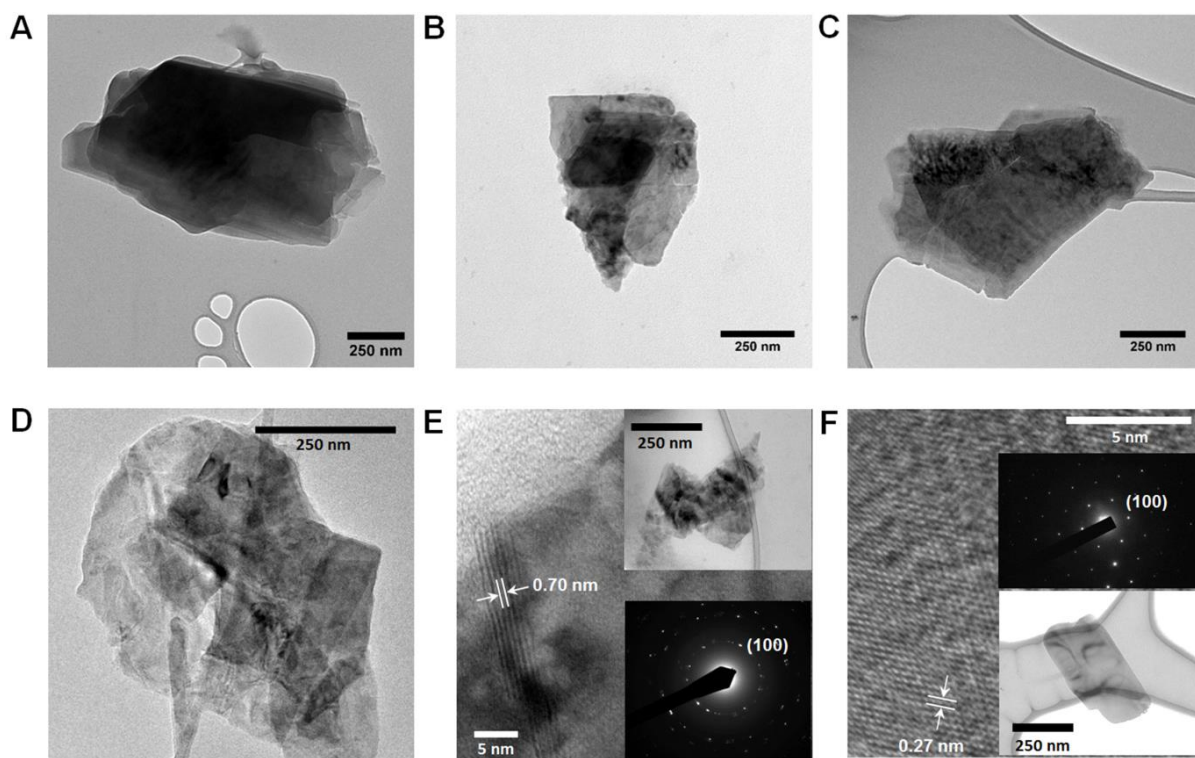


Figure 3-6 Microscopic characterisation of exfoliated nanoflakes. TEM images of the MoS₂ nanoflakes exfoliated from bulk 2H-MoS₂ for different SAW exposure durations. (A) 1 min (B) 5 min (C) 10 min (D) 15 min (E) HRTEM of the 20 min sample with corresponding SAED and TEM image represented in the inset. (F) HRTEM of the 25 min sample with TEM and SAED (inset).

Micro-Raman spectroscopy was conducted to assess the vibrational modes of MoS₂ nanoflakes obtained with the different SAW exposure durations. The E_{2g}¹ and A_{1g} modes are considered as they are the thickness-dependent modes. As the MoS₂ crystal is dimensionally reduced, the in-plane (E_{2g}¹) mode of the bulk crystal, whose peak occurs at ~382 cm⁻¹, stiffens thus blue shifted and conversely the out-of-plane (A_{1g}) mode, whose peak occurs at ~407 cm⁻¹ softens hence red shifted³⁷. The wavenumber difference between the two main Raman peaks (E_{2g}¹ and A_{1g}) is shown in Figure 3-7A for bulk, 1 min and 25 min SAW exfoliated samples. The 25 min SAW exfoliated sample possesses the smallest wavenumber difference (23.62 cm⁻¹) in comparison with the bulk (25.64 cm⁻¹)^{38, 39}. The full wavenumber versus exfoliation time curve is presented in Figure 3-7B. In accordance with AFM, the wavenumber difference decreases

with increasing SAW exposure duration and hence the reduction in the number of layers. The difference of wavenumbers in vibrational peaks (E_{2g}^1 and A_{1g}) never reaches those smaller values compared to the previous reports that are representative of monolayers³⁷. Such discrepancy is likely due to the effect of residues on flakes and also polydispersity of nanoflake thicknesses, which have been similarly reported previously³⁹⁻⁴¹.

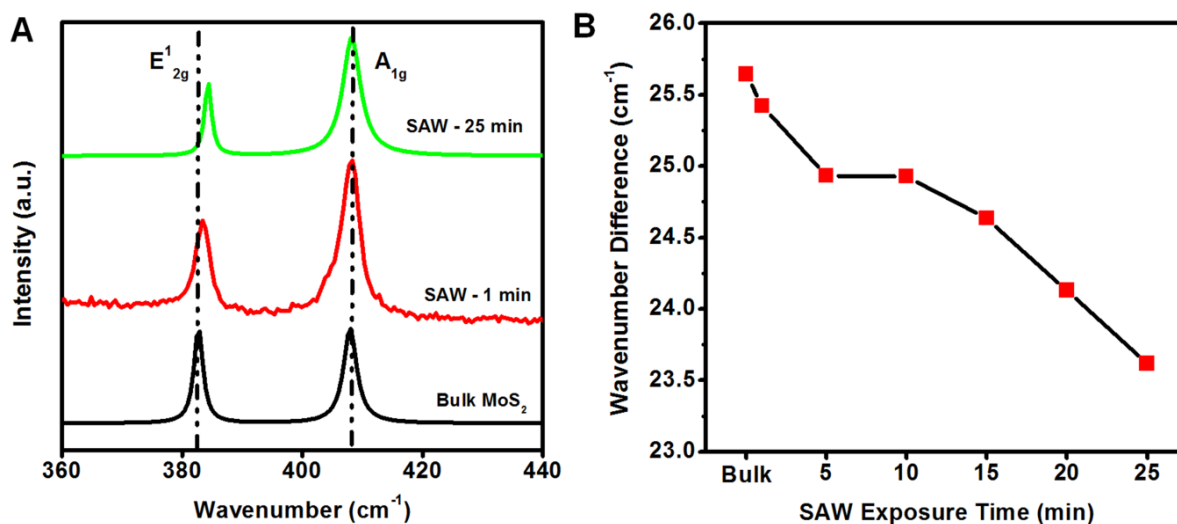


Figure 3-7 Structural characterisation of exfoliated nanoflakes. (A) Raman spectra of the exfoliated MoS₂ nanoflakes at different exfoliation durations. (B) Wavenumber difference of the E_{2g}^1 and A_{1g} Raman modes as a function of SAW exposure time.

The binding energies of the samples were studied using XPS. The results for the bulk powder and 25 min SAW exfoliated samples are presented in Figure 3-8. Both samples show doublet Mo 3d_{5/2} and Mo 3d_{3/2} peaks at 229.4 and 232.6 eV, respectively. The binding energies of the S doublet were also seen at 162.2 and 163.1 eV, representing S 2p_{3/2} and 2p_{1/2}, respectively. This means that the exfoliated materials were comprised of stoichiometric MoS₂ and that the exfoliation process did not deteriorate the quality of the flakes.

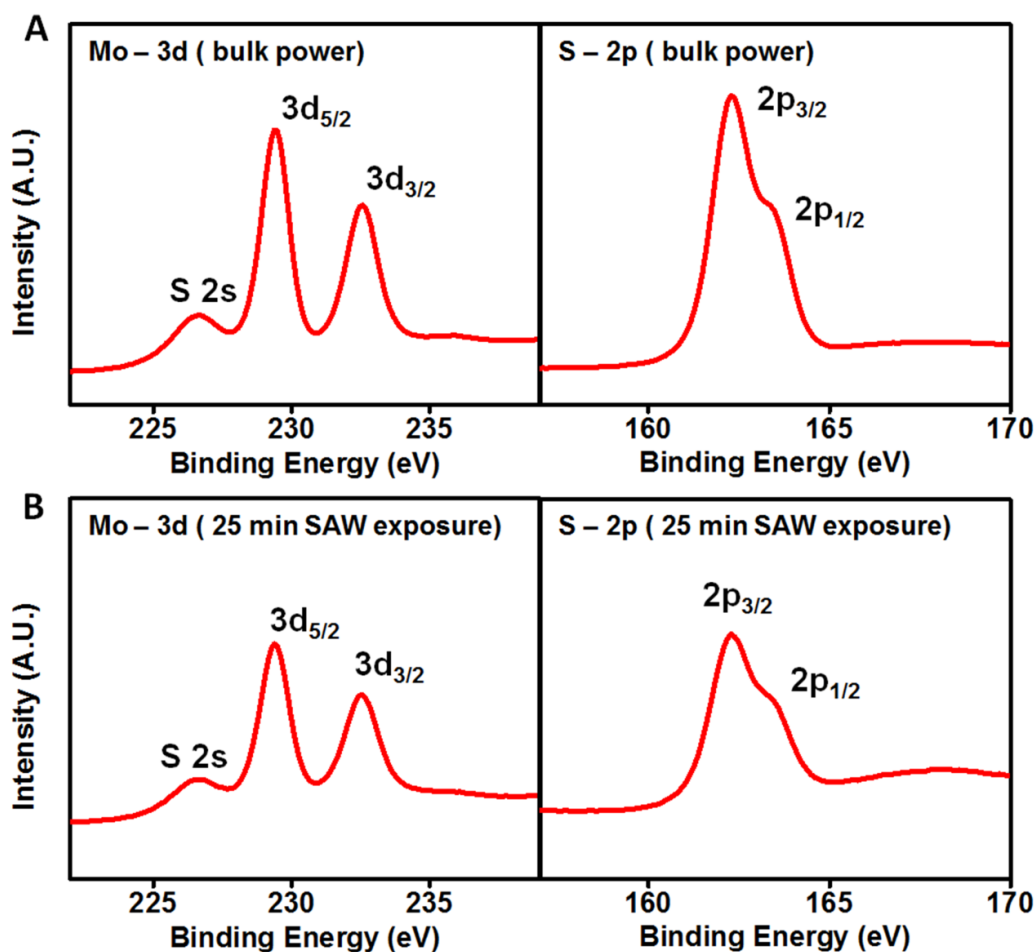


Figure 3-8 XPS of MoS₂. (A) Bulk powder and (B) 25 min SAW exfoliated samples. In both cases, carbon 1s peak located at 284.50 eV used as a reference to align the spectra.

Thermogravimetric analysis (TGA) was utilised for the yield estimation⁴² (Figure 3-9). Approximately 0.6 mL of initial 25 min SAW exfoliated solution was centrifuged at 1000 rpm for 30 min to remove the bulk residues. The supernatant of the centrifuged solution collected in a centrifuge tube. This collected supernatant solution then centrifuged twice at high speed (15,000 rpm) for 90 min. The supernatant of high speed centrifuged solution was removed, and precipitant at the bottom was used for TGA, which was performed on a PerkinElmer TGA Pyris 7 by heating the sample in the presence of N₂ gas (Figure 3-9). The concentration of the exfoliated MoS₂ nanoflakes was measured as $\sim 32 \mu\text{g mL}^{-1}$ that translates into $\sim 3.816 (\%)/\text{h}$ yield per unit of time obtained at 1,000 rpm centrifugation.

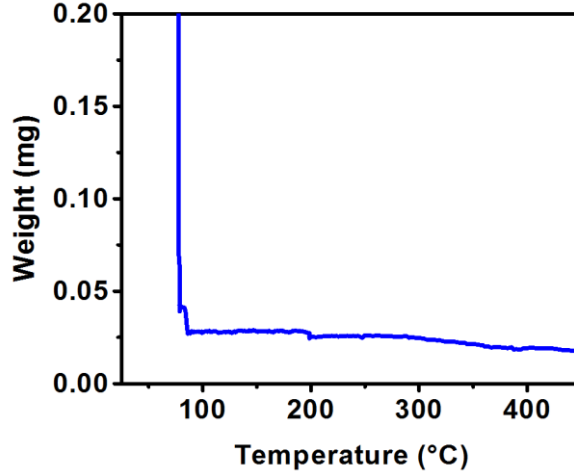


Figure 3-9 TGA of 2D MoS₂ flakes prepared after 25 min of SAW exfoliation in the presence of nitrogen gas. The final concentration was calculated at 400 °C.

Yield per unit time was calculated using the following formula:

$$\text{Yield (\%)} \text{ per unit time} = \frac{\frac{\text{Final concentration (from TGA)}}{\text{Initial concentration}} \times 100}{\text{Time in hour}}$$

Figure 3-10A presents an illustration of MoS₂ centrosymmetric even layers and non-centrosymmetric odd layers. Figure 3-10B shows the relative proportion of the number of fundamental layers in the 2D MoS₂ flakes after 25 min of SAW exfoliation. Extracted from the results in Figure 3-5F, approximately 58% of the produced flakes are monolayer, as presented in Figure 3-10B. Based on the calculations, this exfoliation takes place under an applied electric field of on average 10^5 V m^{-1} generated by the SAW device. This electric field was estimated from the applied voltage (14 V) across the IDTs, the width of the IDT finger pairs and the possible penetration depth of the wave into the aqueous media²⁰.

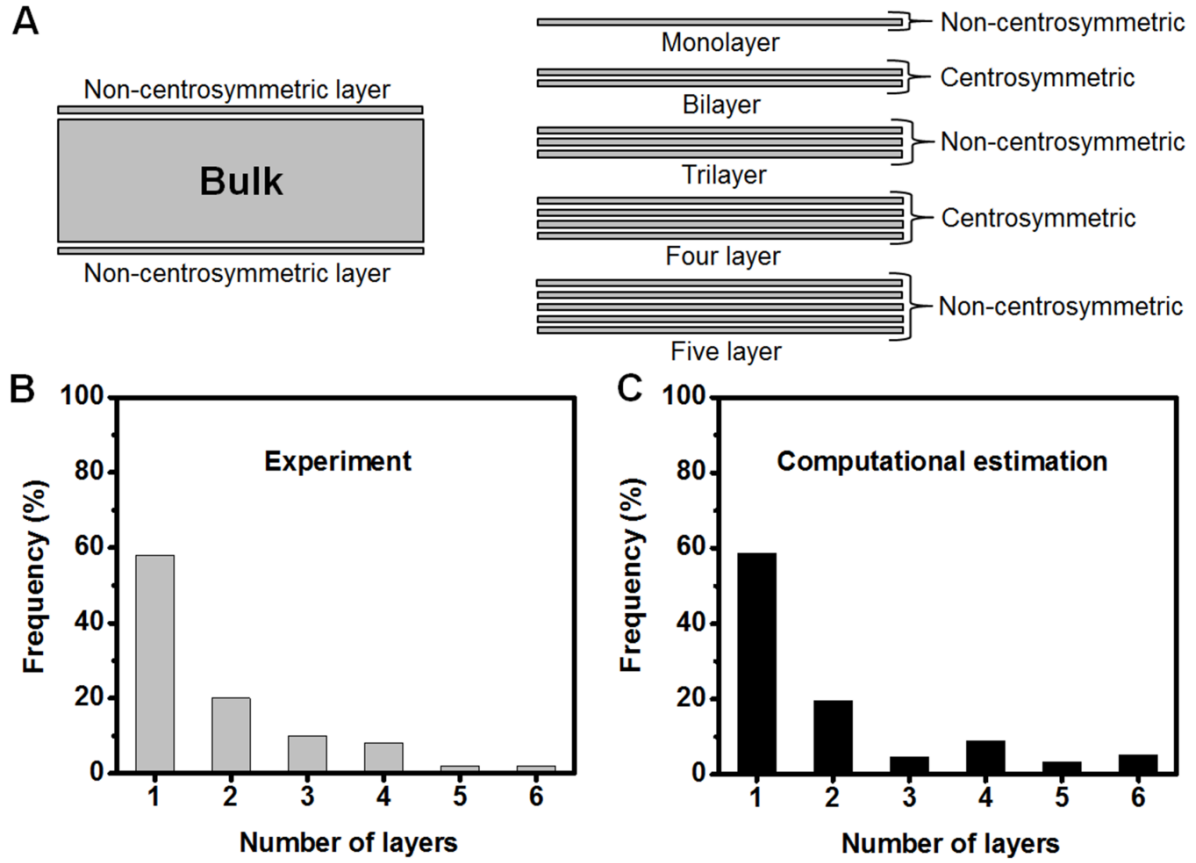


Figure 3-10 Computational estimation and validation of exfoliation. (A) Illustration of centrosymmetric and non-centrosymmetric MoS₂ layers. (B) The number of layers in the 25 min SAW exposed sample obtained from the AFM thickness distribution estimation compared with (C) exfoliation of 9-layer nanoflakes under the influence of electric field in the computational estimation.

To understand the mechanism that underpins the SAW exfoliation process, a computational assessment was conducted. In the model, the exfoliation is mediated by the electric displacement under an applied electric field was assumed. This would only occur if a structure is non-centrosymmetric (*i.e.*, it has no inversion symmetry). Group theory reveals that flakes of MoS₂ with an odd number of layers are non-centrosymmetric and thereby exhibits piezoelectricity, while sheets with even number of layers of MoS₂ have fundamental planes that are centrosymmetric and are therefore not piezoelectric²². Therefore, a further assumption in the model is that once an even-numbered layer has been created, no further exfoliation of that nanoflake can occur. Additionally, electric fields induced displacement between MoS₂

fundamental planes is only possible when the thickness of odd layer of nanoflakes are reasonably low ($7 < \text{layers}$) to exhibit appreciable piezoelectricity²².

As a simplifying assumption, the numbers of layers in bulk can be considered for computation. Here the example for 9 layers is shown than can be extended to smaller numbers (highly likely as piezoelectricity increases) or larger numbers (less likely as the thickness is closer to bulk and piezoelectricity drops) using the same method. As can be seen in Figure 3-11, exfoliation events can be continued through to a maximum of 4 exfoliation steps (labelled as “branch layers” in Figure 3-11). The possibility of single and double exfoliation events is considered. In this example, starting from a 9-layer nanoflake the exfoliation possibilities include 8-1, 7-2, 6-3, 5-4 as single exfoliation events and 7-1-1, 5-3-1, 3-3-3 as double exfoliation events. A single exfoliation event can be labelled as $(k | k-n, n)$ which means a k -layer MoS_2 slab has exfoliated into $k-n$ layer slab and n -layer slab. Similarly, double exfoliation events are labelled as $(k | k-n_1-n_2, n_1, n_2)$.

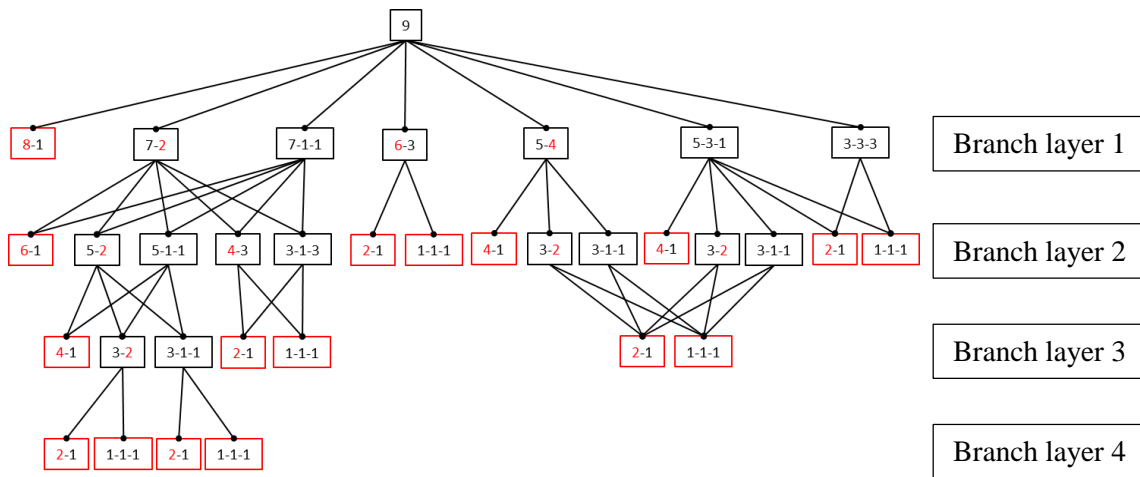


Figure 3-11 Exfoliation from a 9 layer nanoflake through to a 1 layer. The possible pathways of exfoliation can proceed through 4 successive exfoliation steps (branch layers 1-4). No further exfoliation for even number nanoflakes (labelled in red in the diagram) is considered once created.

Mathematically, an exfoliation proportional probability weighting (P) is associated with each of the events using in an n layer system as:

$$p \propto e^{-\frac{|\Delta E|}{kT}} \quad (1)$$

Where k is the Boltzmann's constant and T is the temperature and ΔE is the difference of exfoliation energy before and after the exfoliation event as calculated using a hybrid DFT computation (B3LYP). Under the 9-layer assumption, possible pathways for single and double exfoliation events are represented in Figure 3-11. Exfoliation events continue when the outcome contains odd number of layers. They stop when exfoliation result in either even or monolayer flakes. A description of the calculation of exfoliated MoS₂ layers frequency, with the number of layers, is presented in the subsequent section.

For each branch layer, a probability (P) is assigned for each single exfoliation event ($k | k-n, n$) by:

$$P(k|k-n, n) = A \exp\left(-\frac{|\Delta E(k|k-n, n)|}{kT}\right) \quad (2)$$

$$\Delta E(k|k-n, n) = E_{B3LYP}(k) - (E_{B3LYP}(k-n) + E_{B3LYP}(n)) \quad (3)$$

Where $E_{B3LYP}(k)$, $E_{B3LYP}(k-n)$ and $E_{B3LYP}(n)$ are the Density Function Theory (B3LYP) calculated energies for the k , $k-n$ and n layered slab respectively, T is the temperature (⁰K), k is the Boltzmann constant and A is a normalisation constant.

Similarly, for each double exfoliation event ($k | k-n_1-n_2, n_1, n_2$) the probabilities are given by:

$$P(k|k-n_1-n_2, n_1, n_2) = A \exp\left(-\frac{|\Delta E(k|k-n_1-n_2, n_1, n_2)|}{kT}\right) \quad (4)$$

$$\Delta E(k|k-n_1-n_2, n_1, n_2) = E_{B3LYP}(k) - (E_{B3LYP}(k-n_1-n_2) + E_{B3LYP}(n_1) + E_{B3LYP}(n_2)) \quad (5)$$

It is assumed that each exfoliation event is independent; therefore, as a slab continues to undergo successive exfoliation events through the branch layers of the tree diagram, the total probability of an outcome is the product of the probability of formation at each branch layer. The frequency spectrum (Figure 3-10C) is obtained in the following way:

1. For each outcome event in the tree diagram, the probability of the event (as outlined above) and multiply that value by the number of layers that are formed from that event is calculated. For example, there are 9 single layer slabs created through the pathway $(9|3,3,3) \rightarrow (3|1,1,1)$ since there are three 3-layer slabs created in the $(9|3,3,3)$ event (branch layer 1), and each of the three layered slabs can give rise to three 1-layer slabs through the $(3|1,1,1)$ event.
2. For a particular layer number (for example 2-layer slabs), the frequency value of that layer as a sum of values (as determined in step 1) of all the outcomes that give that particular layer value is calculated.
3. Finally, all the frequency values for all the layers are renormalised so that all of the frequency values sum to 100 %.

The computational outcomes are presented in Figure 3-10C, which is in good agreement with the measurements. For instance, the ratio of monolayer MoS₂ in experiment and computation estimations are ~58% and ~59%, respectively. The slight discrepancies between the experiment and computation estimation of other flake numbers may originate from the fact that shear exfoliation, which was not considered in the computational estimation, still plays an important role in the exfoliation process.

Shear rate is crucial for the exfoliation of monolayer using probe sonication or turbulent based techniques^{6, 43, 44}. In reports based on such techniques, efficient exfoliation to ultrathin layers

generally occurs when the shear rate exceeds the threshold value of $\sim 10^4 \text{ s}^{-1}$ ^{6, 43, 44}. Considering streaming velocity of microcentrifugation SAW device and diameter of the PDMS reservoir, shear rate produced in the microcentrifugation SAW device is $\sim 10^2 \text{ s}^{-1}$, which is relatively low.

To investigate the exfoliation characteristics of MoS₂ nanoflakes using microcentrifugation SAW device in the absence of electric field, a thin 100 nm gold (Au) layer (with 30 nm chromium adhesion layer) deposited between the PDMS reservoir and lithium niobate substrate (Figure 3-12A inset). This metallic layer screens and prevents electric field exposure to MoS₂ particles. Flakes thickness distribution histogram shown in Figure 3-12A represents the exfoliation of MoS₂ (25 min) with and without the presence of an electric field. As can be seen, shear force exfoliation (in red), with no electric field, has larger median value for the flakes thickness (4.3 nm) in comparison with the presence of electric field (1.4 nm). This red bars distribution is very similar to previous experiments using the shear force only, confirming that electric field is not present⁷. The experiment also shows the increased efficiency of the exfoliation process in the presence of electric field. Figure 3-12B shows the corresponding lateral dimension histograms of flakes of Figure 3-12A. As can be seen, the average lateral dimension of the exfoliated samples in the presence of electric field is larger than that of only shear force exfoliation. It seems that electric field helps in the more efficient exfoliation of the crystal before they are broken down by the shear force. Therefore, both experiment and computational analysis suggest that the electric field plays a dominant role in exfoliating MoS₂ to ultrathin layers.

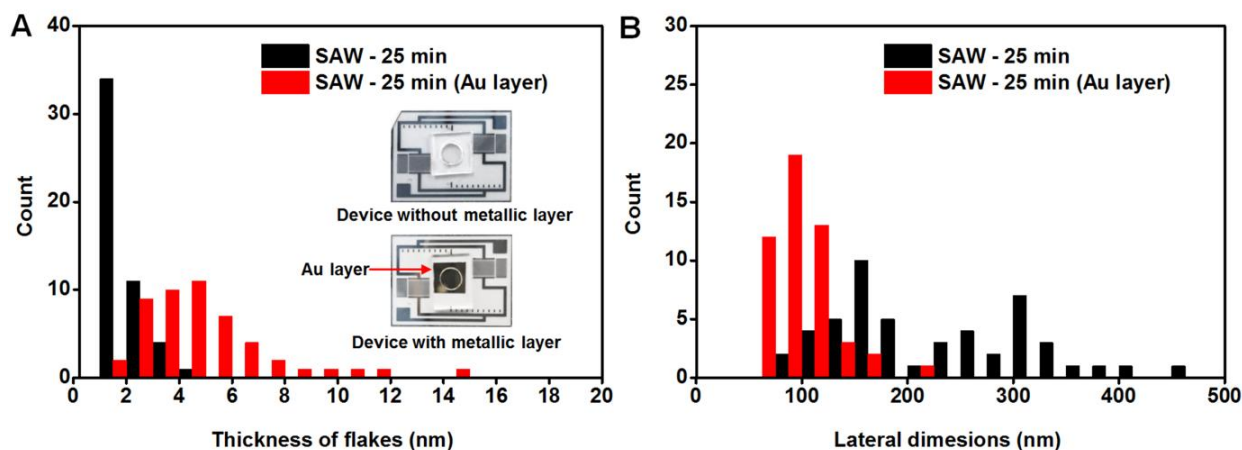


Figure 3-12 Comparison of shear force only exfoliation with electric field-assisted exfoliation. (A) AFM Thickness distribution histograms of MoS₂ flakes (25 min) with (black) and without (red) the presence of electric field. Inset shows microcentrifugation SAW device coated with Au layer underneath the PDMS reservoir and device without any metallic layer. (B) Flakes lateral dimension histograms.

The efficiency of the developed technique is compared with a few selected previous works in terms of the median number of layers, the run time and the yield per unit of time (Table 3-1). To facilitate consistency in the comparison, the data in the table only focuses on liquid exfoliation techniques with surfactants or chemical solvents, without the incorporation of any assisting chemically active reagents (such as butyllithium and sodium hydroxide). As can be seen, the proposed method here has the best exfoliation efficiency in an impressively short time, resulting in approximately 58% monolayer MoS₂ flakes. In this work, the yield is high, reaching a yield per unit of time of 3.816/h. This is higher than that of previous reports for sonication methods with surfactant or N-Methyl-2-pyrrolidone (NMP) as a solvent. Such efficiency can be ascribed to the ability to exploit the piezoelectricity of the non-centrosymmetric material, given the presence of the electric field that accompanies the mechanical shear, which is not possible with other methods.

Table 3-1 Comparison of exfoliation efficiency. Comparison of the exfoliation efficiency of MoS₂ prepared in this work with that produced from selected other comparable single-step liquid exfoliation methods.

Exfoliation methods, chemical used	Median number of layers	Run time	Yield per unit of time (%)/h	Reference
Liquid exfoliation using SAW with aqueous surfactant	1	25 min	3.816	This work
Liquid exfoliation using blender with aqueous surfactant	2 to 12	2 h	0.400	7
Probe sonication with aqueous surfactant	4	16 h	0.625	45
Probe sonication with NMP	-	7 h	0.285	46
Probe sonication with NMP	-	140 h	0.290	5

3.4 Conclusions

In brief, unlike conventional exfoliation methods, a compact microcentrifugation SAW device was developed that applies a concomitant electric field, and mechanical shear force for efficient exfoliation of monolayer enrich MoS₂ suspension. Overall, a yield per unit of time of 3.816 (%)/h was achieved utilising the developed SAW system, which is at least 5 times higher than the best previously reported value. High accelerating acoustic wave-induced shear streaming reduces the thickness of MoS₂. Through the experimental realisation and computational estimation, it was shown that the electric field plays a critical role in increasing the efficiency of the exfoliation process due to the intrinsic piezoelectric nature of non-centrocymmetric layered MoS₂. The thickness of MoS₂ can be modulated by increasing the SAW exfoliation duration, as revealed by the AFM images which show the existence of a high percentage of MoS₂ monolayers. Further optimisation studies on the design and development of the device is expected to improve production efficiency.

The SAW system reveals the possibility of micro-scale routes for the versatile exfoliation of non-centrosymmetric layered materials and also alludes to the significant possibility of exploiting the electric field to increase the efficiency of these exfoliation processes. The process can be applied to a large number of layered crystals, including transition metal oxides and chalcogenides. A list of possible candidates is presented in the works by Duerloo et al. and Blonsky et al.^{21,47}. Additionally, many more layered crystals should be explored and identified based on the selection criteria of non-centrosymmetric condition. Centrosymmetric materials are nonpiezoelectric (e.g., graphene); therefore, exfoliation of such materials will not be as effective as non-centrosymmetric materials using the SAW method⁴⁸. In the following chapter, an alternative method of agitative exfoliation and co-applied electric field will be investigated.

References

1. Nicolosi, V., Chhowalla, M., Kanatzidis, M. G., Strano, M. S., Coleman, J. N., Liquid exfoliation of layered materials. *Science* **2013**, *340* (6139), 1226419.
2. Chen, Y., Tan, C., Zhang, H., Wang, L., Two-dimensional graphene analogues for biomedical applications. *Chem. Soc. Rev.* **2015**, *44* (9), 2681-2701.
3. Ferrari, A. C., Bonaccorso, F., Fal'ko, V., Novoselov, K. S., Roche, S., Boggild, P., Borini, S., Koppens, F. H. L., Palermo, V., Pugno, N., et al., Science and technology roadmap for graphene, related two-dimensional crystals, and hybrid systems. *Nanoscale* **2015**, *7* (11), 4598-4810.
4. Novoselov, K. S., Jiang, D., Schedin, F., Booth, T. J., Khotkevich, V. V., Morozov, S. V., Geim, A. K., Two-dimensional atomic crystals. *Proc. Natl. Acad. Sci. U.S.A.* **2005**, *102* (30), 10451-10453.

5. O'Neill, A., Khan, U., Coleman, J. N., Preparation of high concentration dispersions of exfoliated MoS₂ with increased flake size. *Chem. Mater.* **2012**, *24* (12), 2414-2421.
6. Paton, K. R., Varrla, E., Backes, C., Smith, R. J., Khan, U., O'Neill, A., Boland, C., Lotya, M., Istrate, O. M., King, P., et al., Scalable production of large quantities of defect-free few-layer graphene by shear exfoliation in liquids. *Nat. Mater.* **2014**, *13* (6), 624-630.
7. Varrla, E., Backes, C., Paton, K. R., Harvey, A., Gholamvand, Z., McCauley, J., Coleman, J. N., Large-scale production of size-controlled MoS₂ nanosheets by shear exfoliation. *Chem. Mater.* **2015**, *27* (3), 1129-1139.
8. Yao, Y., Lin, Z., Li, Z., Song, X., Moon, K.-S., Wong, C.-p., Large-scale production of two-dimensional nanosheets. *J. Mater. Chem.* **2012**, *22* (27), 13494-13499.
9. Kim, J., Kwon, S., Cho, D.-H., Kang, B., Kwon, H., Kim, Y., Park, S. O., Jung, G. Y., Shin, E., Kim, W.-G., et al., Direct exfoliation and dispersion of two-dimensional materials in pure water *via* temperature control. *Nat. Commun.* **2015**, *6*, 8294.
10. Yao, Y., Tolentino, L., Yang, Z., Song, X., Zhang, W., Chen, Y., Wong, C. p., High-concentration aqueous dispersions of MoS₂. *Adv. Funct. Mater.* **2013**, *23* (28), 3577-3583.
11. Fan, X., Xu, P., Li, Y. C., Zhou, D., Sun, Y., Nguyen, M. A. T., Terrones, M., Mallouk, T. E., Controlled exfoliation of MoS₂ crystals into trilayer nanosheets. *J. Am. Chem. Soc.* **2016**, *138* (15), 5143-5149.
12. Fan, X., Xu, P., Zhou, D., Sun, Y., Li, Y. C., Nguyen, M. A. T., Terrones, M., Mallouk, T. E., Fast and efficient preparation of exfoliated 2H MoS₂ nanosheets by sonication-assisted lithium intercalation and infrared laser-induced 1T to 2H phase reversion. *Nano Lett.* **2015**, *15* (9), 5956-5960.

13. Ramakrishna Matte, H. S. S., Gomathi, A., Manna, A. K., Late, D. J., Datta, R., Pati, S. K., Rao, C. N. R., MoS₂ and WS₂ analogues of graphene. *Angew. Chem. Int. Ed.* **2010**, *49* (24), 4059-4062.
14. Wang, Y., Carey, B. J., Zhang, W., Chrimes, A. F., Chen, L., Kalantar-zadeh, K., Ou, J. Z., Daeneke, T., Intercalated 2D MoS₂ utilizing a simulated sun assisted process: reducing the HER overpotential. *J. Phys. Chem. C* **2016**, *120* (4), 2447-2455.
15. Wang, Q. H., Kalantar-Zadeh, K., Kis, A., Coleman, J. N., Strano, M. S., Electronics and optoelectronics of two-dimensional transition metal dichalcogenides. *Nat. Nanotech.* **2012**, *7* (11), 699-712.
16. Destgeer, G., Jung, J. H., Park, J., Ahmed, H., Sung, H. J., Particle separation inside a sessile droplet with variable contact angle using surface acoustic waves. *Anal. Chem.* **2017**, *89* (1), 736-744.
17. Yeo, L. Y., Friend, J. R., Surface acoustic wave microfluidics. *Annu. Rev. Fluid Mech.* **2014**, *46* (1), 379-406.
18. Shilton, R., Tan, M. K., Yeo, L. Y., Friend, J. R., Particle concentration and mixing in microdrops driven by focused surface acoustic waves. *J. Appl. Phys.* **2008**, *104* (1), 014910.
19. Rezk, A. R., Carey, B., Chrimes, A. F., Lau, D. W. M., Gibson, B. C., Zheng, C., Fuhrer, M. S., Yeo, L. Y., Kalantar-zadeh, K., Acoustically-driven trion and exciton modulation in piezoelectric two-dimensional MoS₂. *Nano Lett.* **2016**, *16* (2), 849-855.
20. Miansari, M., Qi, A., Yeo, L. Y., Friend, J. R., Vibration-induced deagglomeration and shear-induced alignment of carbon nanotubes in air. *Adv. Funct. Mater.* **2015**, *25* (7), 1014-1023.
21. Duerloo, K.-A. N., Ong, M. T., Reed, E. J., Intrinsic piezoelectricity in two-dimensional materials. *J. Phys. Chem. Lett.* **2012**, *3* (19), 2871-2876.

22. Wu, W., Wang, L., Li, Y., Zhang, F., Lin, L., Niu, S., Chenet, D., Zhang, X., Hao, Y., Heinz, T. F., et al., Piezoelectricity of single-atomic-layer MoS₂ for energy conversion and piezotronics. *Nature* **2014**, *514* (7523), 470-474.
23. Gracioso Martins, A. M., Glass, N. R., Harrison, S., Rezk, A. R., Porter, N. A., Carpenter, P. D., Du Plessis, J., Friend, J. R., Yeo, L. Y., Toward complete miniaturisation of flow injection analysis systems: Microfluidic enhancement of chemiluminescent detection. *Anal. Chem.* **2014**, *86* (21), 10812-10819.
24. Dovesi, R., Orlando, R., Erba, A., Zicovich-Wilson, C., Civalieri, B., Casassa, S., Maschio, L., Ferrabone, M., De La Pierre, M., D'Arco, P., CRYSTAL14: A program for the *ab initio* investigation of crystalline solids. *Int. J. Quantum Chem.* **2014**, *114* (19), 1287-1317.
25. Dovesi, R., Saunders, V., Roetti, C., Orlando, R., Zicovich-Wilson, C., Pascale, F., Civalieri, B., Doll, K., Harrison, N., Bush, I., et al., CRYSTAL14 User's Manual (University of Torino, Torino, 2014). *CRYSTAL14 User's Manual* **2014**.
26. Becke, A. D., Density-functional thermochemistry. III. The role of exact exchange. *J. Chem. Phys.* **1993**, *98* (7), 5648-5652.
27. Grimme, S., Semiempirical GGA-type density functional constructed with a long-range dispersion correction. *J. Comput. Chem.* **2006**, *27* (15), 1787-1799.
28. Civalieri, B., Zicovich-Wilson, C. M., Valenzano, L., Ugliengo, P., B3LYP augmented with an empirical dispersion term (B3LYP-D*) as applied to molecular crystals. *CrystEngComm* **2008**, *10* (4), 405-410.
29. Cora, F., Patel, A., Harrison, N. M., Roetti, C., Richard A. Catlow, C., An *ab initio* Hartree-Fock study of α -MoO₃. *J. Mater. Chem.* **1997**, *7* (6), 959-967.

30. Berean, K. J., Ou, J. Z., Daeneke, T., Carey, B. J., Nguyen, E. P., Wang, Y., Russo, S. P., Kaner, R. B., Kalantar-zadeh, K., 2D MoS₂ PDMS nanocomposites for NO₂ separation. *Small* **2015**, *11* (38), 5035-5040.
31. Ou, J. Z., Ge, W., Carey, B., Daeneke, T., Rotbart, A., Shan, W., Wang, Y., Fu, Z., Chrimes, A. F., Wlodarski, W., et al., Physisorption-based charge transfer in two-dimensional SnS₂ for selective and reversible NO₂ gas sensing. *ACS Nano* **2015**, *9* (10), 10313-10323.
32. Jiao, Z. J., Huang, X. Y., Nguyen, N. T., Scattering and attenuation of surface acoustic waves in droplet actuation. *J. Phys. A* **2008**, *41* (35), 355502.
33. Li, H., Friend, J. R., Yeo, L. Y., Surface acoustic wave concentration of particle and bioparticle suspensions. *Biomed Microdevices* **2007**, *9* (5), 647-656.
34. Rezk, A. R., Ramesan, S., Yeo, L. Y., Plug-and-actuate on demand: multimodal individual addressability of microarray plates using modular hybrid acoustic wave technology. *Lab Chip* **2018**, *18* (3), 406-411.
35. Kang, J., Seo, J.-W. T., Alducin, D., Ponce, A., Yacaman, M. J., Hersam, M. C., Thickness sorting of two-dimensional transition metal dichalcogenides *via* copolymer-assisted density gradient ultracentrifugation. *Nat. Commun.* **2014**, *5*, 5478.
36. Bang, G. S., Nam, K. W., Kim, J. Y., Shin, J., Choi, J. W., Choi, S.-Y., Effective liquid-phase exfoliation and sodium ion battery application of MoS₂ nanosheets. *ACS Appl. Mater. Interfaces* **2014**, *6* (10), 7084-7089.
37. Lee, C., Yan, H., Brus, L. E., Heinz, T. F., Hone, J., Ryu, S., Anomalous lattice vibrations of single- and few-layer MoS₂. *ACS Nano* **2010**, *4* (5), 2695-2700.
38. Coleman, J. N., Lotya, M., O'Neill, A., Bergin, S. D., King, P. J., Khan, U., Young, K., Gaucher, A., De, S., Smith, R. J., et al., Two-dimensional nanosheets produced by liquid exfoliation of layered materials. *Science* **2011**, *331* (6017), 568-571.

39. Wu, J.-Y., Lin, M.-N., Wang, L.-D., Zhang, T., Photoluminescence of MoS₂ prepared by effective grinding-assisted sonication exfoliation. *J. Nanomater.* **2014**, 2014, 852735.
40. Tang, Y., Zhang, X., Choi, P., Manica, R., Liu, Q., Xu, Z., Single-molecule MoS₂–polymer interaction and efficient aqueous exfoliation of MoS₂ into single layer. *J. Phys. Chem. C* **2018**, 122 (15), 8262-8269.
41. Eda, G., Yamaguchi, H., Voiry, D., Fujita, T., Chen, M., Chhowalla, M., Photoluminescence from chemically exfoliated MoS₂. *Nano Lett.* **2011**, 11 (12), 5111-5116.
42. Alsaif, M. M. Y. A., Field, M. R., Daeneke, T., Chrimes, A. F., Zhang, W., Carey, B. J., Berean, K. J., Walia, S., van Embden, J., Zhang, B., et al., Exfoliation solvent dependent plasmon resonances in two-dimensional sub-stoichiometric molybdenum oxide nanoflakes. *ACS Appl. Mater. Interfaces* **2016**, 8 (5), 3482-3493.
43. Feng, X., Binghui, G., Jing, C., Arokia, N., Linhuo, L. X., Hongyu, M., Huihua, M., Chongyang, Z., Weiwei, X., Zhengrui, L., et al., Scalable shear-exfoliation of high-quality phosphorene nanoflakes with reliable electrochemical cycleability in nano batteries. *2D Mater.* **2016**, 3 (2), 025005.
44. Varrla, E., Paton, K. R., Backes, C., Harvey, A., Smith, R. J., McCauley, J., Coleman, J. N., Turbulence-assisted shear exfoliation of graphene using household detergent and a kitchen blender. *Nanoscale* **2014**, 6 (20), 11810-11819.
45. Smith, R. J., King, P. J., Lotya, M., Wirtz, C., Khan, U., De, S., O'Neill, A., Duesberg, G. S., Grunlan, J. C., Moriarty, G., et al., Large-scale exfoliation of inorganic layered compounds in aqueous surfactant solutions. *Adv. Mater.* **2011**, 23 (34), 3944-3948.
46. Finn, D. J., Lotya, M., Cunningham, G., Smith, R. J., McCloskey, D., Donegan, J. F., Coleman, J. N., Inkjet deposition of liquid-exfoliated graphene and MoS₂ nanosheets for printed device applications. *J. Mater. Chem. C* **2014**, 2 (5), 925-932.

47. Blonsky, M. N., Zhuang, H. L., Singh, A. K., Hennig, R. G., *Ab initio* prediction of piezoelectricity in two-dimensional materials. *ACS Nano* **2015**, 9 (10), 9885-9891.
48. Ahmed, H., Rezk, A. R., Carey, B. J., Wang, Y., Mohiuddin, M., Berean, K. J., Russo, S. P., Kalantar-zadeh, K., Yeo, L. Y., Ultrafast acoustofluidic exfoliation of stratified crystals. *Adv. Mater.* **2018**, 30 (20), 1704756.

Chapter 4

Exploring electric field assisted van der Waals weakening of stratified crystals†

† The contents of this chapter is published in Mohiuddin et al., Exploring electric Field Assisted van der Waals Weakening of Stratified Crystals, *Applied Materials Today*, 2018, 12, 359-365.

4.1 Introduction

It has been presented in chapter 3, that the concomitant mechanical and electric field generated by an external piezoelectric substrate can enhance the exfoliation process. The monolayer TMDs such as molybdenum disulphide (MoS_2) and tungsten disulphide (WS_2) have inherent piezoelectricity due to the lack of centrosymmetry, while ideal bulk TMDs are symmetric and do not show piezoelectricity¹⁻⁶. To date, no studies have been conducted on understanding the direct application of electric field exploiting the piezoelectricity during the liquid-phase mechanical exfoliation of TMDs. External electric field on the nature of match between the dispersive component of surface energy may influence the distribution of the field on the boundaries. In this chapter, external electric field for enhancing liquid-phase sonication exfoliation of MoS_2 and WS_2 layers (also non-piezoelectric graphene as a reference) has been investigated. Considering the more effective influence of electric field on the exfoliation efficiency of WS_2 , characterisation and electrocatalytic HER proof-of-concept have been presented for this material.

4.2 Experimental section

4.2.1 Materials

WS₂ (2 µm, 99%) powder, graphite flakes (+100 mesh) and dimethylformamide (DMF, 99.8%) were purchased from Sigma-Aldrich. MoS₂ (0.8-1.2 µm, 99%) powder was purchased from US-nano. Sulfuric acid, H₂SO₄ (≥99%, Sigma-Aldrich), polytetrafluoroethylene, PTFE (60 wt%, Sigma-Aldrich), carbon paper (CP). All the reagents were used as received without any further purification.

4.2.2 Synthesis

An in-house built system was utilised to the apply electric field. For the system 0.5 mm thick perforated stainless steel sheet was used for preparing outer and inner electrodes. Diameters of outer and inner electrodes were 41 mm and 27 mm, respectively. These electrodes were housed into a machined high-density polyethylene (HDPE) container.

Each time 2 mg/ml of bulk powder was prepared in 20 ml of solvent and taken into the HDPE container for exfoliation. For exfoliation experiments, the solution was tip sonicated with and without electric field (nitrogen purged). The electric field (sinusoidal, 1.5 kHz) was applied using a voltage amplifier (Trek 677A). The sonication was performed for 30 min (unless stated otherwise) by a probe sonicator (Q500, QSONICA, 1/2" diameter probe, 500 W and 20 kHz frequency) using 25% amplitude of power with 8 s on and 2 s off pulses. To remove the unexfoliated materials, exfoliated solutions were centrifuged (Labogene 1524M-ScanSpeed) at 1000 rpm for 30 min, and supernatants (top 50%) were collected for further characterisation.

4.2.3 Characterisations

The TEM for histogram was performed in JEOL 1010 at 100 kV accelerating voltage. The crystal structure and lattice properties of exfoliated nanoflakes were evaluated by JEOL 2010F at 200 kV accelerating voltage. The samples were drop-casted onto holey carbon grids for the TEM analysis. Perkin Elmer Lambda 1050 spectrophotometer and quartz cuvette of 10 mm

path length were used to perform optical absorbance of samples. The thickness and surface roughness of nanoflakes were measured using a Bruker Dimension Icon AFM in ScanAsyst air mode, 10 μL of solution (centrifuged at 2000 rpm, Eppendorf - 5702) was drop-casted onto silicon (Si) substrates. The SEM image of bulk WS_2 powder presented in Figure 4-1(a) was examined using a Verios 460L field-emission SEM. Raman and PL spectrometry of drop-casted WS_2 were conducted using Horiba Scientific LabRAM HR evolution Raman. For Raman and photoluminescence (PL) measurements, the samples were drop-casted onto gold-coated Si wafers. For the Raman spectrometry the samples were excited with a 532 nm laser. The measurements were conducted using a 50 \times lens and 1800/mm grating. The PL measurements were conducted using the same instrument as for the Raman characterisations, using 150 grating/1200 nm. The XRD patterns were collected using a Bruker D8 DISCOVER microdiffractometer fitted with a general area detector diffraction system. Data were collected with a potential of 40 kV and a current of 40 mA featuring a Cu $\text{K}\alpha$ X-ray source ($\lambda = 0.154$ nm). Zeta potentials were performed in Malvern Nano ZS Zetasizer. All measurements were performed under ambient conditions.

4.2.4 Electrochemical measurements

Hydrogen evolution reaction was performed using a three-electrode configuration (CHI 760D) in 0.5 M H_2SO_4 (pH = 0.3) electrolyte. Carbon paper (CP) coated with the sample, graphite rod, and Ag/AgCl (in 1 M KCl aqueous solution) were used as working electrode, counter electrode, and a reference electrode, respectively. The carbon paper was cleaned properly with ethanol and DI water before use. All the potentials shown in this paper were converted to RHE and all the polarisation curves were iR corrected. The presented current density was normalised to the geometric surface area. Linear sweep voltammetry was performed at a 5 mV s^{-1} scan rate to obtain the polarisation curves. All the tests were conducted at room temperature and ambient pressure. Inks of WS_2 nanosheets were prepared by mixing 2 mg of materials powder

and carbon black at 80% and 20% ratio in IPA and DI water mixture (1:1). 6 μL PTFE solution (60% in H_2O , Sigma) was added followed by sonication for 10 min. Around 100 μL of the suspension was drop-casted onto a carbon paper with an area of 0.25 cm^2 . Electrochemical cyclic voltammetry measurements for determining electrochemical double-layer capacitors (EDLC) were performed over a range of scan rates (10, 20, 30, 40, and 50 mV s^{-1}) at 0.15 V vs RHE.

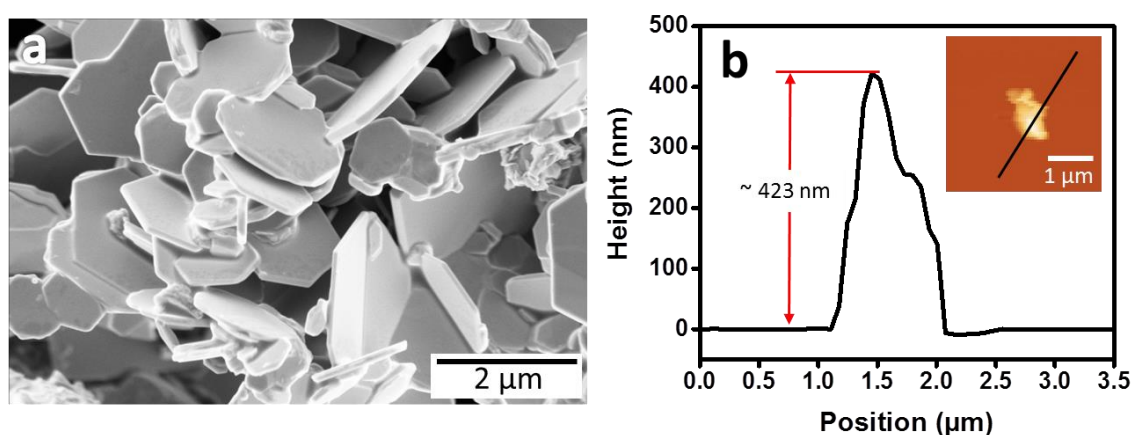


Figure 4-1 (a) SEM microstructure of the as-purchased bulk WS_2 powder. (b) AFM thickness profile of a typical WS_2 grain with the inset showing the AFM image.

4.3 Results and discussion

Schematically shown in Figure 4-2(a) is the apparatus that generates an electric field using two concentric electrodes. Figure 4-2(b), (c) present the actual images of the system. Approximately 20 ml solution can be included in a single run using this system. Liquid suspensions with no electric field applied, 0.1 kV mm^{-1} and 0.2 kV mm^{-1} electric field-assisted sonication were prepared. The mechanical power of 125 W was applied to the probe sonicator for 30 min in the process (Materials and methods). After the exfoliation, the samples to which the electric field was applied show increase in exfoliation concentrations of WS_2 in DMF.

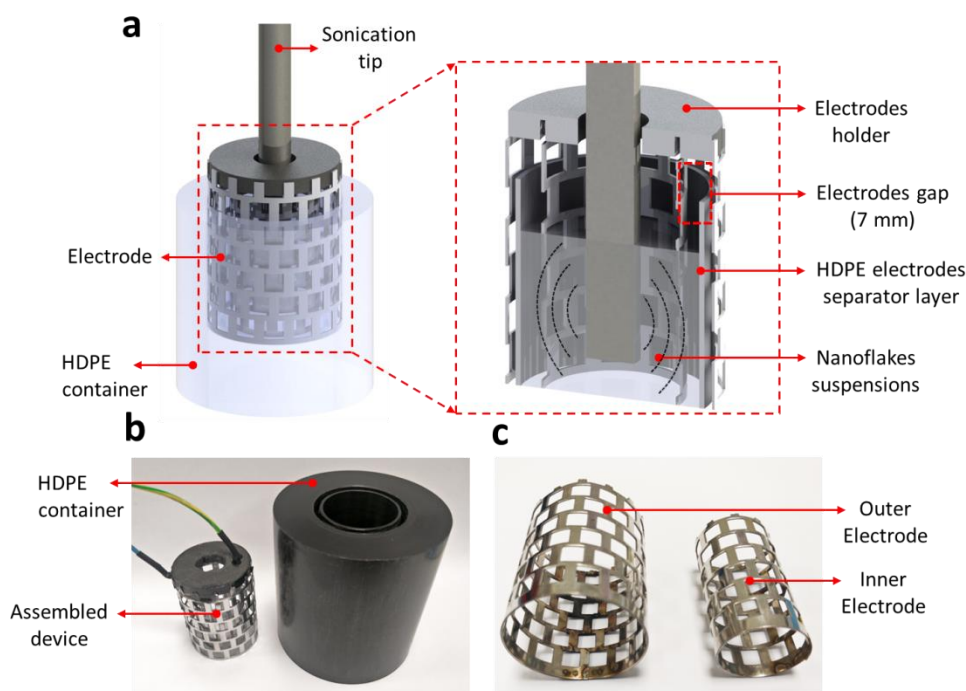


Figure 4-2 Electric field-assisted liquid-phase exfoliation. (a) Schematic illustration of the experimental procedure for synthesising nanoflakes by liquid-phase exfoliation using simultaneous electric field and probe sonication. HDPE container is used to exfoliate 20 ml solution. (b) Assembled device and HDPE container, device is used to apply electric field has two concentric electrodes with a gap 7 mm between the electrodes. (c) Disassembled outer and inner electrodes.

Figure 4-3(a) and (c) display the exfoliated WS_2 and MoS_2 suspensions after centrifugation at 1000 rpm. The concentration estimate and optical properties of the exfoliated WS_2 nanoflakes were characterised by ultraviolet-visible (UV-vis) absorption spectroscopy (Figure 4-3(b)). The samples exhibit three distinct exciton absorption peaks of A, B, and C at approximately 630, 524, and 460 nm, respectively, which is in good agreement with previous reports^{7, 8}. Excitonic A, B, and C peaks confirm that external electric field does not cause any phase-transitions or defects in the exfoliated WS_2 ^{8, 9}. The electric field-assisted exfoliated 2D WS_2 shows a substantial increase in the intensity of the entire wavelength range in comparison to the samples synthesised using only probe sonication. As the dimensional aspects of the flakes are further reduced under electric field (shown later) the increase of the 2D material's concentration according to Beer-Lambert law becomes more pronounced. The concentration

of the as exfoliated WS₂ suspensions were calculated from excitonic A absorption peak of UV-vis spectra as per described in previous reports¹⁰⁻¹². The yields of exfoliated WS₂ suspensions were calculated to be 2.3, 3.2, and 4.6 µg/ml for no field, 0.1 kV mm⁻¹, and 0.2 kV mm⁻¹, respectively.

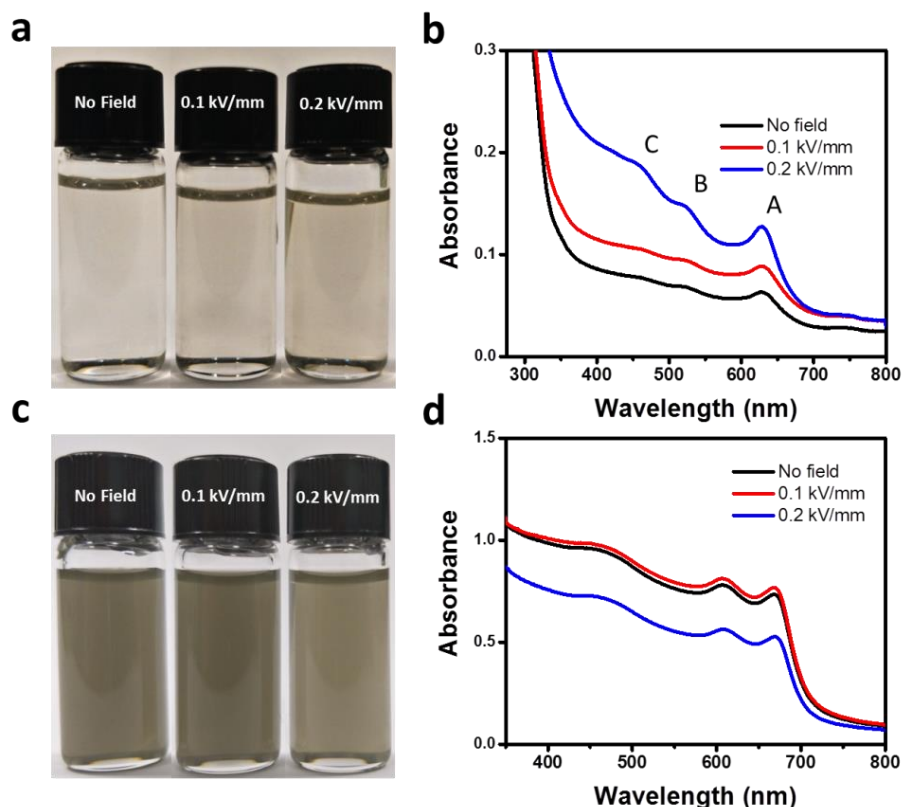


Figure 4-3 (a, c) Exfoliated WS₂, MoS₂ suspensions and (b, d) UV-vis spectra of exfoliated WS₂, MoS₂ suspensions.

To understand the exfoliation efficiency in the time domain, WS₂ nanoflakes dispersion concentration is investigated for both no field and with applied electric field (0.1 kV mm⁻¹) at different processing time. Dispersions concentration at different processing time of 10, 30, 60, and 90 min is represented in Figure 4-4. For both no field and applied electric field, the concentration increases with the increase of time. Both curves show nonlinear behaviour with the processing time. It appears that the exfoliation with the presence of electric field is more effective than sonication only exfoliation.

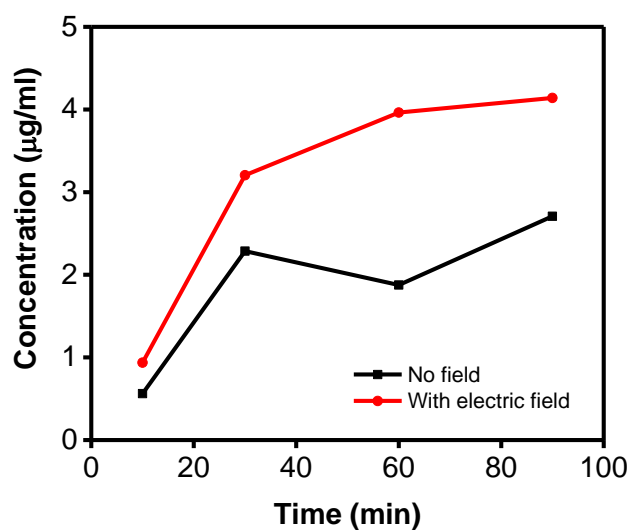


Figure 4-4 The concentrations of the WS₂ suspensions for no field and with an applied electric field as a function of sonication time.

These initial assessments confirmed that the electric field-assisted process has likely resulted in higher concentration and thinner flakes. Alternating electric field impacts on the surfaces of the WS₂ and help in distorting the top and bottom layers which are noncentrosymmetric and show piezoelectricity. In order to investigate the effect of solvent parameters further, three different volume ratios of isopropyl alcohol (IPA) and deionised (DI) water (10:90, 50:50 and 90:10) were prepared as the exfoliation solvent of WS₂. However, no discernible difference was observed after applying the electric field (Figure 4-5).

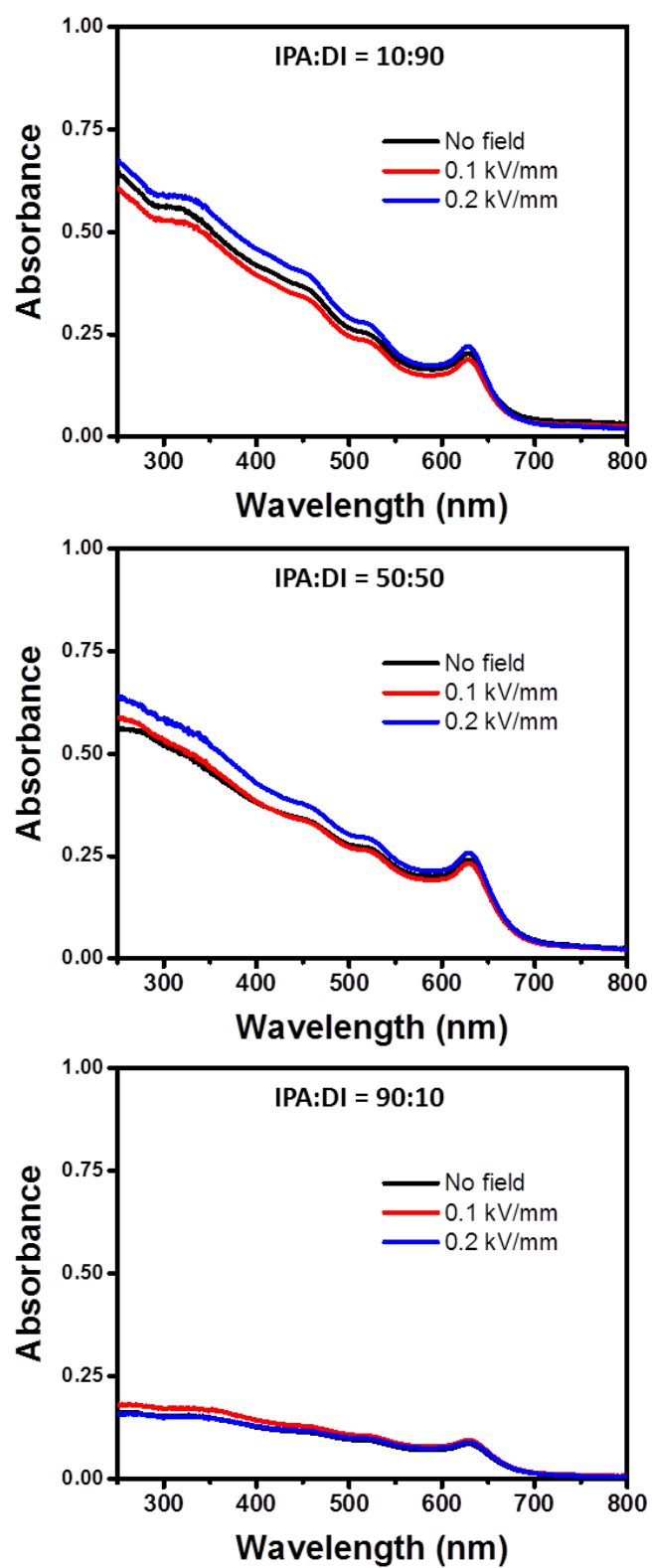


Figure 4-5 UV-vis spectra of exfoliated WS₂ for different volume ratios of IPA and DI water.

UV-vis spectra of MoS₂ presented in Figure 4-3(d). Unlike WS₂, UV-vis spectra of no field and 0.1 kV mm⁻¹ MoS₂ electric field strength are identical and overlap with each other and downshifted to the lower absorption for 0.2 kV mm⁻¹ field strength.

Table 4-1 summarises the surface tension components of solvents and 2D materials investigated in this study ¹³⁻¹⁵. Previously surface tension matching ¹⁵, or the matching of polar component/dispersive component ratio ^{13, 14, 16} have been identified as the possible parameters governing the efficiency of the exfoliation process with no electric field applied. However, it seems that here the best exfoliation outcomes are obtained when the dispersive component of the solvent, in the case of DMF (25.21), and WS₂ (25.59) are matched (Table 4-1). This makes sense as the dispersive interaction is defined as the interaction caused by temporary fluctuations of the charge distribution across the surface of the stratified particles and the nearby solvent ¹⁷. The matching of the dispersive component results in a resonance effect for the free charges near the interfacial area that influences the van der Waals interactions. The resonance increases the concentration of free charges at the interfacial layers of WS₂, which is a piezoelectric material. This in return enhances the surface agitation of the layers and increases the efficiency of exfoliation by weakening the van der Waals forces. This resonance is not seen for IPA/DI cosolvent as the dispersive components of none of the concentration matches that of WS₂ and these components are all lower for the IPA and DI cosolvent. The case of MoS₂/DMF is interesting as the application of the electric field causes a drop in the exfoliation efficiency, although MoS₂ has similarities of piezoelectric properties to WS₂. Considering that MoS₂ and DMF has a relatively close polar component/dispersive component ratios, 0.449 and 0.448, respectively, the change of electric field is in fact perturbs this matching and reduces the shear force impact (Table 4-1). The system is also tested on the exfoliation of graphene (Figure 4-6) and observed no effect of electric field on exfoliation efficiency as the interfacial graphene is a non-piezoelectric surface.

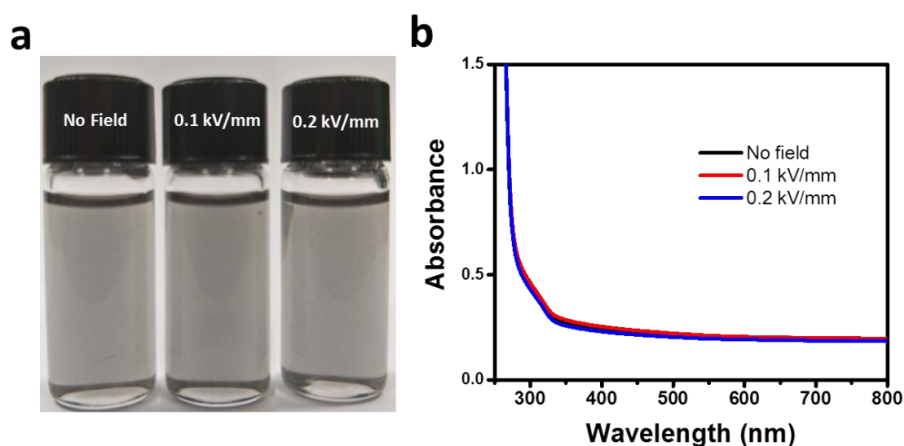


Figure 4-6 (a) Images of the suspensions of exfoliated graphene. (b) UV-vis spectra of graphene.

Overall, the synergy of the dispersive component between DMF and WS₂ along with the piezoelectric properties of WS₂, have a better effect on the efficiency of electric field-assisted exfoliation. Moreover, the closeness of the ratio of surface tension components between the aimed MoS₂ and DMF might reduce exfoliation efficiency. Such phenomenon does not apply to graphene due to its poorer piezoelectricity in comparison to WS₂ and MoS₂.

Table 4-1 Surface tension components of solvents and 2D materials.

Name	Surface tension [mN/m]	Dispersive component [mN/m]	Polar component [mN/m]	Polar component/dispersive component
IPA/DI (10/90)	43.90	21.11	22.79	1.080
IPA/DI (50/50)	25.13	16.96	8.17	0.482
IPA/DI (90/10)	22.77	15.79	6.98	0.442
DMF	36.5	25.21	11.29	0.448
WS ₂	40	25.59	14.41	0.563
MoS ₂	40	27.6	12.4	0.449
Graphene	63	42.83	20.17	0.471

AFM analysis was performed to assess the thickness of the WS₂ nanoflakes. Figure 4-1(b) shows the thickness profile of a typical WS₂ grain and AFM image as the inset. Distributions

of the nanoflake thicknesses for each condition are displayed in Figure 4-7 along with sample AFM images. It was observed that the electric field has an apparent impact on the thickness of the exfoliated WS₂. The thickness distribution of the WS₂ nanoflakes was reduced (Figure 4-7(a), (b), (c)) with the introduction and increase of the external electric field. The measured median thicknesses of exfoliated 2D WS₂ nanoflakes were approximately 4.4, 3.4 and 2 nm for no field, 0.1 kV mm⁻¹, and 0.2 kV mm⁻¹, respectively. AFM confirms that the 0.2 kV mm⁻¹ field sample constitute a large proportion of single and double-layer flakes in the dispersions

18.

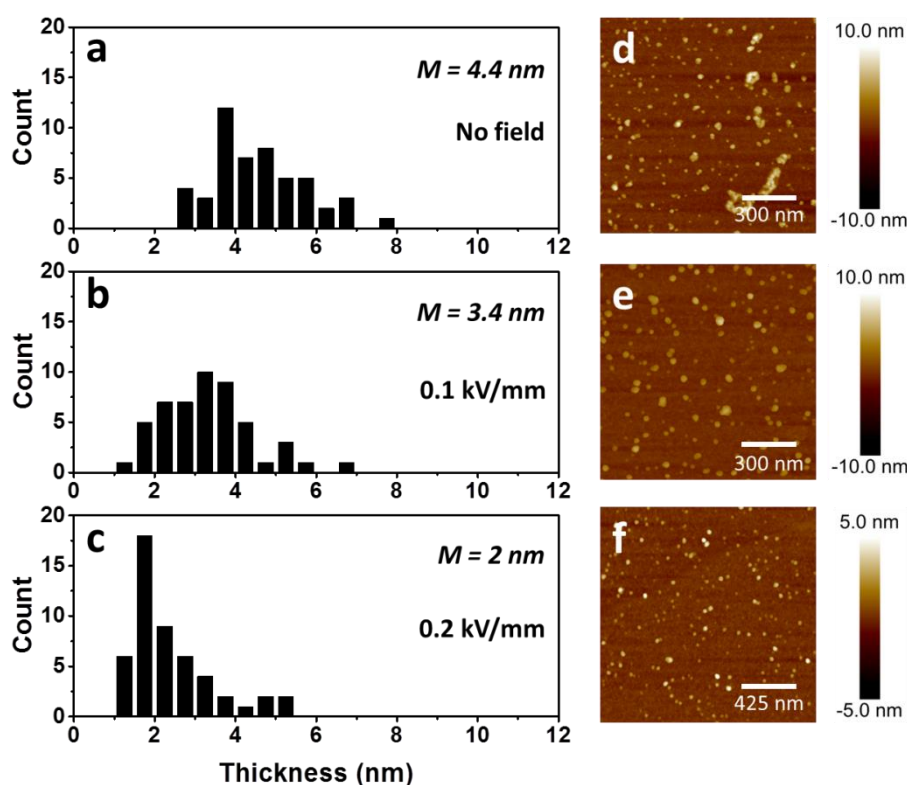


Figure 4-7 AFM characterisation of the exfoliated nanoflakes. AFM thickness distribution histogram of (a) no field (b) 0.1 kV mm⁻¹ and (c) 0.2 kV mm⁻¹ and correspondent original AFM images shown in (c), (d) & (f), respectively. 50 randomly selected nanoflakes of each sample were analysed by AFM to obtain thickness distribution histogram, and *M* represents median number of layers.

The lateral dimensions of the exfoliated WS₂ were assessed using TEM. Representative images of the nanoflakes obtained from the no field, 0.1 kV mm⁻¹ and 0.2 kV mm⁻¹ exfoliation

possesses are depicted in Figure 4-8(a, b), (c, d) and (e, f), respectively, along with their corresponding high-resolution TEM (HRTEM) images. The distribution of lateral dimensions of the nanoflakes from TEM images indicate that the nanoflakes were in the range of 40–80 nm across (Figure 4-9) and there is negligible change with an applied electric field. The estimated interlayer spacing from the HRTEM image was ~ 0.27 nm which matches well with the d-spacing value for the (100) plane of 2H-WS₂⁹. Altogether, the external electric field seems to impose no undesired effects on the morphology of the synthesised 2D WS₂ nanoflakes.

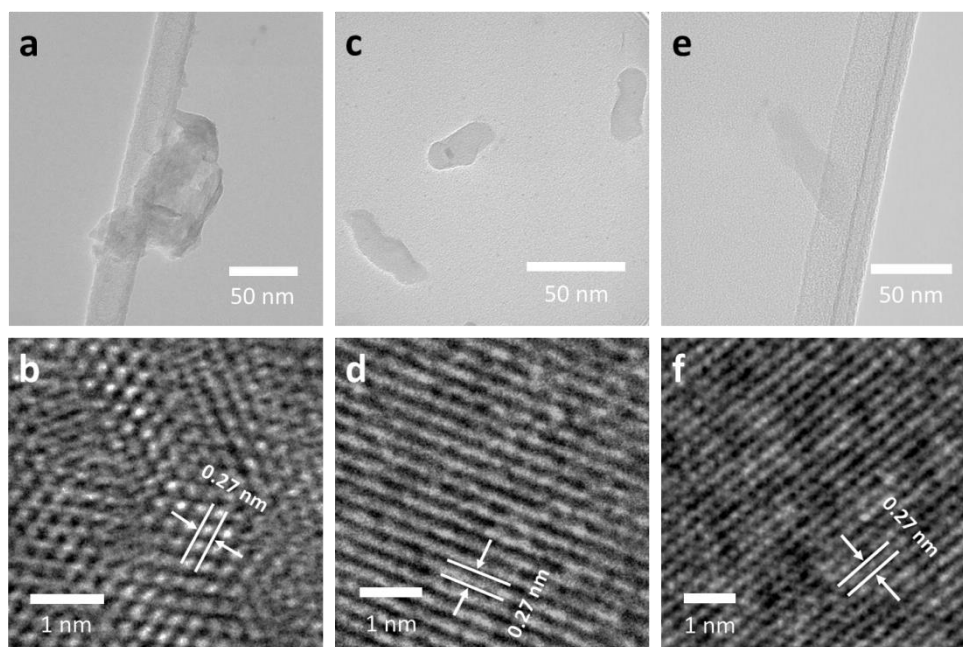


Figure 4-8 TEM and HRTEM with visible crystalline spacing images of typical (a, b) no field, (c, d) 0.1 kV mm⁻¹, and (e, f) 0.2 kV mm⁻¹ of 2D WS₂ nanoflakes, respectively.

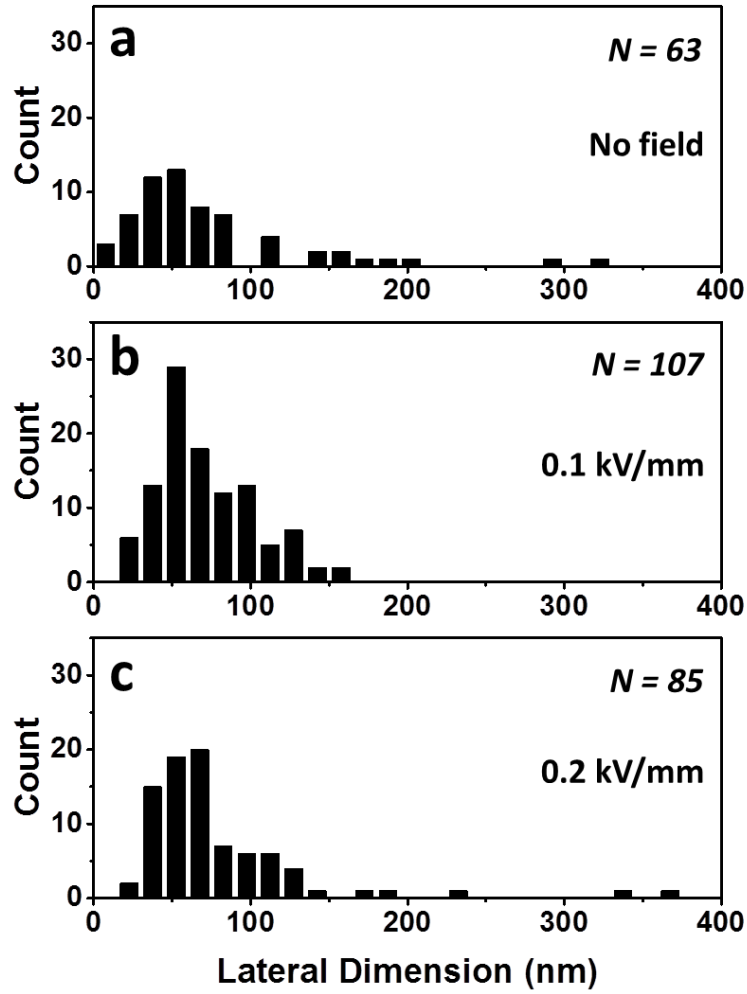


Figure 4-9 Lateral dimension distributions of 2D WS₂ nanoflakes determined from TEM images: (a) no field (b) 0.1 kV mm⁻¹ (c) 0.1 kV mm⁻¹. Here, N represents the number of nanoflakes for the construction of flakes distributions.

Raman spectroscopy is a non-destructive approach to assess the structural quality and vibration properties of the exfoliated WS₂ nanoflakes. For all conditions represented in Figure 4-10(a), the Raman spectra were dominated by the 2LA (M), E_{2g}¹ and A_{1g} modes which is consistent with previous reports^{19, 20}. At the excitation wavelengths of 488 and 647 nm, the intensity of 2LA (M) mode is weaker than that of the E_{2g}¹¹⁹; however, Raman spectra is shown in Figure 4-10(a) at 532 nm excitation wavelength, 2LA (M) mode is stronger than that of the E_{2g}¹²⁰. Such behaviour can be explained by the double resonance process due to the laser excitation wavelength dependency of the intensity of 2LA (M) and E_{2g}¹ phonon modes^{19, 20}. Wavenumber

differences between second-order Raman peak, the 2LA (M) and the out-of-plane vibrational mode A_{1g} of all samples were observed to be identical ($\sim 64 \text{ cm}^{-1}$). This can be attributed to the small thickness dependence of the A_{1g} and 2LA (M) peaks in WS_2 ^{19, 21-23} and $\sim 1 \text{ nm}$ difference in median thickness of nanoflake between samples. However, with the increase of the applied electric field, the intensity ratio of $A_{1g}/2\text{LA (M)}$ peaks decreases, which generally indicate the reduction of number of layers^{19, 21}. For no field, 0.1 kV mm^{-1} , and 0.2 kV mm^{-1} , the intensity ratio of $A_{1g}/2\text{LA (M)}$ is 0.94, 0.86, and 0.75, respectively, which is consistent with the reduction of nanoflakes thickness.

The indirect bandgap of 1.4 eV in bulk WS_2 changes to a direct bandgap of 2.1 eV when it is thinned down to monolayer²⁴. Therefore, strong PL emerges²⁴. The PL spectra of the WS_2 nanoflakes under the 532 nm excitation is presented in Figure 4-10(b). Here, the exciton A peak of monolayer WS_2 appeared at approximately 2.1 eV. A strong peak at approximately 1.85 eV originating from mono to multilayers nanoflakes of varying A exciton binding energies and edge/defect emission, is in good agreement with liquid-phase exfoliation results reported in the past²⁵. Moreover, the strengthening of PL signal with the increase of applied electric field indicates the thinning of WS_2 ²⁶. The A exciton peak position of WS_2 is weakly dependent on the flake thickness^{20, 21, 27}. In many previous reports, with the decrease of thickness, A exciton peak experiences a slight shift^{20, 21, 27, 28}. In contrast, no visible shift of A exciton peak was observed for the samples shown in Figure 4-10(b). Such discrepancy might be due to the different exfoliation processes, which have also been reported previously²⁹.

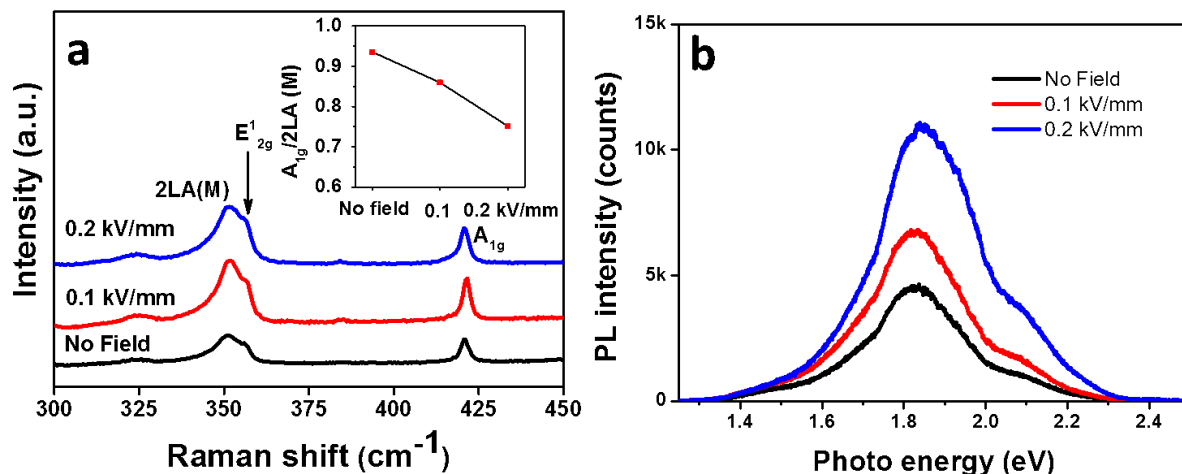


Figure 4-10 (a) Raman spectra of WS₂ nanoflakes exfoliated with phonon vibrational modes indicated. Inset depicts the peak intensity ratio between 2LA (M) and A_{1g} modes as a function of electric field. (b) PL signal of the samples prepared on gold-coated Si substrates. Peaks intensity increased with the introduction of electric field.

Furthermore, the effect of electric field on the chemical state and crystal structure of exfoliated WS₂ nanoflakes were assessed by XRD measurements. XRD patterns of bulk, with and without electric field exfoliated WS₂ are shown in Figure 4-11. Various peaks in bulk WS₂ arise from the lattice planes of stacked many layers. However, only four peaks exist in exfoliated WS₂ nanoflakes, and those peaks were from the symmetry of the vertical crystal planes at 14.32, 28.89, 43.93, and 59.87 corresponding to 002, 004, 006 and 008 lattice planes of 2H-WS₂, respectively¹². No change in peak positions between no field and applied electric field was observed.

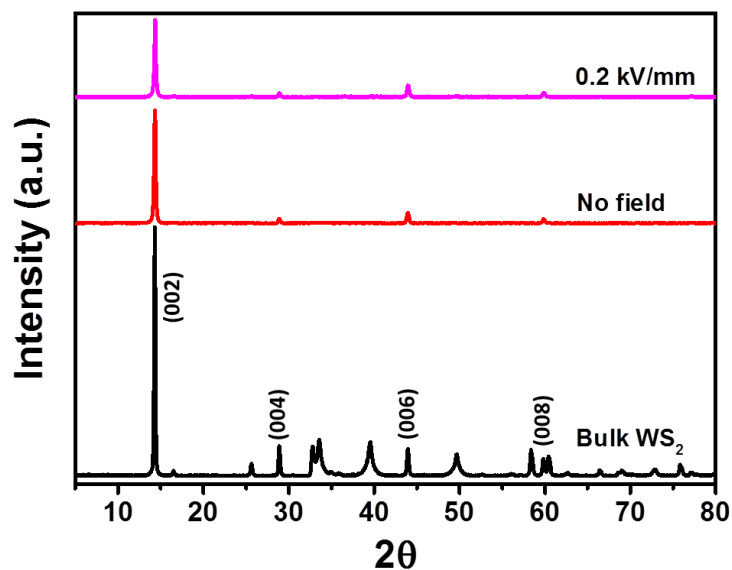


Figure 4-11 XRD patterns for bulk WS₂ and exfoliated 2D WS₂ nanoflakes.

The zeta potential of exfoliated dispersion indicates the magnitude of the electrostatic attraction/repulsion between nanoflakes to evaluate the stability of colloidal suspensions. Dispersions with higher absolute zeta potential are more electrostatically stable due to the relative high repulsive forces over the attractive forces³⁰. The value of zeta potentials were -13.4 , -20.9 , and -21.8 mV for no field, 0.1 kV mm^{-1} , and 0.2 kV mm^{-1} , respectively (Figure 4-12). Therefore, exfoliated WS₂ nanoflakes were negatively charged^{30, 31} and the increase in the absolute value of the exfoliated nanoflakes with the presence of electric field indicates better dispersion stability than sonication only exfoliation^{32, 33}. To determine the long term aqueous stability of exfoliated WS₂ nanoflakes, suspensions are re-examined using zeta potential after six months of storage at room temperature. The results (Figure 4-13) show that the polarity of suspensions hasn't changed; however, slight decrease of absolute zeta potential of 3.1 , 2.4 and 0.6 mV has been observed for no field, 0.1 kV mm^{-1} , and 0.2 kV mm^{-1} , respectively.

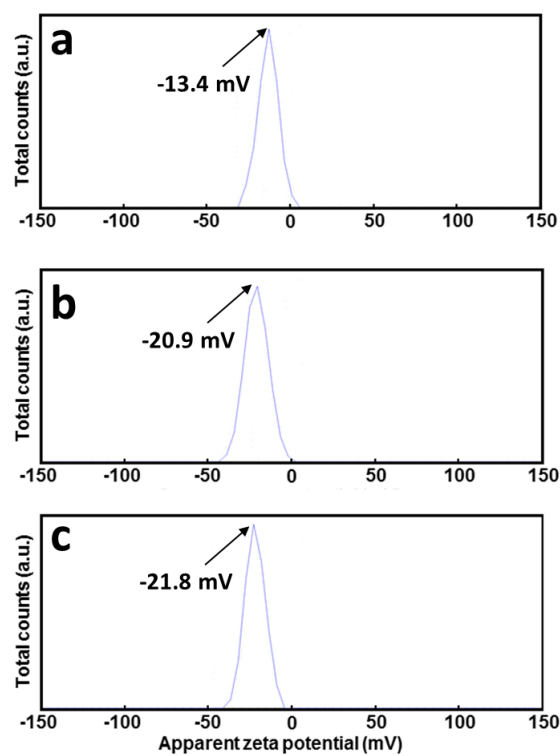


Figure 4-12 Zeta potential spectra for WS₂ nanoflakes for three samples: (a) no field (b) 0.1 kV mm⁻¹ (c) 0.2 kV mm⁻¹.

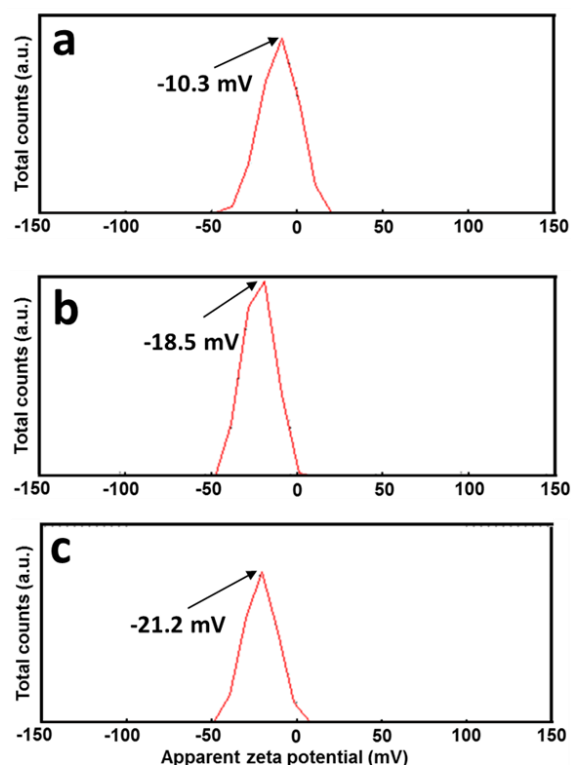


Figure 4-13 Zeta potential spectra for WS₂ nanoflakes for three samples: (a) no field (b) 0.1 kV mm⁻¹ (c) 0.2 kV mm⁻¹ after six months.

For the proof-of-concept, electrocatalytic HER performance of exfoliated WS₂ nanosheet, the electrochemical measurements of WS₂ with and without electric field exfoliation were conducted in acidic media (0.5 M H₂SO₄). For comparison, electrocatalysts and bare carbon paper electrodes were tested at room temperature under identical conditions. The linear sweep voltammetry (LSV) measurements are shown in Figure 4-14. The electric field exfoliated WS₂ nanosheets showed lower overpotential compared to sonication only exfoliated WS₂ to achieve 10 mA cm⁻² current density. As shown in Figure 4-14, for electric field exfoliated WS₂, an overpotential of 376 mV was required to achieve standard 10 mA cm⁻² current density, whereas it was 429 mV for no field exfoliation WS₂.

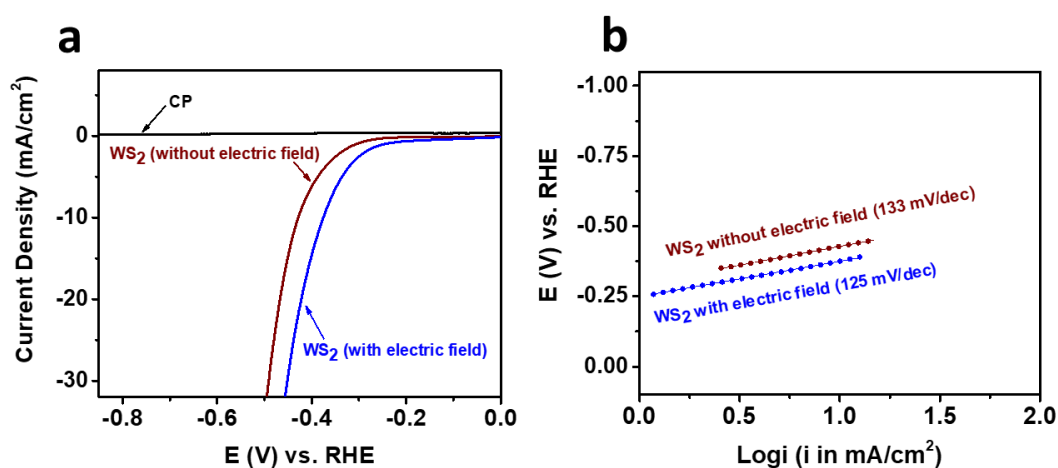


Figure 4-14 (a) LSV curves of bare CP, sonication only and electric field exfoliated WS₂ in 0.5 M H₂SO₄ and (b) the corresponding Tafel slopes.

To obtain further insight into the HER activity, the Tafel slopes were derived from the LSV polarisation curves, as shown in Figure 4-14b, the lower the values of Tafel slopes the faster the HER rates. A Tafel slope of 125 mV dec⁻¹ was observed for the field exfoliated 2D WS₂ nanosheets, which is smaller than the value obtained for sonication only WS₂ (133 mV dec⁻¹), indicates the superior HER activity of field exfoliated WS₂.

The electrochemically surface area (ECSA) of the electrocatalysts was calculated using electric double layer capacitance (EDLC) *via* CV (Figure 4-15) in order to understand the intrinsic

activity of the active sites and active sites play the most important role for hydrogen evolution reaction. For the calculation, the geometric current density at 0.15 V vs the RHE is plotted against five different CV scan rates as depicted in Figure 4-16. The EDLC values were calculated from the slopes of the linear regression of Figure 4-16. A larger EDLC value of 16.1 mF cm^{-2} was obtained for the 2D electric field exfoliated WS_2 compared to the value of 7.5 mF cm^{-2} measured for sonication only exfoliation. 2D electric field exfoliated WS_2 possesses much higher active surface area compared to sonication only exfoliated WS_2 , which led to excellent HER activity.

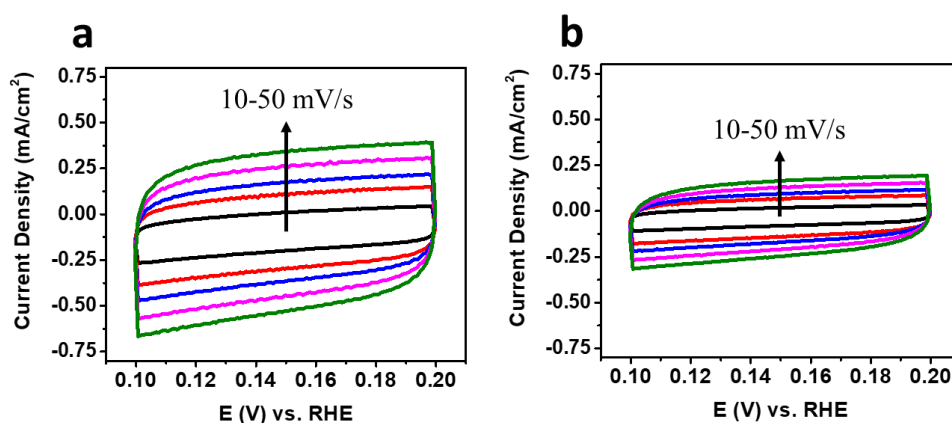


Figure 4-15 Cyclic voltammetry (CV) curves for (a) electric field-assisted exfoliated WS_2 , (b) sonication only exfoliated WS_2 in the region of 0.10 ~ 0.20 V vs RHE at five different scan rates.

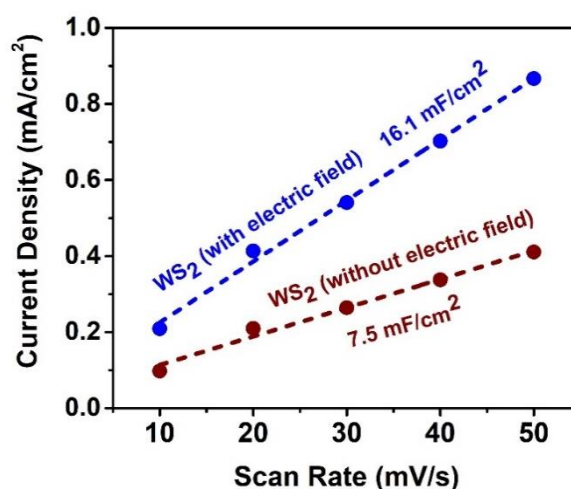


Figure 4-16 Capacitive currents at 0.15 V vs RHE as a function of scan rate for nanosheets electric field-assisted and sonication only exfoliated WS_2 .

4.4 Conclusions

In brief, the presence of an electric field plays an important role in the liquid-phase exfoliation of WS₂ and not MoS₂ and graphite. This was associated to the lack of symmetry on the interfacial planes of dispersive component of DMF and WS₂ are similar, while the polar and dispersive components ratio is very close for DMF and MoS₂ and piezoelectricity of the boundary layers are small for graphene. Investigations of exfoliated WS₂ confirm that the intrinsic characteristics of WS₂ were well preserved even after the exposure to electric field in liquid media. It has been shown that if the condition is well designed, a more efficient exfoliation process could be obtained with the increase of electric field. The developed method can be utilised simultaneously with sonication to improve the efficiency of selected liquid-phase exfoliation process, especially for those that the solution and stratified materials matching of dispersive component. Unlike micro-exfoliation, odd and even number of layers biasness has not been observed in this experiment. The difference could be due to the high electric field strength and frequency which was not possible to achieve using available amplifiers. Finally, the proof-of-concept electrochemical HER measurements show the superior performance of electric field-assisted exfoliated WS₂ nanosheets over sonication only exfoliation. To further improve the catalytic and charge transfer activities, WS₂ can be hybridised before the exfoliation process. The hybridisation of WS₂ could be carried out by adding centrosymmetric materials such as quantum dots, graphene. Carbon-based centrosymmetric materials will enhance charge transfer activities but will not be influenced by the external electric field.

References

1. Duerloo, K.-A. N., Ong, M. T., Reed, E. J., Intrinsic piezoelectricity in two-dimensional materials. *J. Phys. Chem. C* **2012**, 3 (19), 2871-2876.

2. Blonsky, M. N., Zhuang, H. L., Singh, A. K., Hennig, R. G., *Ab initio* prediction of piezoelectricity in two-dimensional materials. *ACS Nano* **2015**, 9 (10), 9885-9891.
3. Alyörük, M. M., Aierken, Y., Çakır, D., Peeters, F. M., Sevik, C., Promising piezoelectric performance of single layer transition-metal dichalcogenides and dioxides. *J. Phys. Chem. C* **2015**, 119 (40), 23231-23237.
4. Wu, W., Wang, L., Li, Y., Zhang, F., Lin, L., Niu, S., Chenet, D., Zhang, X., Hao, Y., Heinz, T. F., et al., Piezoelectricity of single-atomic-layer MoS₂ for energy conversion and piezotronics. *Nature* **2014**, 514, 470.
5. Zhu, H., Wang, Y., Xiao, J., Liu, M., Xiong, S., Wong, Z. J., Ye, Z., Ye, Y., Yin, X., Zhang, X., Observation of piezoelectricity in free-standing monolayer MoS₂. *Nat. Nanotechnol.* **2014**, 10, 151.
6. Michel, K. H., Verberck, B., Phonon dispersions and piezoelectricity in bulk and multilayers of hexagonal boron nitride. *Phys. Rev. B* **2011**, 83 (11), 115328.
7. Zhou, M., Zhang, Z., Huang, K., Shi, Z., Xie, R., Yang, W., Colloidal preparation and electrocatalytic hydrogen production of MoS₂ and WS₂ nanosheets with controllable lateral sizes and layer numbers. *Nanoscale* **2016**, 8 (33), 15262-15272.
8. Pagona, G., Bittencourt, C., Arenal, R., Tagmatarchis, N., Exfoliated semiconducting pure 2H-MoS₂ and 2H-WS₂ assisted by chlorosulfonic acid. *Chem. Commun.* **2015**, 51 (65), 12950-12953.
9. Atkin, P., Daeneke, T., Wang, Y., Carey, B. J., Berean, K. J., Clark, R. M., Ou, J. Z., Trinchì, A., Cole, I. S., Kalantar-zadeh, K., 2D WS₂/carbon dot hybrids with enhanced photocatalytic activity. *J. Mater. Chem. A* **2016**, 4 (35), 13563-13571.
10. Coleman, J. N., Lotya, M., O'Neill, A., Bergin, S. D., King, P. J., Khan, U., Young, K., Gaucher, A., De, S., Smith, R. J., et al., Two-dimensional nanosheets produced by liquid exfoliation of layered materials. *Science* **2011**, 331 (6017), 568-571.

11. O'Neill, A., Khan, U., Coleman, J. N., Preparation of high concentration dispersions of exfoliated MoS₂ with increased flake size. *Chem. Mater.* **2012**, *24* (12), 2414-2421.
12. Carey, B. J., Daeneke, T., Nguyen, E. P., Wang, Y., Zhen Ou, J., Zhuiykov, S., Kalantar-zadeh, K., Two solvent grinding sonication method for the synthesis of two-dimensional tungsten disulphide flakes. *ChemComm* **2015**, *51* (18), 3770-3773.
13. Shen, J., Wu, J., Wang, M., Dong, P., Xu, J., Li, X., Zhang, X., Yuan, J., Wang, X., Ye, M., et al., Surface tension components based selection of cosolvents for efficient liquid phase exfoliation of 2D materials. *Small* **2016**, *12* (20), 2741-2749.
14. Shen, J., He, Y., Wu, J., Gao, C., Keyshar, K., Zhang, X., Yang, Y., Ye, M., Vajtai, R., Lou, J., et al., Liquid phase exfoliation of two-dimensional materials by directly probing and matching surface tension components. *Nano Lett.* **2015**, *15* (8), 5449-5454.
15. Cunningham, G., Lotya, M., Cucinotta, C. S., Sanvito, S., Bergin, S. D., Menzel, R., Shaffer, M. S. P., Coleman, J. N., Solvent exfoliation of transition metal dichalcogenides: dispersibility of exfoliated nanosheets varies only weakly between compounds. *ACS Nano* **2012**, *6* (4), 3468-3480.
16. Wang, M., Xu, X., Ge, Y., Dong, P., Baines, R., Ajayan, P. M., Ye, M., Shen, J., Surface tension components ratio: an efficient parameter for direct liquid phase exfoliation. *ACS Appl. Mater. Interfaces* **2017**, *9* (10), 9168-9175.
17. Bargeman, D., van Voorst Vader, F., Van der waals forces between immersed particles. *J. Electroanal. Chem. Interfacial Electrochem.* **1972**, *37* (1), 45-52.
18. Yan, Y., Zhang, C., Gu, W., Ding, C., Li, X., Xian, Y., Facile synthesis of water-soluble WS₂ quantum dots for turn-on fluorescent measurement of lipoic acid. *J. Phys. Chem. C* **2016**, *120* (22), 12170-12177.
19. Berkdemir, A., Gutiérrez, H. R., Botello-Méndez, A. R., Perea-López, N., Elías, A. L., Chia, C.-I., Wang, B., Crespi, V. H., López-Urías, F., Charlier, J.-C., et al.,

- Identification of individual and few layers of WS₂ using Raman Spectroscopy. *Sci. Rep.* **2013**, 3, 1755.
20. Peimyoo, N., Shang, J., Yang, W., Wang, Y., Cong, C., Yu, T., Thermal conductivity determination of suspended mono- and bilayer WS₂ by Raman spectroscopy. *Nano Res.* **2015**, 8 (4), 1210-1221.
 21. Zeng, H., Liu, G.-B., Dai, J., Yan, Y., Zhu, B., He, R., Xie, L., Xu, S., Chen, X., Yao, W., et al., Optical signature of symmetry variations and spin-valley coupling in atomically thin tungsten dichalcogenides. *Sci. Rep.* **2013**, 3, 1608.
 22. Zhao, W., Ghorannevis, Z., Amara, K. K., Pang, J. R., Toh, M., Zhang, X., Kloc, C., Tan, P. H., Eda, G., Lattice dynamics in mono- and few-layer sheets of WS₂ and WSe₂. *Nanoscale* **2013**, 5 (20), 9677-9683.
 23. Zhang, Y., Zhang, Y., Ji, Q., Ju, J., Yuan, H., Shi, J., Gao, T., Ma, D., Liu, M., Chen, Y., et al., Controlled growth of high-quality monolayer WS₂ layers on sapphire and imaging its grain boundary. *ACS Nano* **2013**, 7 (10), 8963-8971.
 24. Wang, Q. H., Kalantar-Zadeh, K., Kis, A., Coleman, J. N., Strano, M. S., Electronics and optoelectronics of two-dimensional transition metal dichalcogenides. *Nat. Nanotechnol.* **2012**, 7, 699.
 25. Bernal, M. M., Lidia, Á., Emerson, G., Adriana, A., Luisa, R.-G., Santiago, C., Daniel, G., Ana, M. P., Andres, C.-G., Emilio, M. P., Luminescent transition metal dichalcogenide nanosheets through one-step liquid phase exfoliation. *2D Mater.* **2016**, 3 (3), 035014.
 26. Park, J., Lee, W., Choi, T., Hwang, S.-H., Myoung, J. M., Jung, J.-H., Kim, S.-H., Kim, H., Layer-modulated synthesis of uniform tungsten disulfide nanosheet using gas-phase precursors. *Nanoscale* **2015**, 7 (4), 1308-1313.

27. Zhao, W., Ghorannevis, Z., Chu, L., Toh, M., Kloc, C., Tan, P.-H., Eda, G., Evolution of electronic structure in atomically thin sheets of WS₂ and WSe₂. *ACS Nano* **2013**, 7 (1), 791-797.
28. Gutiérrez, H. R., Perea-López, N., Elías, A. L., Berkdemir, A., Wang, B., Lv, R., López-Urías, F., Crespi, V. H., Terrones, H., Terrones, M., Extraordinary room-temperature photoluminescence in triangular WS₂ monolayers. *Nano Lett.* **2013**, 13 (8), 3447-3454.
29. Peimyoo, N., Shang, J., Cong, C., Shen, X., Wu, X., Yeow, E. K. L., Yu, T., Nonblinking, intense two-dimensional light emitter: monolayer WS₂ triangles. *ACS Nano* **2013**, 7 (12), 10985-10994.
30. Bhandavat, R., David, L., Singh, G., Synthesis of surface-functionalized WS₂ nanosheets and performance as Li-Ion battery anodes. *J. Phys. Chem. Lett.* **2012**, 3 (11), 1523-1530.
31. Notley, S. M., High yield production of photoluminescent tungsten disulphide nanoparticles. *J. Colloid Interface Sci.* **2013**, 396, 160-164.
32. Varrla, E., Backes, C., Paton, K. R., Harvey, A., Gholamvand, Z., McCauley, J., Coleman, J. N., Large-scale production of size-controlled MoS₂ nanosheets by shear exfoliation. *Chem. Mater.* **2015**, 27 (3), 1129-1139.
33. Ronan, J. S., Mustafa, L., Jonathan, N. C., The importance of repulsive potential barriers for the dispersion of graphene using surfactants. *New J. Phys.* **2010**, 12 (12), 125008.

Chapter 5

Facile and scalable template-assisted synthesis of ultrathin hematite nanosheets and nanonets†

† The contents of this chapter is under review in Mohiuddin et al., Synthesis of Two-Dimensional Hematite and Iron Phosphide for Hydrogen Evolution, *Journal of Materials Chemistry A*, 2019.

5.1 Introduction

2D materials are of great interest for different field of research ranging from electronics to energy due to thickness-dependent unique properties^{1, 2}. Majority of the 2D nanostructures synthesis methods are only suitable for layered materials³⁻⁷ and restricted to produce fewer quantities, limits their applicability at industrial scale. Individual layers are bonded weakly by van der Waals forces in layered materials; therefore, 2D ultrathin nanostructures can be obtained straightforwardly from intrinsically layered materials through well-established methods; however such ultrathin structures are considerably complex to produce for naturally non-layered materials due to the intrinsic three-dimensional bulk crystals structures⁸.

Chemical synthesis of 2D materials in suitable solvents are favourable for high yield synthesis which is prerequisite for many applications, particularly, energy storage and conversions^{9, 10}. A long list of ultrathin non-layered 2D structures are favourable to synthesis using wet-chemical synthesis approaches; however, conventional wet-chemical synthesis methods are encountered with poor control over the morphology and lateral dimensions¹¹. Amongst, template-assisted synthesis is one of the most popular and widely used wet-chemical technique to prepare free standing non-oriented/oriented nanostructures^{8, 11-13}. Majority of the template synthesis methods of nanostructures usually includes hard templates, as well activation of those

templates by complex processes and chemicals;^{12, 14} therefore, a facile and easily removable template strategy for the controlled synthesis of 2D nanostructures is highly desirable.

Owing to the low cost, earth abundance, and high stability under harsh conditions, hematite (α -Fe₂O₃) is widely been used for various applications such as energy conversions, photocatalysts^{15, 16}. Great efforts have been made so far to synthesis ultrathin nanosheets of α -Fe₂O₃ using different methods, as such half-unit-cell thickness of α -Fe₂O₃ with the lateral size up to about 1 μ m synthesised using the hard template, subsequently hard template was removed using a chemical etching process. Liquid-phase synthesis using sonication for long hours is another way to obtain ultrathin α -Fe₂O₃ nanosheets. Unfortunately, complicated long processing along with the limited yield hinder the further investigation for practical applications. Moreover, the facile and scalable synthesis of 2D nanosheets and nanonets of non-layered iron oxides and its compounds with defined shape and size is a great challenge; therefore, a scalable synthesis of α -Fe₂O₃ can open up a limitless possibility for diverse applications.

In this chapter, a novel synthesis of non-layered 2D ultrathin μ m sized α -Fe₂O₃ nanosheets and nanonets by utilising template is presented. The developed synthesis approach is highly scalable; moreover, the inexpensive and reusable template supports the nanostructures throughout the synthesis process. It is also hypothesised that the formation of ultrathin nanosheets on the surface of the crystalline template facilitates through the lattice matching between the template and target materials, interestingly, through the aging process at room temperature, nanosheets can be transformed to nanonets exploiting template induced strain effect.

5.2 Experimental section

5.2.1 Materials

Iron (III) nitrate nonahydrate, $\text{Fe}(\text{NO}_3)_3 \cdot 9\text{H}_2\text{O}$ (Chem-Supply), Sodium chloride, NaCl ($\geq 99\%$, Sigma-Aldrich), Sulfuric acid, H_2SO_4 ($\geq 99\%$, Sigma-Aldrich), Polytetrafluoroethylene, PTFE (60 wt%, Sigma-Aldrich), carbon paper, All chemicals were used without further purification.

5.2.2 Preparation of nanosheets and nanonets

1 g of $\text{Fe}(\text{NO}_3)_3 \cdot 9\text{H}_2\text{O}$ was dispersed in 20 ml of ethanol with stirring using magnetic stirrer for 30 min to obtain the precursor solution (Figure 5-1a). 310 g of NaCl salt (template) was measured and transferred in a 1L glass beaker for mixing. Previously prepared precursor solution mixed with the NaCl salt drop-wise and mixed manually on a hotplate at $\sim 80^\circ\text{C}$ for ~ 20 min. After the mixing process, precursor@template processed within 2-3 days (annealing, filtration etc) to obtain nanosheets on the template. For the growth process of nanonets, after the mixing of NaCl salt and precursor, precursor@template stored and left in ambient conditions until the light yellow mixture turns to light brown (takes ~ 10 days, Figure 5-1b).

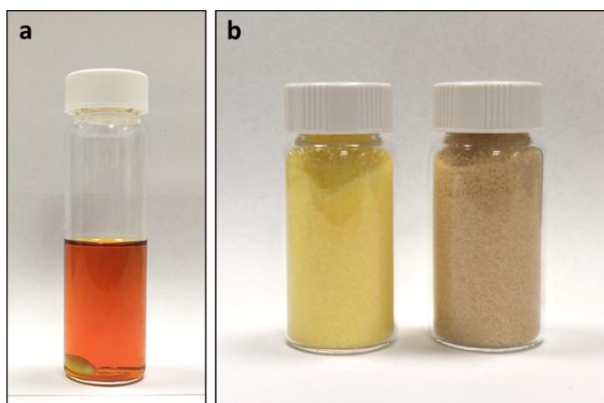


Figure 5-1 (a) Iron precursor (b) precursor and template mixture (left-immediately after preparation, right – after aging).

For the annealing process to obtain $\alpha\text{-Fe}_2\text{O}_3$, precursor@template mixture was dried in a tube furnace under Ar environment at 400°C for 2 h. Ramp rate for the annealing process was 2°C min^{-1} for nanosheets and $10^\circ\text{C min}^{-1}$ for nanonets. Nanosheet and nanonets (FeOOH , $\alpha\text{-Fe}_2\text{O}_3$)

Fe₂O₃)@template were washed with DI water to remove the template and redispersed in ethanol to obtain nanostructures for further characterisation.

5.2.3 Characterisations

TEM and HRTEM studies were performed on a JEOL 1010 and JEOL 2100F instruments, respectively operating at 100 and 200 kV, respectively. XPS was performed using a Thermo Scientific K-Alpha XPS spectrometer, and all the XPS results are calibrated at C-C (C 1s - 284.8 eV) to be used as a reference. The machine was featured with a monochromated Al K α X-ray source with a photon energy of 1486.7 eV and an X-ray spot size of 400 μ m. The samples were scanned with a pass energy of 50 eV and a dwell time of 50 ms. Data acquisition and processing were performed using Avantage software. XRD analysis was used to evaluate the crystal structure of samples which was performed using a Bruker D4 Endeavour featuring a CuK α X-ray source ($\lambda = 1.54 \text{ \AA}$). For both cases, the operating voltage and current were at 40 kV and 40 mA, respectively. The morphologies of the samples were observed with field emission SEM (FEI Verios 460L). For SEM, liquid suspension of samples drop-casted onto a pre-cleaned Si piece and dried in ambient, as prepared sample then mounted on aluminium stubs using both side adhesive carbon tape. AFM images were recorded using a Bruker Dimension Icon AFM with nanoscope software. For the AFM measurements, the samples were drop-casted on Si substrate which was pre-cleaned with acetone, IPA and DI water. The Fourier-transform infrared spectroscopy (FTIR) spectrum was performed on a PerkinElmer Spectrum 100 FT-IR spectrometer in a scan range of 4000 - 600 cm^{-1} .

5.2.4 Electrochemical measurements

Hydrogen evolution reaction was performed using a three-electrode configuration (CHI 760D) in 70 ml 0.5 M H₂SO₄ (pH = 0.3) electrolyte. Carbon paper coated with the samples was used as a working electrode whereas a graphite rod, and Ag/AgCl (in 1 M KCl aqueous solution) were used as a counter electrode, and reference electrode, respectively. The carbon paper was

cleaned using ethanol and DI water prior coating carbon paper with samples. All the potentials shown in this paper were converted to RHE and all the polarisation curves were iR corrected. The presented current density was normalised to the geometric surface area. Linear sweep voltammetry was performed at a 5 mV s^{-1} scan rate to obtain the polarisation curves. All the tests were conducted at room temperature and ambient pressure. Inks (FeOOH , $\alpha\text{-Fe}_2\text{O}_3$) were prepared by mixing 5 mg of materials powder and carbon black at 80% and 20% ratio in IPA and DI water mixture (1:1). 15 μL PTFE solution (60% in H_2O , Sigma) was added followed by sonication for 10 min. Around 100 μL of the suspension was drop-casted onto a carbon paper (CP) with an area of 0.25 cm^2 .

5.3 Results and discussion

A water dissolvable template-synthesis approach was employed to grow the atomically-thin nanosheets of iron compounds on the surface of crystalline sodium chloride (NaCl), as shown in Figure 5-2.

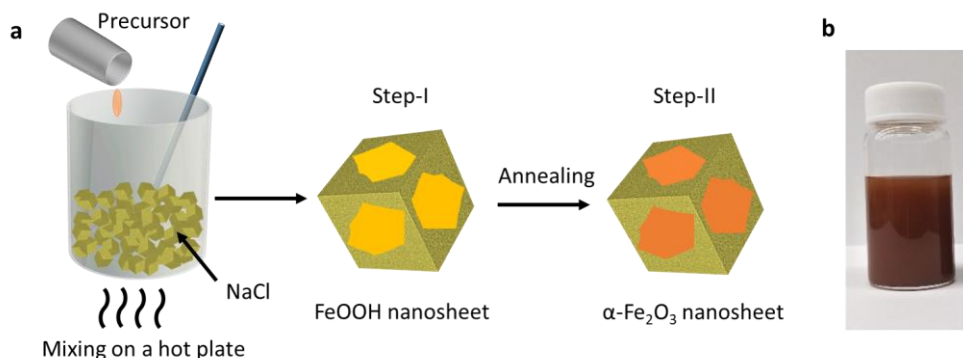


Figure 5-2 (a) Schematic of the synthesis procedure of nanosheets, step I, FeOOH nanosheets were obtained by filtering the initially formed FeOOH on the template (FeOOH@template), step II, shows the annealing of FeOOH@template to form $\alpha\text{-Fe}_2\text{O}_3$. (b) The optical image shows the liquid suspension of $\alpha\text{-Fe}_2\text{O}_3$.

The crystalline template plays the main key to facilitate the growth of the nanosheets from the precursor molecules on the template surface. The close match of lattice parameters between

the template and target material leads to the formation of nanosheets at the interface. The details of the lattice matching of coincidence lattices between NaCl template and preliminary formed ferric oxyhydroxide (FeOOH) will be presented later this section. After the formation of FeOOH on the template, annealing was carried out to form the stable nanosheets of α -Fe₂O₃. The TEM image in Figure 5-3a clearly reveals the ultrathin nature of the FeOOH nanosheets. The copious amount of several micrometres (~5 μ m) lateral sized FeOOH nanosheets are observed in SEM (Figure 5-3b), witness the scalability of the developed method. The selective area electron diffraction (SAED) pattern of FeOOH presented in the inset of Figure 5-3b indicates a match for the monoclinic phase (β -phase) of FeOOH (PDF 34-1266). The typical topography scan using AFM demonstrates the ultrathin features with thickness of 1.5 nm, as shown in Figure 5-3c, and d. Low magnification TEM image (Figure 5-4a) shows a typical morphology of the α -Fe₂O₃ nanosheet. The high resolution (HR) TEM image presented in Figure 5-4b delineates the lattice spacing of 2.5 Å corresponds to the (110) plane of α -Fe₂O₃ according to the standard card No JCPDS No. 24-0072¹⁷. The SAED image further witnesses the HRTEM observation by indexing (110) and (214) crystal plane of α -Fe₂O₃ (Figure 5-4c). AFM study of α -Fe₂O₃ nanosheet demonstrated in Figure 5-4d, and e shows the thickness down to 1 nm measured on Si substrate. Scanning TEM (STEM) energy dispersive spectroscopic (EDS) mapping and spectrum of α -Fe₂O₃ (Figure 5-5) confirm the uniformity of oxide formation and the presence of peaks for Fe and O atoms apart from Cu and C of TEM grid, indicate the absence of Na or Cl impurities from the template.

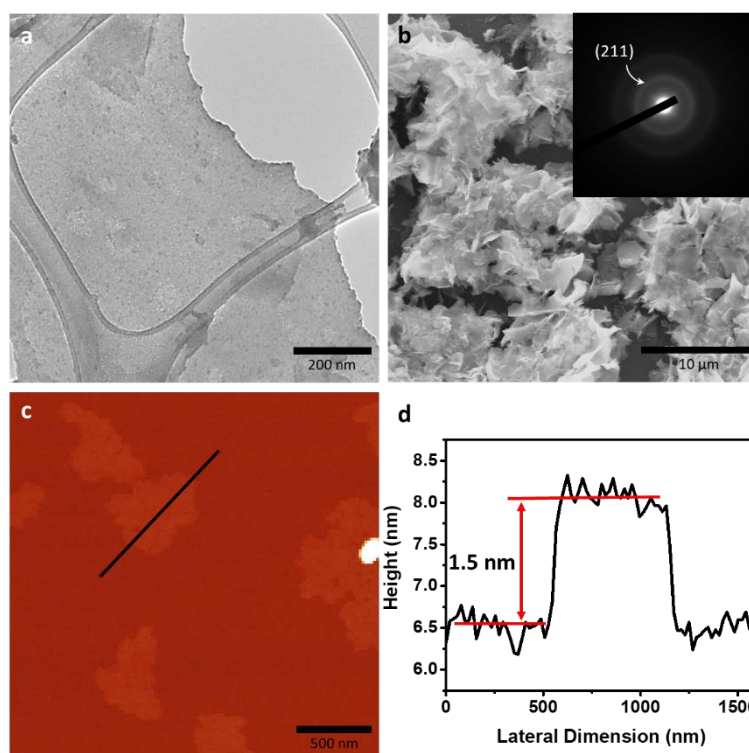


Figure 5-3 (a, b) low- resolution TEM and SEM images of FeOOH nanosheets, respectively. The inset of b shows the SAED of FeOOH nanosheets. (c) AFM image of the FeOOH nanosheets with corresponding (d) thickness profile.

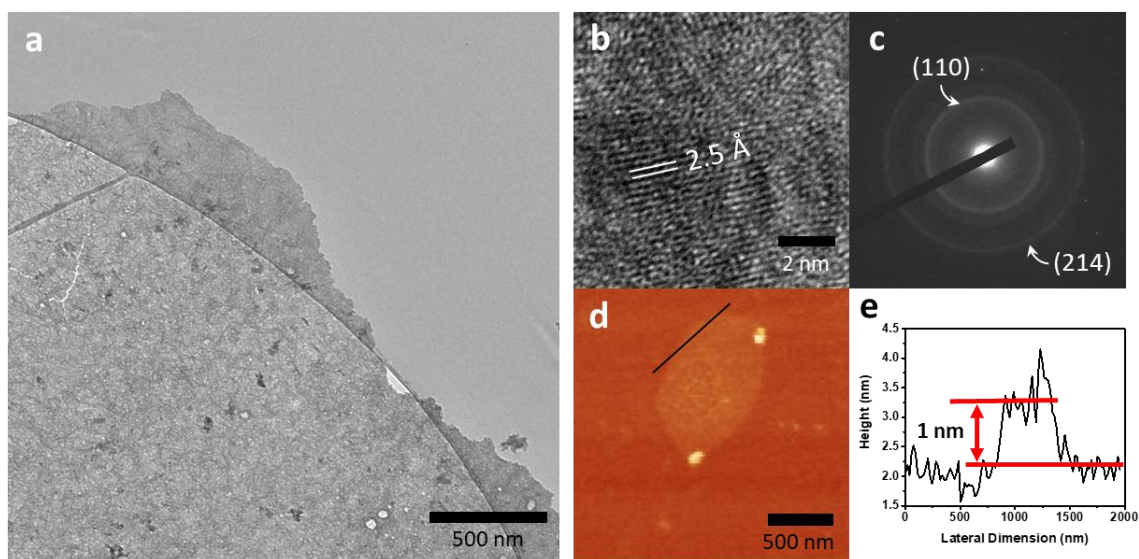


Figure 5-4 (a-c) low-, high-resolution TEM images, and SAED pattern of α -Fe₂O₃ nanosheets, respectively. (d) AFM images of α -Fe₂O₃ nanosheets with corresponding (e) thickness profile.

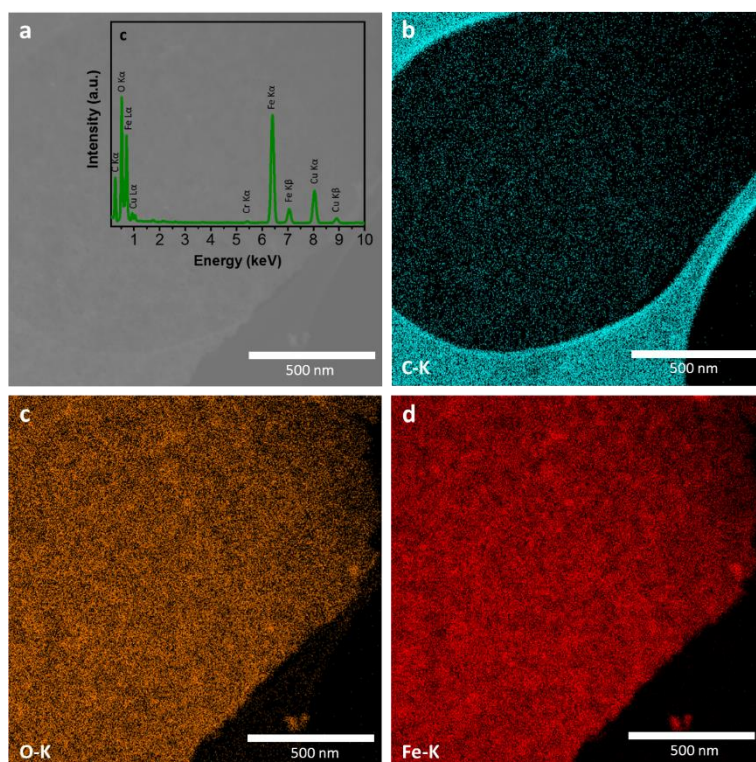


Figure 5-5 (a) STEM image along with (b-d) C, Fe and O elemental mapping of α -Fe₂O₃ nanosheets, respectively. STEM EDS spectrum of α -Fe₂O₃ nanosheets shown in the inset of a.

The high-resolution XPS Fe 2p spectrum of FeOOH and α -Fe₂O₃ nanosheets are shown in Figure 5-6a. Fe 2p peaks of FeOOH and α -Fe₂O₃ samples are identical and represent oxidation peaks. Doublet of Fe 2p_{3/2} and 2p_{1/2} are located at ~710.9 and ~724.5 eV, respectively, well separated by two board satellite peaks located at ~719.2 and ~733.4 eV, suggesting the Fe³⁺ oxidation state of iron in FeOOH and α -Fe₂O₃ nanosheets¹⁸.

Figure 5-6b and c, show the O 1s core-level spectrum of FeOOH and α -Fe₂O₃ nanosheets. For both, a peak exhibits at ~529.9 eV corresponding to lattice oxygen in iron oxyhydroxides or iron oxides¹⁹. On the other hand, the peak at ~531.5 eV corresponds to lattice hydroxyl group¹⁹. As expected, FeOOH nanosheets have more hydroxyl groups bound to their surface than α -Fe₂O₃. One additional distinct peak is observed for FeOOH nanosheets at ~533.5 eV, which belongs to the binding energy of surface absorbed H₂O molecules²⁰⁻²². The crystal structure and phase purity of FeOOH and α -Fe₂O₃ samples are investigated by XRD, as shown in Figure

5-6d. Upon annealing yellowish colour of FeOOH nanosheets turns to red. The XRD pattern of the FeOOH nanosheets exhibits two broad and weak diffraction peaks corresponding to the (310) and (211) orientation plane of β -FeOOH (PDF 34-1266). The XRD pattern of α -Fe₂O₃ shows the conversion to pure hematite (indexed as hexagonal α -Fe₂O₃, JCPDS No. 24-0072).

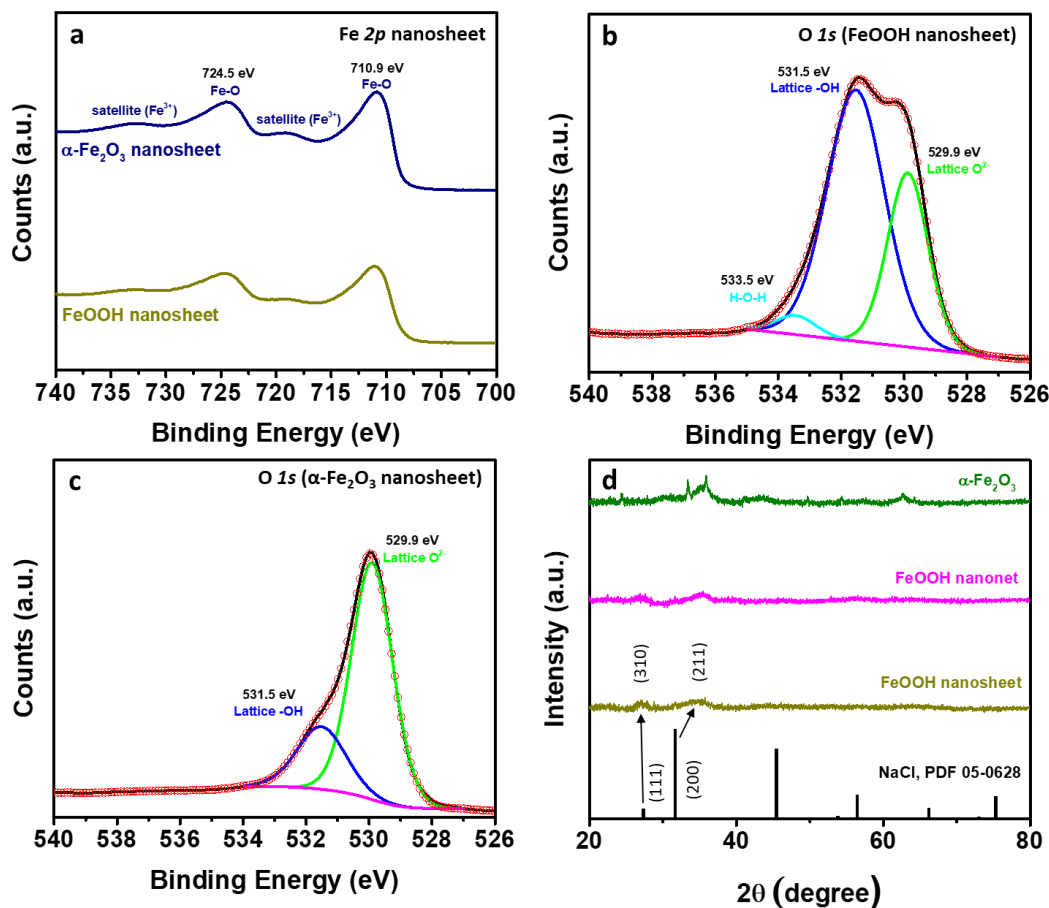


Figure 5-6 Structure and surface characterisations. XPS spectrum of nanosheets (a) Fe 2p (b) O 1s of FeOOH (c) O 1s of α -Fe₂O₃ (d) XRD pattern of FeOOH, α -Fe₂O₃.

As the phase is critical in forming FeOOH on the surface of the NaCl template, the (FTIR) is performed to further confirm the phase of FeOOH. The FTIR spectrum of FeOOH shown in Figure 5-7 also matches with the FTIR spectrum of β -FeOOH^{23, 24}. The bands observed at the region I and II attributed to the stretching and bending vibration mode of –OH bond, respectively resulting from surface absorbed water^{25, 26}, whereas bands at region III was ascribed to the vibration modes of Fe–O in β -FeOOH²⁷.

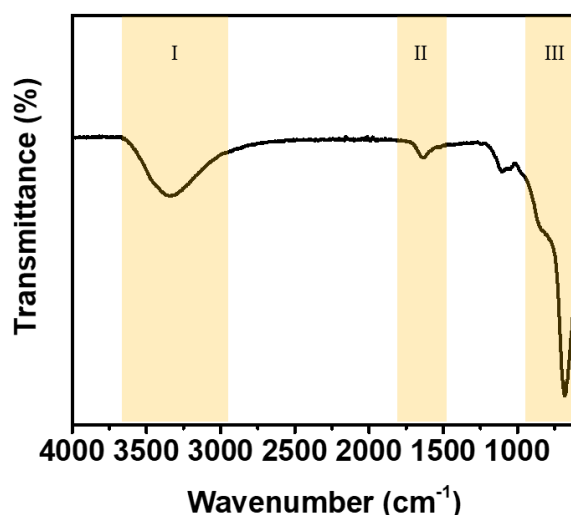


Figure 5-7 FTIR spectrum of FeOOH, which matches with the of β phase of FeOOH.

The mechanism of FeOOH nanosheets formation is driven by the close lattice matching between the NaCl template and the growing molecules. The low interfacial energy resulting from the close lattice matching initially favours the growth of ultrathin 2D β -FeOOH on NaCl template²⁸. However, lattice strain caused by the small amount lattice mismatch between the template and target materials can enable anisotropic shape transformation^{29,30}. Therefore, apart from the growth of nanosheets on crystalline template through close lattice matching, nanonets can also be grown on the template by aging the precursor@template mixture. The aging process allows anisotropic growth of nanonets on the template at room temperature for a period of time. Initially ultrathin layers form on the crystal surface; however, over time growth continues to nanonets through the aggregation of molecules from the strain of small lattice mismatch to stimulate the anisotropic growth²⁹. The XRD peak (310) of FeOOH nanostructures indicate close match with (111) of NaCl template favourable for nanosheets formation (Figure 5-6d). Contrary, small mismatch of (211) peak of FeOOH nanostructures with the (200) peak of NaCl template leads to the growth of anisotropic FeOOH nanonets.

To validate the hypothesis further, the time-dependent evolution of nanostructures formed on the template are examined at different times within the aging period to understand the shape

transformation process. Schematic illustrations and the TEM images below the schematic shown in Figure 5-8a-d demonstrate the evolution of nanonet. Initially, continuous nanosheet (Figure 5-8a) forms on the template and some voids start to form over time, as shown in Figure 5-8b. Subsequently, the amount of the voids on the nanosheets start to increase (Figure 5-8c) and eventually, the nanosheet is fully evolved to nanonets (Figure 5-8d). The detail characterisation of nanonets formed by aging process is represented in the subsequent section.

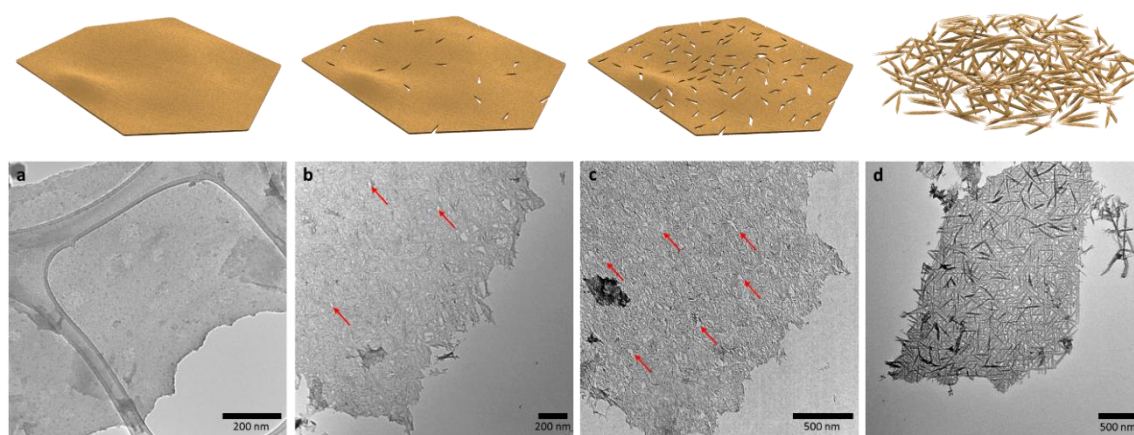


Figure 5-8 Schematic illustrations and TEM images of the time-dependent evolution of nanonet from nanosheet. (a) original nanosheet formed at the initial stage (b) over time voids start to form (indicated in red arrows) on the nanosheet (c) amount of void space increased with time (indicated in red arrows) leading to the formation of nanonet (d) nanonet from nanosheet completely evolved to nanonet.

Low magnification TEM and SEM of FeOOH nanonets shown in Figure 5-9a and b, respectively. As shown in TEM, the typical lengths and the widths of nanorod, which forms the nanonet are varies between 100 - 600 nm and 10 - 30 nm, respectively. The low magnification SEM image shows that the typical lateral dimension of nanonets is up to several μm . A close SEM observation (the inset of Figure 5-9b) of nanonet reveals the randomly orientated overlapping nanorods like structure. The diffused concentric rings of SAED pattern indicate the poor crystalline nature of FeOOH nanonet (Figure 5-9c). SEM of FeOOH nanonet is consistent with TEM image. Represented in Figure 5-9d, a typical AFM image of FeOOH nanonet along with the thickness profile indicate a typical thickness of 15 nm.

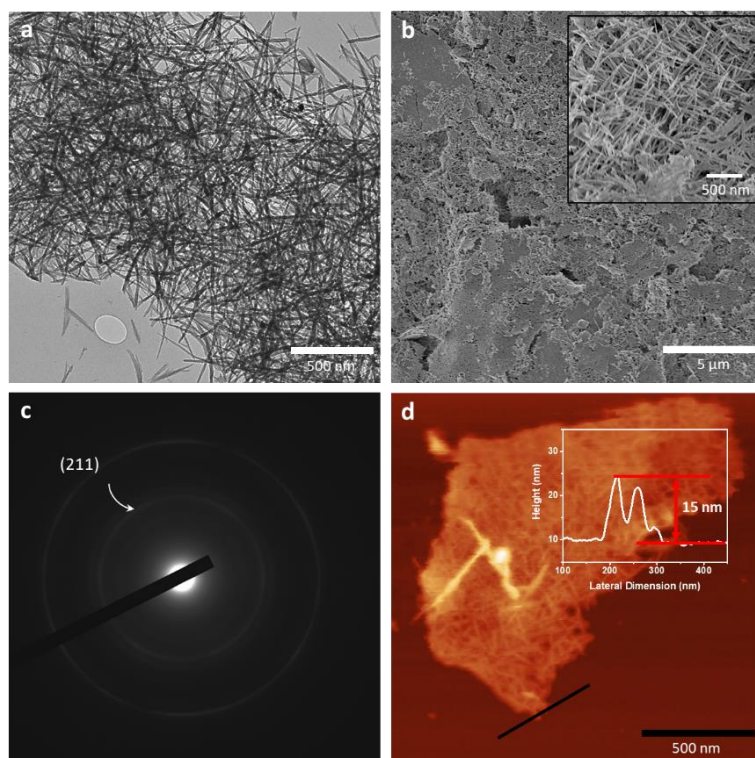


Figure 5-9 (a, b) low- resolution TEM and SEM images of FeOOH nanonet, respectively. The inset of b shows the zoom view of FeOOH nanonets. (c) SAED of FeOOH nanonet. (d) AFM image of the FeOOH nanonet with corresponding thickness profile shown in the inset of d.

The smooth surface of nanorods of FeOOH nanonets became slightly rough, might be due to the dehydration in annealing process (Figure 5-10a). The lattice fringe (Figure 5-10b) of polycrystalline α -Fe₂O₃ shows d-spacing of 2.5 Å, which is corresponding to the (110) crystal plane. The polycrystalline structure of α -Fe₂O₃ confirmed by SAED pattern shown in Figure 5-10c and diffraction spots can be indexed to (110) and (214) crystal planes of α -Fe₂O₃ nanonet. Typical AFM images and thickness profile in Figure 5-4d and e, respectively present the nominal thickness of nanonet to be ~5 nm. Similar to α -Fe₂O₃ nanosheet, the EDS elemental mapping and spectrum of α -Fe₂O₃ nanonet on a holey carbon copper TEM grid shows the Fe, O, Cu and C elements (Figure 5-11).

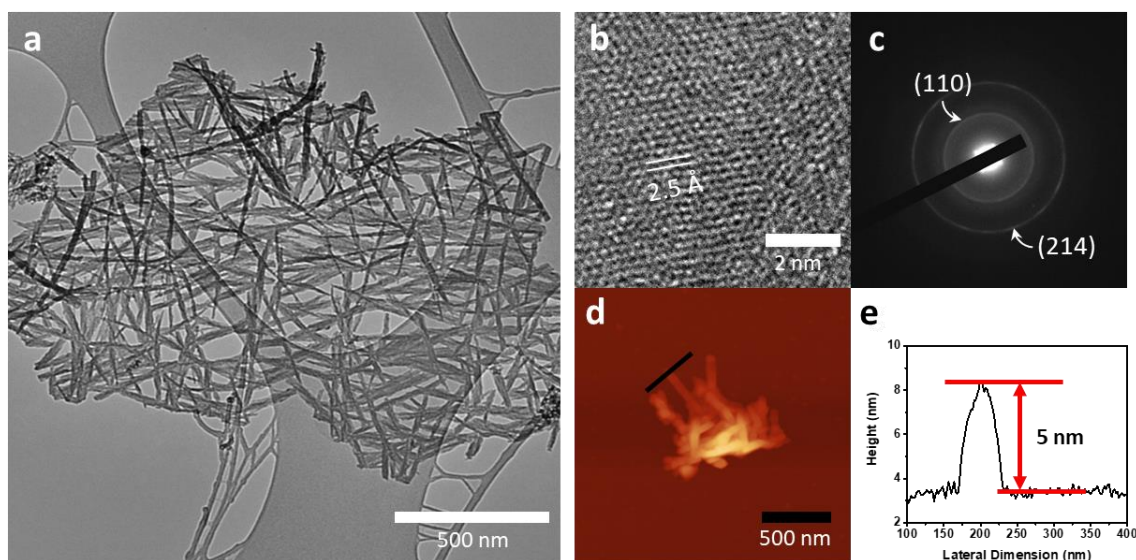


Figure 5-10 (a-c) low-, high-resolution TEM images, and SAED pattern of α -Fe₂O₃ nanonets, respectively. (d) AFM images of α -Fe₂O₃ nanonet with corresponding (e) thickness profile.

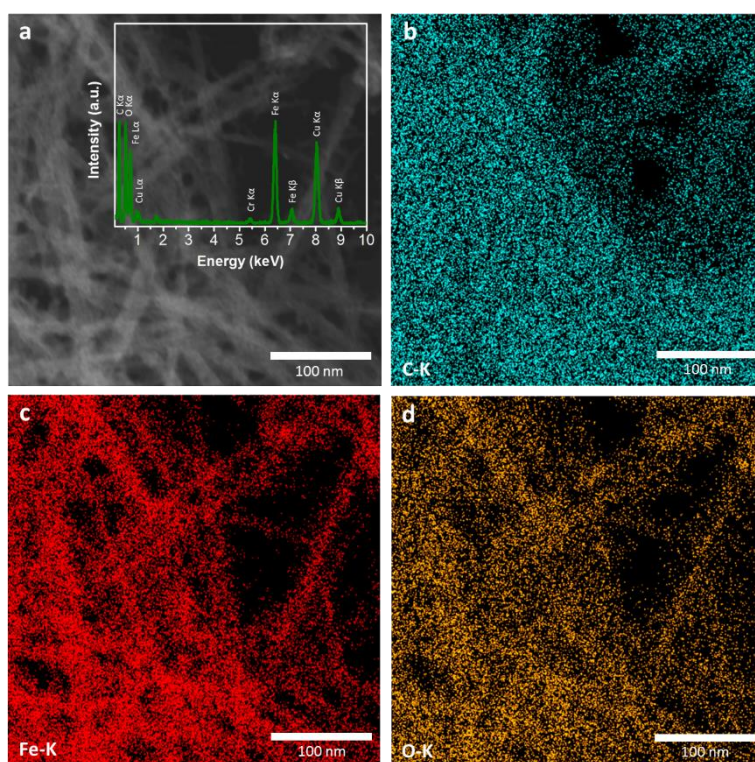


Figure 5-11 (a) STEM image along with (b-d) C, Fe and O elemental mapping of α -Fe₂O₃ nanonet, respectively. STEM EDS spectrum of α -Fe₂O₃ nanonet shown in the inset of a.

To examine the chemical composition due to the morphological transformation of nanonets, XPS of FeOOH and α -Fe₂O₃ nanonets are also performed which is represented in Figure 5-12.

The peak features are virtually the same for both the nanosheets and nanonets; therefore, aging process responsible for the morphological transformation only.

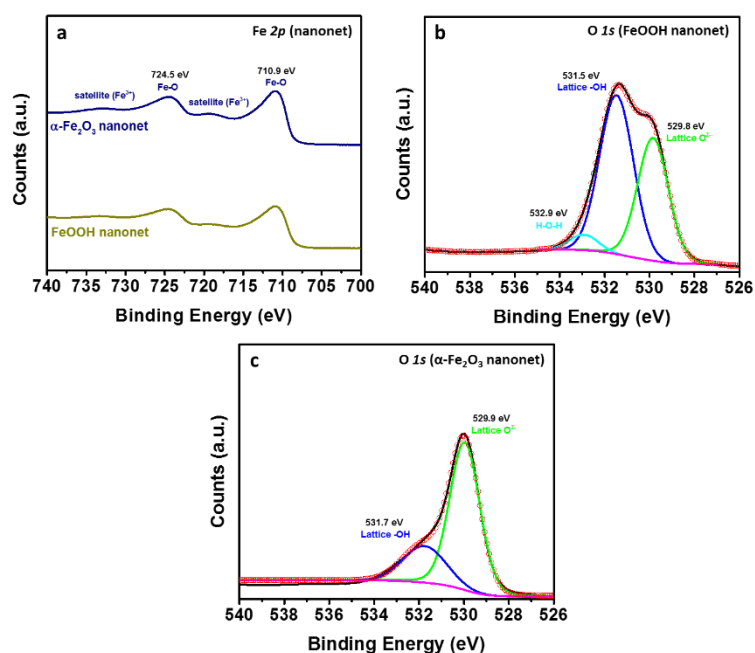


Figure 5-12 XPS spectrum of nanonets (a) Fe 2p (b) O 1s of FeOOH (c) O 1s of α -Fe₂O₃.

Nanosheets and nanonets of FeOOH and α -Fe₂O₃ have been examined for electrocatalytic HER performance. The electrocatalytic activity of the nanosheets and nanonets is evaluated by electrochemical measurements. The polarisation curves of nanosheets and nanonets loaded on carbon paper (1.6 mg cm⁻²) in acidic 0.5 M H₂SO₄ solution shown in Figure 5-13a. The current density of carbon paper, FeOOH nanosheets and FeOOH nanonets is negligible while α -Fe₂O₃ nanosheets and nanonets exhibit more than 800 mV overpotential to achieve 10 mA cm⁻² current density. However, the maximum current density achieved by α -Fe₂O₃ nanonets is higher than nanosheets. To extend the performance examination of the reaction kinetics, the corresponding Tafel plots of α -Fe₂O₃ based on the polarisation curves are presented in Figure 5-13b. A large Tafel slope of 203 and 171 mV dec⁻¹ for α -Fe₂O₃ nanosheets and nanonets, respectively is obtained.

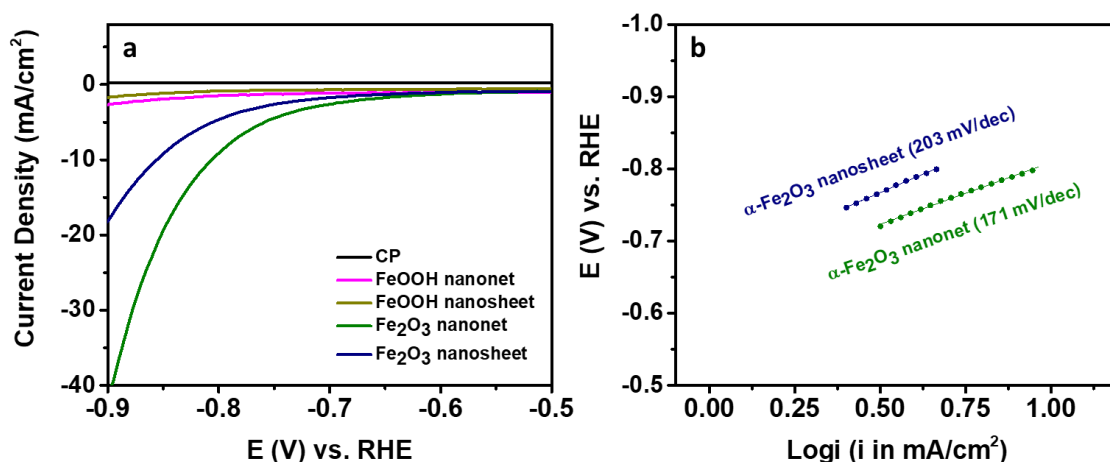


Figure 5-13 (a) Polarisation curves of FeOOH and α -Fe₂O₃ nanostructures measured in acidic media, (b) and the corresponding Tafel slopes of α -Fe₂O₃ nanostructures.

5.4 Conclusions

In summary, the synthesis of non-layered 2D α -Fe₂O₃ *via* template approach has been demonstrated. The close lattice matching allows the formation of ultrathin nanosheets on the template; however, shape transformation to the anisotropic nanonets resulting from the small lattice mismatch induced strain can also be introduced by aging process. Parameters such as precursor concentration, the ratio of precursor to template, growth temperature can be investigated further to tune the thickness and pore size of α -Fe₂O₃. Altogether, the template synthesis enables the facile and scalable process for synthesising low dimensional non-layered iron compounds which could open the new opportunities for the various applications. To overcome the high overpotential limitations of FeOOH and α -Fe₂O₃ nanostructures for the hydrogen production, attempts of conversion to FeP have been made, which is presented in the following chapter.

References

1. Fiori, G., Bonaccorso, F., Iannaccone, G., Palacios, T., Neumaier, D., Seabaugh, A., Banerjee, S. K., Colombo, L., Electronics based on two-dimensional materials. *Nat. Nanotechnol.* **2014**, *9*, 768.
2. Jin, H., Guo, C., Liu, X., Liu, J., Vasileff, A., Jiao, Y., Zheng, Y., Qiao, S.-Z., Emerging two-dimensional nanomaterials for electrocatalysis. *Chem. Rev.* **2018**, *118* (13), 6337-6408.
3. Li, X., Cai, W., An, J., Kim, S., Nah, J., Yang, D., Piner, R., Velamakanni, A., Jung, I., Tutuc, E., et al., Large-area synthesis of high-quality and uniform graphene films on copper foils. *Science* **2009**, *324* (5932), 1312-1314.
4. Yoo, D., Kim, M., Jeong, S., Han, J., Cheon, J., Chemical synthetic strategy for single-layer transition-metal chalcogenides. *J. Am. Chem. Soc.* **2014**, *136* (42), 14670-14673.
5. Zavabeti, A., Zhang, B. Y., de Castro, I. A., Ou, J. Z., Carey, B. J., Mohiuddin, M., Datta, R., Xu, C., Mouritz, A. P., McConville, C. F., et al., Green synthesis of low-dimensional aluminum oxide hydroxide and oxide using liquid metal reaction media: Ultrahigh flux membranes. *Adv. Funct. Mater.* **2018**, *28* (44), 1804057.
6. Son, J. S., Yu, J. H., Kwon, S. G., Lee, J., Joo, J., Hyeon, T., Colloidal synthesis of ultrathin two-dimensional semiconductor nanocrystals. *Adv. Mater.* **2011**, *23* (28), 3214-3219.
7. Mohiuddin, M., Pillai, N., Zavabeti, A., Mahmood, N., Syed, N., Datta, R. S., Jampaiah, D., Daeneke, T., Ou, J. Z., Kalantar-Zadeh, K., Exploring electric field assisted van der Waals weakening of stratified crystals. *Appl. Mater. Today* **2018**, *12*, 359-365.

8. Wang, F., Wang, Z., Shifa, T. A., Wen, Y., Wang, F., Zhan, X., Wang, Q., Xu, K., Huang, Y., Yin, L., et al., Two-dimensional non-layered materials: Synthesis, properties and applications. *Adv. Funct. Mater.* **2017**, 27 (19), 1603254.
9. Chung, D. Y., Jun, S. W., Yoon, G., Kim, H., Yoo, J. M., Lee, K.-S., Kim, T., Shin, H., Sinha, A. K., Kwon, S. G., et al., Large-scale synthesis of carbon-shell-coated FeP nanoparticles for robust hydrogen evolution reaction electrocatalyst. *J. Am. Chem. Soc.* **2017**, 139 (19), 6669-6674.
10. Hu, Z., Xiao, X., Jin, H., Li, T., Chen, M., Liang, Z., Guo, Z., Li, J., Wan, J., Huang, L., et al., Rapid mass production of two-dimensional metal oxides and hydroxides *via* the molten salts method. *Nat. Commun.* **2017**, 8, 15630.
11. Tan, C., Zhang, H., Wet-chemical synthesis and applications of non-layer structured two-dimensional nanomaterials. *Nat. Commun.* **2015**, 6, 7873.
12. Cheng, W., He, J., Yao, T., Sun, Z., Jiang, Y., Liu, Q., Jiang, S., Hu, F., Xie, Z., He, B., et al., Half-unit-cell α -Fe₂O₃ semiconductor nanosheets with intrinsic and robust ferromagnetism. *J. Am. Chem. Soc.* **2014**, 136 (29), 10393-10398.
13. Liu, B., Yang, W., Li, J., Zhang, X., Niu, P., Jiang, X., Template approach to crystalline GaN nanosheets. *Nano Lett.* **2017**, 17 (5), 3195-3201.
14. Fan, Z., Liu, Y., Yan, J., Ning, G., Wang, Q., Wei, T., Zhi, L., Wei, F., Template-directed synthesis of pillared-porous carbon nanosheet architectures: High-performance electrode materials for supercapacitors. *Adv. Energy Mater.* **2012**, 2 (4), 419-424.
15. Puthirath Balan, A., Radhakrishnan, S., Woellner, C. F., Sinha, S. K., Deng, L., Reyes, C. d. l., Rao, B. M., Paulose, M., Neupane, R., Apte, A., et al., Exfoliation of a non-van der Waals material from iron ore hematite. *Nat. Nanotechnol.* **2018**, 13 (7), 602-609.

16. Dias, P., Vilanova, A., Lopes, T., Andrade, L., Mendes, A., Extremely stable bare hematite photoanode for solar water splitting. *Nano Energy* **2016**, 23, 70-79.
17. Jeon, T. H., Moon, G.-h., Park, H., Choi, W., Ultra-efficient and durable photoelectrochemical water oxidation using elaborately designed hematite nanorod arrays. *Nano Energy* **2017**, 39, 211-218.
18. Wang, G., Ling, Y., Wheeler, D. A., George, K. E. N., Horsley, K., Heske, C., Zhang, J. Z., Li, Y., Facile synthesis of highly photoactive α -Fe₂O₃-based films for water oxidation. *Nano Lett.* **2011**, 11 (8), 3503-3509.
19. Owusu, K. A., Qu, L., Li, J., Wang, Z., Zhao, K., Yang, C., Hercule, K. M., Lin, C., Shi, C., Wei, Q., et al., Low-crystalline iron oxide hydroxide nanoparticle anode for high-performance supercapacitors. *Nat. Commun.* **2017**, 8, 14264.
20. Zhang, E., Wang, B., Yu, X., Zhu, J., Wang, L., Lu, B., β -FeOOH on carbon nanotubes as a cathode material for Na-ion batteries. *Energy Storage Mater.* **2017**, 8, 147-152.
21. Zhang, X., Ge, J., Lei, B., Xue, Y., Du, Y., High quality β -FeOOH nanostructures constructed by a biomolecule-assisted hydrothermal approach and their pH-responsive drug delivery behaviors. *CrystEngComm* **2015**, 17 (22), 4064-4069.
22. Flak, D., Chen, Q., Mun, B. S., Liu, Z., Rękas, M., Braun, A., In situ ambient pressure XPS observation of surface chemistry and electronic structure of α -Fe₂O₃ and γ -Fe₂O₃ nanoparticles. *Appl. Surf. Sci.* **2018**, 455, 1019-1028.
23. Bashir, S., McCabe, R. W., Boxall, C., Leaver, M. S., Mobbs, D., Synthesis of α - and β -FeOOH iron oxide nanoparticles in non-ionic surfactant medium. *J. Nanoparticle Res.* **2009**, 11 (3), 701-706.
24. Xu, Z., Yu, Y., Fang, D., Xu, J., Liang, J., Zhou, L., Microwave–ultrasound assisted synthesis of β -FeOOH and its catalytic property in a photo-Fenton-like process. *Ultrason. Sonochem.* **2015**, 27, 287-295.

25. Dutcher, B., Fan, M., Leonard, B., Dyar, M. D., Tang, J., Speicher, E. A., Liu, P., Zhang, Y., Use of nanoporous FeOOH as a catalytic support for NaHCO₃ decomposition aimed at reduction of energy requirement of Na₂CO₃/NaHCO₃ based CO₂ separation technology. *J. Phys. Chem. C* **2011**, *115* (31), 15532-15544.
26. Deliyanni, E. A., Peleka, E. N., Matis, K. A., Effect of cationic surfactant on the adsorption of arsenites onto akaganeite nanocrystals. *Sep. Sci. and Technol.* **2007**, *42* (5), 993-1012.
27. Mohapatra, J., Mitra, A., Tyagi, H., Bahadur, D., Aslam, M., Iron oxide nanorods as high-performance magnetic resonance imaging contrast agents. *Nanoscale* **2015**, *7* (20), 9174-9184.
28. Xiao, X., Song, H., Lin, S., Zhou, Y., Zhan, X., Hu, Z., Zhang, Q., Sun, J., Yang, B., Li, T., et al., Scalable salt-templated synthesis of two-dimensional transition metal oxides. *Nat. Commun.* **2016**, *7*, 11296.
29. Robinson, R. D., Sadtler, B., Demchenko, D. O., Erdonmez, C. K., Wang, L.-W., Alivisatos, A. P., Spontaneous superlattice formation in nanorods through partial cation exchange. *Science* **2007**, *317* (5836), 355-358.
30. Wang, Z., Chen, Z., Zhang, H., Zhang, Z., Wu, H., Jin, M., Wu, C., Yang, D., Yin, Y., Lattice-mismatch-induced twinning for seeded growth of anisotropic nanostructures. *ACS Nano* **2015**, *9* (3), 3307-3313.

Chapter 6

Ultrathin iron phosphide nanostructures towards hydrogen evolution reaction[†]

[†] The contents of this chapter is under review in Mohiuddin et al., Synthesis of Two-Dimensional Hematite and Iron Phosphide for Hydrogen Evolution, *Journal of Materials Chemistry A*, 2019.

6.1 Introduction

Hydrogen could be an ideal carbon-neutral energy source to cope up with the fast increase in energy consumption. Water electrolysis to hydrogen and oxygen through electrical power source is promising for large scale fuel production^{1,2}. The design and development of low cost, earth-abundant and highly active catalysts for a wide range of energy conversion applications on a large scale are the primary concern for sustainable energy. The quest for stable, earth-abundant electrocatalysts with high efficiency remains a great challenge. The TMPs have been highlighted as promising candidates for electrocatalysts energy conversion application³⁻⁸. It is important to develop scalable and facile synthesis method of high quality, large quantity nanomaterials for energy application. In this chapter, a facile and scalable synthesis of 2D FeP nanosheets and nanonets for effective electrocatalyst for hydrogen evolution reaction (HER) has been described. The simple and low-cost synthesis method is suitable for large-scale production, and electrochemical measurements of electrocatalysts show high stability and activity in acidic media. Prepared highly efficient electrocatalyst could be an effective replacement of noble Pt-based electrocatalyst in energy devices.

6.2 Experimental section

6.2.1 Materials

α -Fe₂O₃ nanostructures prepared in Chapter 5, Sulfuric acid, H₂SO₄ ($\geq 99\%$, Sigma-Aldrich), Polytetrafluoroethylene, PTFE (60 wt%, Sigma-Aldrich), carbon paper, All chemicals were used without further purification.

6.2.2 Synthesis

Transformation to FeP was performed in a horizontal tubular furnace with continuous N₂ flow (50 sccm). α -Fe₂O₃@template was placed in a quartz crucible, and NaH₂PO₂ were placed on another quartz crucible. Quartz crucible of α -Fe₂O₃@template was positioned at the centre of the furnace whereas of NaH₂PO₂ crucible was positioned in upstream inside the furnace. The temperature of the furnace raised to 400 °C at the rate of 5 °C min⁻¹ then cool down to room temperature with N₂ flow. The total duration for the reaction process was 120 min after the temperature of the system had reached the desired temperature. At these temperatures, 2D nanostructures (nanosheets and nanonets) on template reacted with PH₃ vapour to convert to FeP. Nanonsheet and nanonets of FeP@template were washed with DI water to remove the template and redispersed in ethanol after filtration to obtain nanostructures for further characterisation.

6.2.3 Characterisations

TEM and HRTEM studies were performed on a JEOL 1010 and JEOL 2100F instruments, respectively operating at 100 and 200 kV, respectively. XPS was performed using a Thermo Scientific K-Alpha XPS spectrometer, and all the XPS results are calibrated at C-C (C 1s - 284.8 eV) to be used as a reference. The machine was featured with a monochromated Al K α X-ray source with a photon energy of 1486.7 eV and an X-ray spot size of 400 μ m. The samples were scanned with a pass energy of 50 eV and a dwell time of 50 ms. Data acquisition and processing were performed using Avantage software. XRD analysis was used to evaluate the

crystal structure of samples which was performed using a Bruker D4 Endeavour featuring a CuK α X-ray source ($\lambda = 1.54 \text{ \AA}$). For both cases, the operating voltage and current were at 40 kV and 40 mA, respectively. AFM images were recorded using a Bruker Dimension Icon AFM with nanoscope software. For the AFM measurements, the samples were drop-casted on Si substrate, which was pre-cleaned with acetone, IPA and DI water. Brunauer–Emmett–Teller (BET) surface area measurements were performed in Quantachrome ASiQwin. The BET surface area and pore size distribution were calculated from the nitrogen adsorption/desorption isotherms at 77 K.

6.2.4 Electrochemical measurements

Hydrogen evolution reaction was performed using a three-electrode configuration (CHI 760D) in 70 ml 0.5 M H₂SO₄ (pH = 0.3) electrolyte. Carbon paper (CP) coated with the samples was used as a working electrode whereas a graphite rod, and Ag/AgCl (in 1 M KCl aqueous solution) were used as a counter electrode, and a reference electrode, respectively. CP was used as a working electrode for electrochemical measurements because of the versatility and cost-effectiveness over other electrodes. The carbon paper was cleaned using ethanol and DI water prior coating carbon paper with samples. All the potentials shown in this paper were converted to RHE, and all the polarisation curves were iR corrected. The presented current density was normalised to the geometric surface area. Linear sweep voltammetry was performed at a 5 mV s⁻¹ scan rate to obtain the polarisation curves. All the tests were conducted at room temperature and ambient pressure. Inks of FeP was prepared by mixing 5 mg of materials powder and carbon black at 80% and 20% ratio in IPA and DI water mixture (1:1). 15 μ L PTFE solution (60% in H₂O, Sigma) was added followed by sonication for 10 min. Around 100 μ L of the suspension was drop-casted onto a carbon paper (CP) with an area of 0.25 cm². Electrochemical cyclic voltammetry measurements for determining EDLC were performed over a range of scan rates (10, 20, 30, 40, and 50 mV s⁻¹) at 0.15 V vs RHE. EIS was carried out at overpotential of

-0.1 mV (vs RHE) with AC signal amplitude of 5 mV. The stability test was also performed at a fixed potential.

6.3 Results and discussion

α -Fe₂O₃ nanostructures obtained using the synthesis method explained in Chapter 5, were phosphorised to form the stable nanostructures of FeP. The TEM image in Figure 6-1a clearly reveals the ultrathin nature of the FeP nanosheets. Apart from ultrathin morphology, a significant amount of mesopores are observed on the nanosheets as depicted in Figure 6-1a (circled in red). Upon conversion of α -Fe₂O₃ to FeP, the lattice spacing of 2.52 Å is observed which corresponds to the (120) crystal plane of orthorhombic FeP in accordance with the card No. JCPDS No. 65-2595, shown in Figure 6-1b⁹. Besides, the SAED pattern reveals the existence of (011) and (022) planes associated with the FeP according to card No. JCPDS No. 65-2595 (Figure 6-1c). The typical topography scan using AFM demonstrates the ultrathin features with thickness down to atomic level; for instance, FeP nanosheet shows thickness of 3 nm as shown in Figure 6-1d and e. The STEM-EDS mapping of a single nanosheet shows the evenly distributed Fe and P across the nanosheet, assuring successful conversion and high purity of the FeP (Figure 6-2). Moreover, the corresponding EDS spectrum of the nanosheet having reasonable signals of Fe and P showing the atomic ratio close to 1 also confirms the formation of FeP (inset of Figure 6-2a).

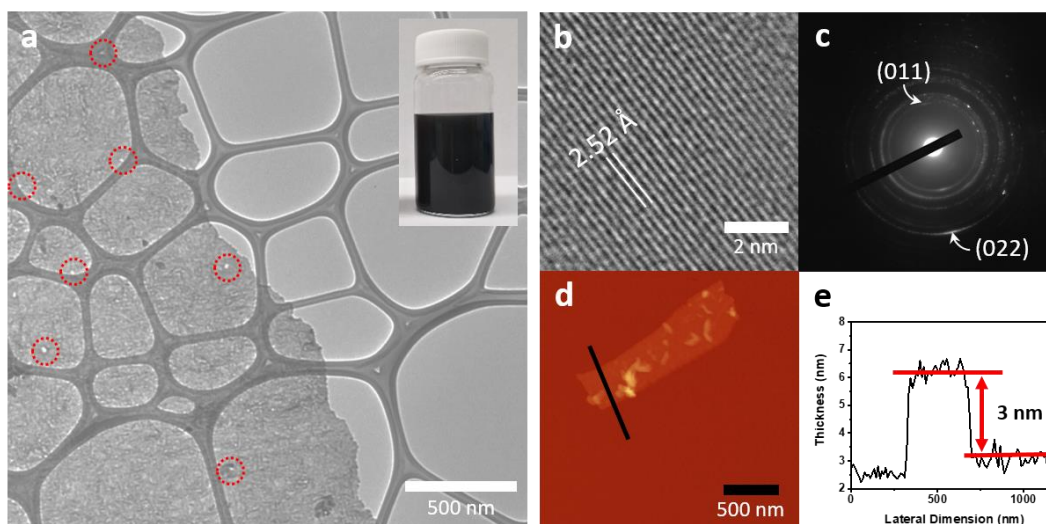


Figure 6-1 (a-c) low-, high-resolution TEM images, and SAED pattern of FeP nanosheets, respectively. (d) AFM images of FeP nanosheets with corresponding (e) thickness profile. The liquid suspension of FeP shown in the inset of a.

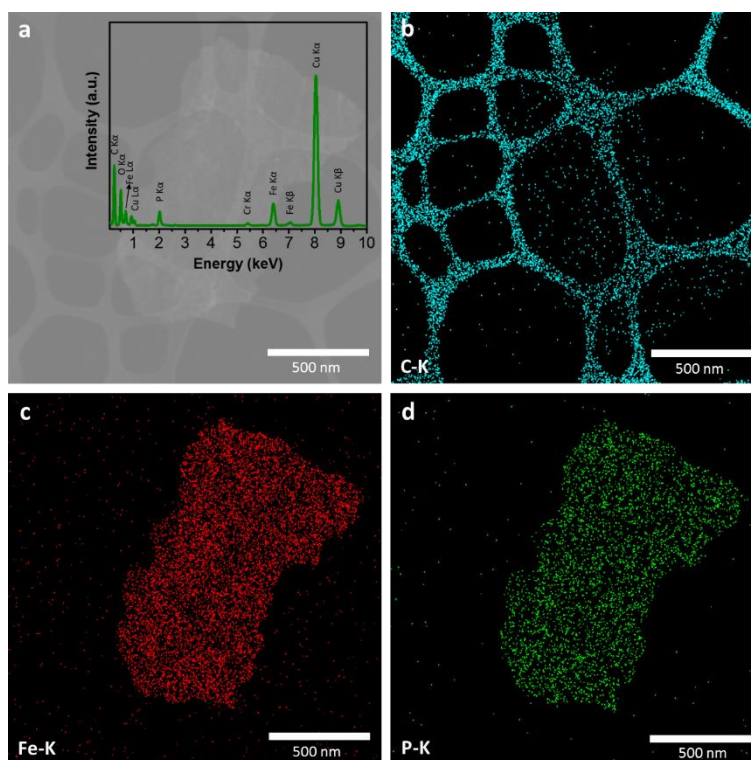


Figure 6-2 (a) STEM image along with (b-d) C, Fe and P elemental mapping of FeP nanosheet, respectively. STEM EDS spectrum of FeP nanosheets shown in the inset of a.

The high-resolution XPS of Fe 2p spectrum of FeP nanosheet is shown in Figure 6-3a. For FeP, peaks at ~707.2 eV (Fe 2p_{3/2}) and ~720.3 eV (Fe 2p_{1/2}) instigated from the bonding between Fe and P in FeP (Fe³⁺)¹⁰.

Moreover, oxidation of Fe species denoted by the peaks at ~711.5 and ~725 eV arise from Fe-O bond, which is probably associated with the formation of thin phosphate layer at the surface of FeP due to oxidation by air exposer^{11, 12}. In the P 2p region (Figure 6-3b) of FeP, the doublet of 2p_{3/2} and 2p_{1/2} appears at ~129.4 and ~130.3 eV, respectively, is initiated from the negatively charged P (P³⁻) ions of metal (Fe) and P bonding^{10, 13} and highly effective hydrogen evolution reaction of FeP resulting from the synergy of proton acceptor P sites and hydride acceptor metal sites¹⁴. The strong peak at ~133.6 eV indicates P-O bond of surface phosphate forms which was also observed in O 1s scan (Figure 6-3c) of FeP nanosheets^{11, 12}. The crystal structure and phase purity of FeP samples are investigated by XRD, as shown in Figure 6-3d. Upon phosphorisation reddish colour of α -Fe₂O₃ nanosheets turns to black. Moreover, characteristic diffraction peaks of FeP confirm the transformation of α -Fe₂O₃ to orthorhombic FeP (JCPDS No. 65-2595).

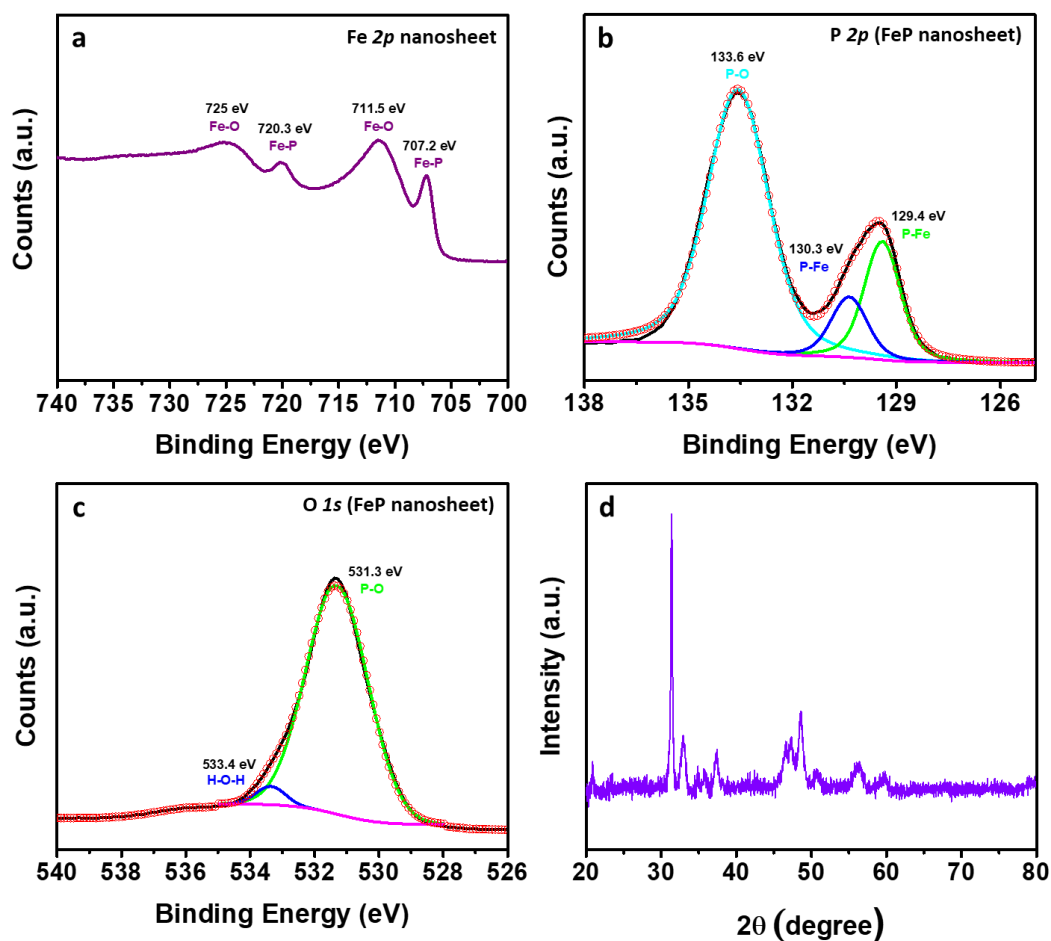


Figure 6-3 Structure and surface characterisations. XPS spectrum of FeP nanosheets (a) Fe 2p (b) P 2p (c) O 1s and (d) XRD pattern.

Although the morphology of nanosheet did not change after phosphorisation, nanonet building block nanorods are transformed into the network of nanoparticles (Figure 6-4a). Lattice fringes (Figure 6-4b) from the HRTEM show the d-spacing is approximately 2.42 Å, corresponding to the (111) crystal plane of orthorhombic FeP which further validated by the SAED of Figure 6-4c. The AFM image and corresponding thickness profile as shown in Figure 6-4d and e reveal the thickness of a typical nanoparticle of FeP. The thickness of individual nanoparticles in FeP nanonet is estimated to be ~9 nm. The EDS elemental mapping (Figure 6-5) and spectrum (Figure 6-5a inset) of a single FeP nanonet in the STEM mode shows a similar outcome to FeP nanosheet.

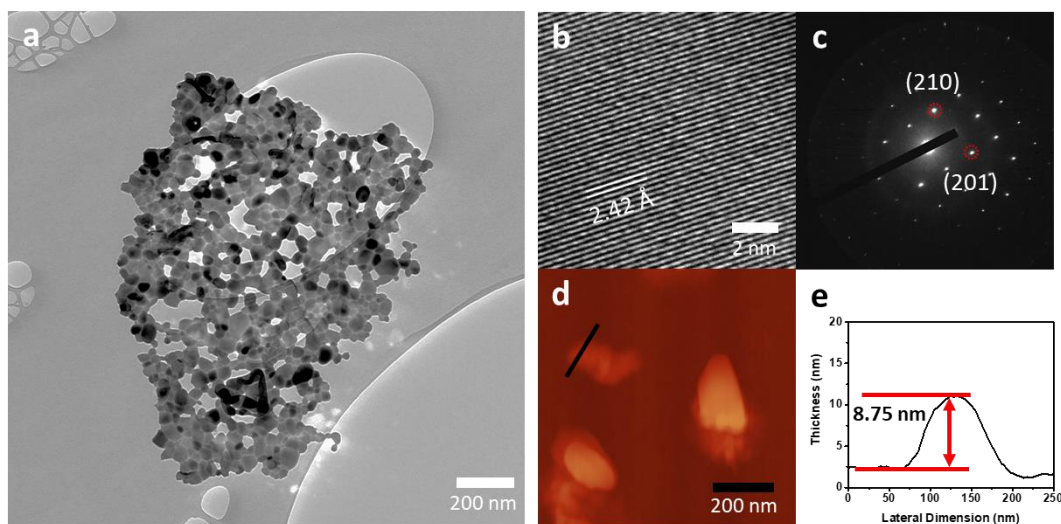


Figure 6-4 (a-c) low-, high-resolution TEM images, and SAED pattern of FeP nanonets, respectively. (d) AFM images of FeP nanonet with corresponding (e) thickness profile.

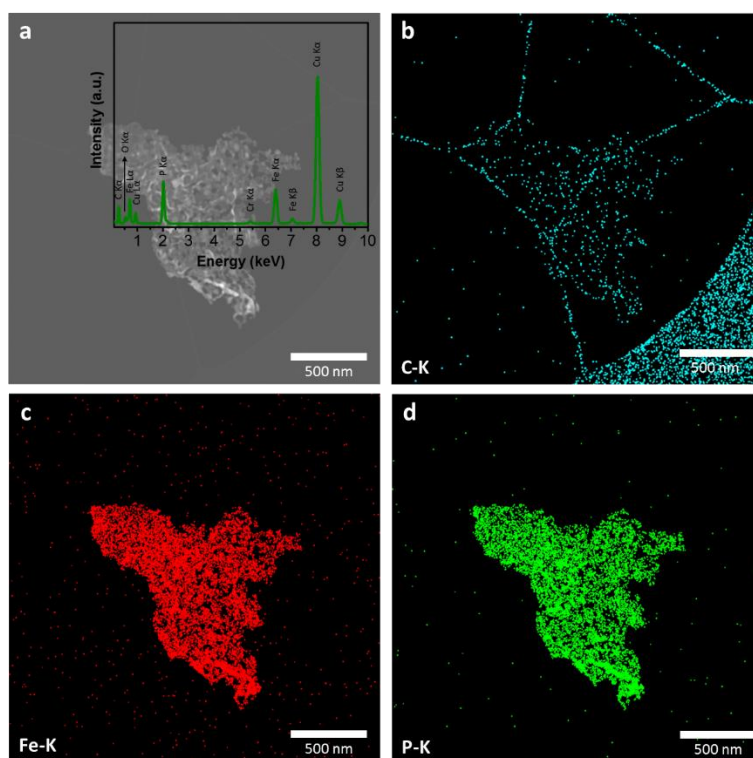


Figure 6-5 (a) STEM image along with (b-d) C, Fe and O elemental mapping of α -Fe₂O₃ nanonet, respectively. STEM EDS spectrum of α -Fe₂O₃ nanonet shown in the inset of a.

The catalyst activity of FeP preliminary assessed by BET surface area measurements. Figure 6-6 shows N₂ sorption isotherms and the pore size distributions (inset) of FeP nanosheets and

nanonets. The specific surface area of FeP nanosheets is calculated to be 50.164 m²/g which is >40% larger than FeP nanonets (35.285 m²/g). As depicted in pore size distributions, both nanosheets and nanonets exhibit a sharp pore size distribution ranging between 2 - 5 nm centred at ~2.7 nm. However, pore volume of nanosheets (0.095 cc/g) is >60% higher than nanonets (0.059 cc/g). The high surface area and porous networks support the high density of active edge sites to the electrolyte.

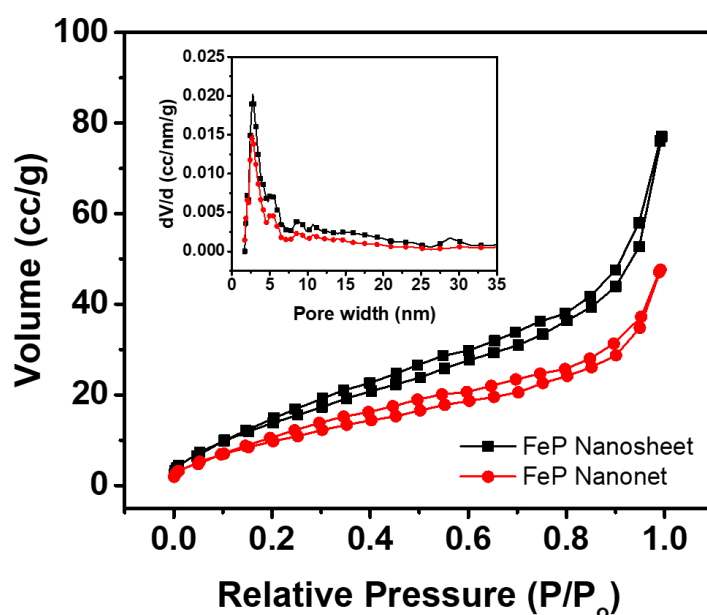


Figure 6-6 Nitrogen sorption isotherms and pore size distribution curves (inset) of FeP nanosheets and nanonets.

FeP has proved to be one of the best non-precious element based candidate for HER electrocatalyst. Therefore, both nanosheets and nanonets have been examined for HER electrocatalyst performance. The electrocatalytic activity of the nanosheets and nanonets is evaluated by electrochemical measurements. Commercial 20% Pt/C and a blank carbon paper are also examined for the comparison of the performances. The polarisation curves of nanosheets and nanonets loaded on carbon paper (1.6 mg cm⁻²) in acidic 0.5 M H₂SO₄ solution shown in Figure 6-7a. Pt/C shows the best HER activity with an overpotential of 38 mV to achieve 10 mA cm⁻² current density (η_{10}). As expected, the current density of carbon paper is negligible and large

current density is only associated with the FeP nanosheets and nanonets (Figure 6-7a). Among, nanosheets and nanonets, the FeP nanosheets electrode shows the smallest overpotential (η_{10}) as low as 117 mV, with the increase of the absolute value of potential the cathodic current intensity increases dramatically proves the high catalytic activity of ultrathin FeP nanosheets over nanonets ($\eta_{10} = 138$ mV) for HER. To extend the performance examination of the reaction kinetics and the determination of HER mechanism, the corresponding Tafel plots and exchange current density based on the polarisation curves are presented in Figure 6-7b. A Tafel slope describes the elementary steps during the hydrogen evolution process. The Tafel slopes of Pt/C, FeP nanosheets and FeP nanonets are 34, 56, and 60 mV dec⁻¹, respectively. The Tafel slope of FeP nanosheets is lower than that of FeP nanonets, indicates the superior electrode kinetics of FeP nanosheets.

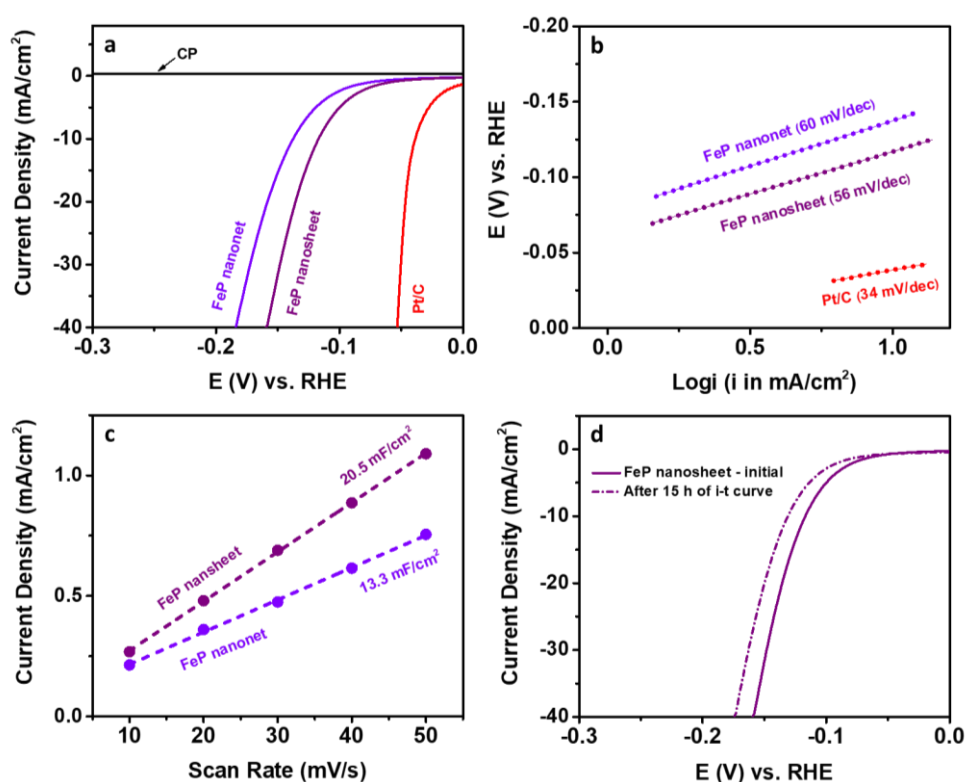


Figure 6-7 Electrochemical HER performances of FeP nanosheets and nanonets measured in acidic media. (a) Polarisation curves, (b) and their corresponding Tafel slopes, (c) Electrochemically active surface area as a function of scan rate of FeP nanosheets and nanonets, (d) The polarisation curve before and after the 15 h of stability test of FeP nanosheets.

Electrochemical impedance spectroscopy (EIS) data shown in Figure 6-8, indicates the insight of the electron transferability. The Nyquist plots derived from EIS measurements converted to an equivalent circuit (Randle's circuit) shown in the inset of Figure 6-8 to estimate the charge transfer resistance (R_{ct}) at solid/liquid interface of the catalyst. Smaller the R_{ct} faster the HER kinetics. The semicircle diameter of FeP nanosheets and nanonets is $\sim 1 \Omega$, implies the similar R_{ct} of both nanostructures.

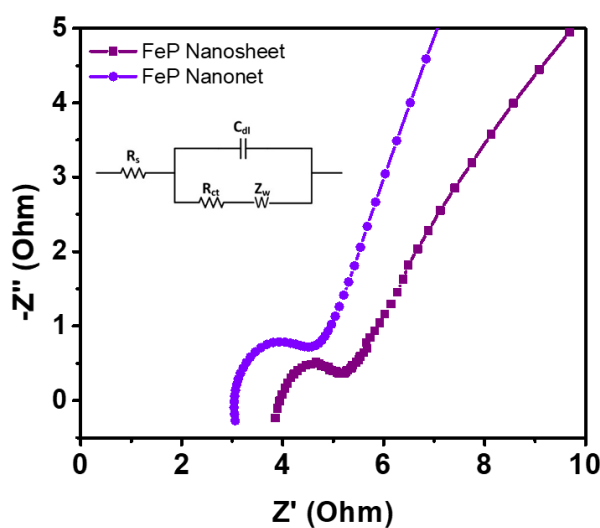


Figure 6-8 EIS Nyquist plot, showing charge transfer resistance of FeP nanosheets and nanonets.

The abundance of surface-active sites has pronounced influences in HER performance; therefore, electrochemically active surface area (ECSA) of catalysts evaluated through electrochemical double-layer capacitance (EDLC) at 0.15 V vs RHE. Figure 6-9 shows the CV curves of both FeP nanosheets and nanonets at a specified voltage range of 0.1- 0.2 V vs RHE with different scan rates. As presented in the slope of Figure 6-7c, FeP nanosheets electrode exhibit a capacitance of 20.5 mF cm^{-2} , which is more than 50% higher than FeP nanonets (13.3 mF cm^{-2}), demonstrating the presence of more electrochemically active sites in FeP nanosheets compare to FeP nanonets. The higher C_{dl} values for FeP nanosheets are also highlighting the advantages of mesopores over macropores as observed in TEM of nanosheets and nanonets,

respectively, although, the macropores are only favourable for better mass transport but limited with active sites.

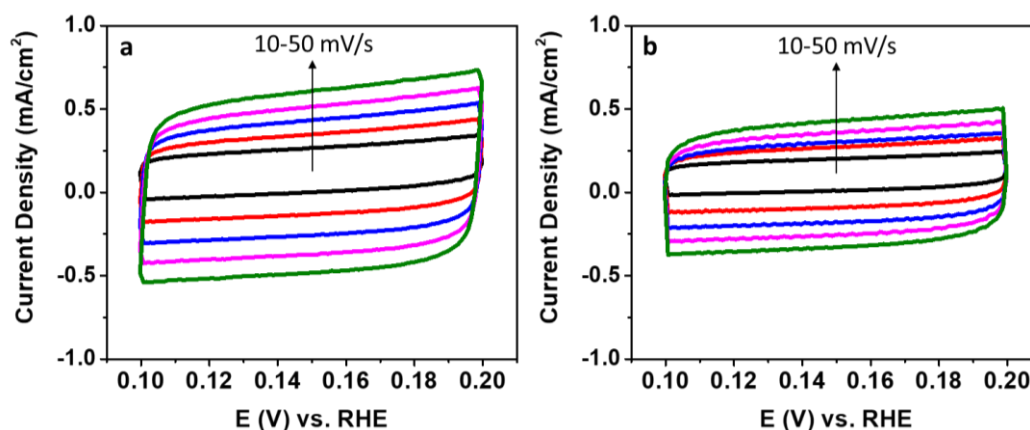


Figure 6-9 Cyclic voltammetry (CV) curves in 0.5 M H₂SO₄ for (a) FeP nanosheets, (b) FeP nanonets in the region of 0.10~0.20 V vs. RHE at various scan rates.

In durability test represented in Figure 6-7d, the negligible difference has been observed in the polarisation curves of FeP nanosheets before and after the 15 h stability test. In addition to the overpotential (η_{10}), Tafel slope, durability, ESCA show the superiority of FeP nanosheets. Superior electrochemical performance of ultrathin FeP nanosheets over nanonets can be ascribed to the large surface areas of ultrathin nanosheets and the surface nanopores which facilitate the diffusion of the liquid electrolyte. In order to confirm the long-term performance consistency, both FeP nanosheets and nanonets were examined at a constant potential for 15 h as shown in Figure 6-10. Current density kept consistent throughout the operation indicates the comparable long-term performance of FeP nanostructures. Overall, the HER results are compared to the reports of HER activity of freestanding single metal phosphides and imply that the comparable performance of FeP nanostructures with those reports and excellent alternate of noble metal-based electrocatalyst for hydrogen production (Table 6-1).

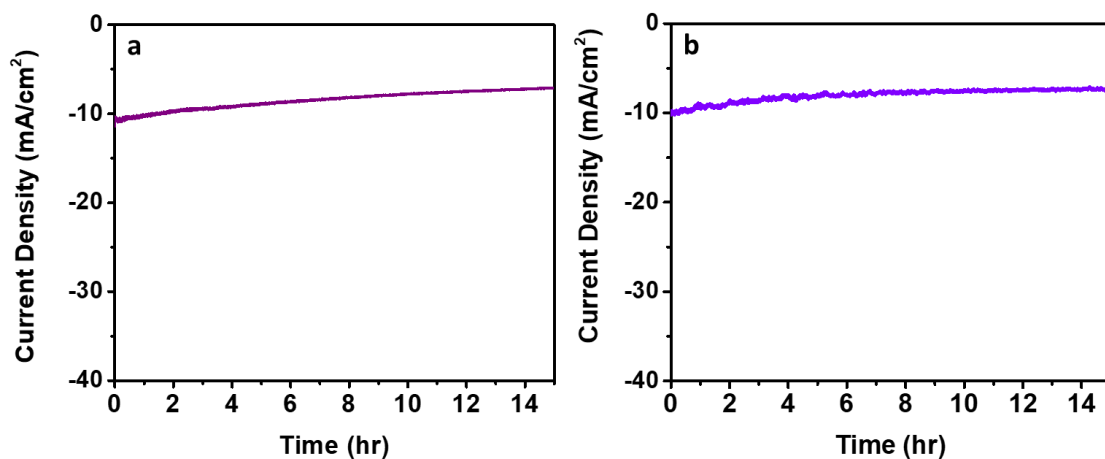


Figure 6-10 Time-dependent HER current density of FeP (a) nanosheets (b) nanonets.

Table 6-1 Comparison of the HER activity of free-standing single metal phosphide based electrocatalysts in acidic media (0.5 M H₂SO₄).

Electrocatalysts	Working electrode	Mass loading (mg cm ⁻²)	Overpotential (mV@ η_{10})	Tafel slope (mV dec ⁻¹)	Reference
Ultrathin FeP nanosheets	CP	1.6	117	56	This work
Nanoporous FeP nanosheets	GCE	0.28	250	67	15
FeP nanowires	GCE	1.02	193	66	16
CoP nanotubes	GCE	0.2	129	60	17
CoP NWs	GCE	0.35	110	54	18
defect-rich MoP	GCE	0.2	156	49	19
MoP microparticles	GCE/FTO	0.1	150	50	20
MoP	GCE	0.86	~130	54	21
Ni ₅ P ₄ nanocrystals	GCE	1.99	118	42	22
WP ₂ submicroparticles	GCE	0.5	161	57	23

6.4 Conclusions

In summary, FeP nanostructures have been demonstrated for hydrogen evolution reaction. FeP nanostructures successfully synthesised from 2D α -Fe₂O₃ through one step phosphorisation process. FeP nanosheets retain the structural integrity in crystalline template during the phosphorisation process. However, shape transformation has been observed for the nanonets morphology but the network of nanonets is well preserved by the crystalline template. Electrocatalytic activities of FeP nanosheets outperformed the FeP nanonets in terms of overpotential, Tafel slope, and surface-active sites. Altogether, the template synthesis enables the facile and scalable process for synthesising low dimensional non-layered iron compounds which could open the new opportunities for the commercial production of energy conversion nanomaterials.

References

1. Kudo, A., Miseki, Y., Heterogeneous photocatalyst materials for water splitting. *Chem. Soc. Rev.* **2009**, 38 (1), 253-278.
2. Walter, M. G., Warren, E. L., McKone, J. R., Boettcher, S. W., Mi, Q., Santori, E. A., Lewis, N. S., Solar water splitting cells. *Chem. Rev.* **2010**, 110 (11), 6446-6473.
3. Jiang, P., Liu, Q., Liang, Y., Tian, J., Asiri, A. M., Sun, X., A cost-effective 3D hydrogen evolution cathode with high catalytic activity: FeP nanowire array as the active phase. *Angew. Chem. Int. Ed.* **2014**, 53 (47), 12855-12859.
4. Zhou, Q., Shen, Z., Zhu, C., Li, J., Ding, Z., Wang, P., Pan, F., Zhang, Z., Ma, H., Wang, S., et al., Nitrogen-doped CoP electrocatalysts for coupled hydrogen evolution and sulfur generation with low energy consumption. *Adv. Mater.* **2018**, 30 (27), 1800140.

5. Chen, M., Qi, J., Zhang, W., Cao, R., Electrosynthesis of NiP_x nanospheres for electrocatalytic hydrogen evolution from a neutral aqueous solution. *ChemComm* **2017**, 53 (40), 5507-5510.
6. Pu, Z., Saana Amiinu, I., Wang, M., Yang, Y., Mu, S., Semimetallic MoP₂: An active and stable hydrogen evolution electrocatalyst over the whole pH range. *Nanoscale* **2016**, 8 (16), 8500-8504.
7. Xia, W., Mahmood, A., Liang, Z., Zou, R., Guo, S., Earth-abundant nanomaterials for oxygen reduction. *Angew. Chem. Int. Ed.* **2016**, 55 (8), 2650-2676.
8. Zhu, J., Wu, Q., Key, J., Wu, M., Shen, P. K., Self-assembled superstructure of carbon-wrapped, single-crystalline Cu₃P porous nanosheets: One-step synthesis and enhanced Li-ion battery anode performance. *Energy Storage Mater.* **2018**, 15, 75-81.
9. Lv, C., Peng, Z., Zhao, Y., Huang, Z., Zhang, C., The hierarchical nanowires array of iron phosphide integrated on a carbon fiber paper as an effective electrocatalyst for hydrogen generation. *J. Mater. Chem. A* **2016**, 4 (4), 1454-1460.
10. Tian, L., Yan, X., Chen, X., Electrochemical activity of iron phosphide nanoparticles in hydrogen evolution reaction. *ACS Catal.* **2016**, 6 (8), 5441-5448.
11. Ma, F.-X., Xu, C.-Y., Lyu, F., Song, B., Sun, S.-C., Li, Y. Y., Lu, J., Zhen, L., Construction of FeP hollow nanoparticles densely encapsulated in carbon nanosheet frameworks for efficient and durable electrocatalytic hydrogen production. *Adv. Sci.* **2019**, 6 (3), 1801490.
12. Xiong, D., Wang, X., Li, W., Liu, L., Facile synthesis of iron phosphide nanorods for efficient and durable electrochemical oxygen evolution. *ChemComm* **2016**, 52 (56), 8711-8714.

13. Yan, Y., Shi, X. R., Miao, M., He, T., Dong, Z. H., Zhan, K., Yang, J. H., Zhao, B., Xia, B. Y., Bio-inspired design of hierarchical FeP nanostructure arrays for the hydrogen evolution reaction. *Nano Res.* **2018**, *11* (7), 3537-3547.
14. Yu, J., Li, Q., Li, Y., Xu, C.-Y., Zhen, L., Dravid, V. P., Wu, J., Ternary metal phosphide with triple-layered structure as a low-cost and efficient electrocatalyst for bifunctional water splitting. *Adv. Funct. Mater.* **2016**, *26* (42), 7644-7651.
15. Xu, Y., Wu, R., Zhang, J., Shi, Y., Zhang, B., Anion-exchange synthesis of nanoporous FeP nanosheets as electrocatalysts for hydrogen evolution reaction. *ChemComm* **2013**, *49* (59), 6656-6658.
16. Son, C. Y., Kwak, I. H., Lim, Y. R., Park, J., FeP and FeP₂ nanowires for efficient electrocatalytic hydrogen evolution reaction. *ChemComm* **2016**, *52* (13), 2819-2822.
17. Du, H., Liu, Q., Cheng, N., Asiri, A. M., Sun, X., Li, C. M., Template-assisted synthesis of CoP nanotubes to efficiently catalyze hydrogen-evolving reaction. *J. Mater. Chem. A* **2014**, *2* (36), 14812-14816.
18. Jiang, P., Liu, Q., Ge, C., Cui, W., Pu, Z., Asiri, A. M., Sun, X., CoP nanostructures with different morphologies: synthesis, characterization and a study of their electrocatalytic performance toward the hydrogen evolution reaction. *J. Mater. Chem. A* **2014**, *2* (35), 14634-14640.
19. Zhang, X., Guo, T., Liu, T., Lv, K., Wu, Z., Wang, D., Tungsten phosphide (WP) nanoparticles with tunable crystallinity, W vacancies, and electronic structures for hydrogen production. *Electrochim. Acta* **2019**, 134798.
20. Wang, T., Du, K., Liu, W., Zhu, Z., Shao, Y., Li, M., Enhanced electrocatalytic activity of MoP microparticles for hydrogen evolution by grinding and electrochemical activation. *J. Mater. Chem. A* **2015**, *3* (8), 4368-4373.

21. Xiao, P., Sk, M. A., Thia, L., Ge, X., Lim, R. J., Wang, J.-Y., Lim, K. H., Wang, X., Molybdenum phosphide as an efficient electrocatalyst for the hydrogen evolution reaction. *Energy Environ. Sci.* **2014**, 7 (8), 2624-2629.
22. Pan, Y., Liu, Y., Zhao, J., Yang, K., Liang, J., Liu, D., Hu, W., Liu, D., Liu, Y., Liu, C., Monodispersed nickel phosphide nanocrystals with different phases: synthesis, characterization and electrocatalytic properties for hydrogen evolution. *J. Mater. Chem. A* **2015**, 3 (4), 1656-1665.
23. Xing, Z., Liu, Q., Asiri, A. M., Sun, X., High-efficiency electrochemical hydrogen evolution catalyzed by tungsten phosphide submicroparticles. *ACS Catal.* **2015**, 5 (1), 145-149.

Chapter 7

Conclusions and future work

7.1 Conclusions

This PhD research develops the novel synthesis of ultrathin 2D naturally occurred layered and non-layered transition metal compounds and their applications in electrocatalyst. Throughout this research, various liquid-phase synthesis techniques were developed and investigated, resulting in the contribution to the advancement in the area of transition metal compounds, which include MoS₂, WS₂, α -Fe₂O₃, and FeP. The key discussions of four specific stages and the outcomes of each topic are as follows:

7.1.1 Phase 1

At the initial phase, this thesis explored the novel liquid-phase synthesis concept of atomically-thin 2D piezoelectric MoS₂ from naturally layered stratified bulk crystal using a microcentrifugation SAW device. The exfoliated MoS₂ was characterised in details using AFM, TEM, Raman, XPS etc. In just 25 min of exfoliation process, it has been found that the majority of the nanosheet thicknesses were ranged between ~1.2 to ~2 nm corresponding to mono and double layer of MoS₂, respectively. Moreover, a yield per unit of time of 3.816 (%)/h along with 58% of monolayer was achieved utilising the developed system which was compared to the previously published reports based on the single-step liquid-phase exfoliation of MoS₂. Concomitant electric and mechanical fields are applied using a SAW during micro-exfoliation process in SAW device. While the inherit effect of shear stress is similar to the one applied during agitation based exfoliation techniques, the accompanying electric field is proven

to be critical in enhancing the exfoliation efficiency of piezoelectric MoS₂. Then, the impact of electric field was investigated using a density functional theory model to explore a theoretical prediction for the frequency of monolayers, which is found to be in a very good agreement with the experiments.

7.1.2 Phase 2

The effect of chemical and mechanical components of the stratified crystals and solvents have been the topics of many investigations so far. It is known that stratified crystals such as molybdenum disulphide (MoS₂) and tungsten disulphide (WS₂) become non-centrosymmetric at their interfaces and show piezoelectricity. Therefore, utilising the exfoliation concept performed in a microdevice in phase 1, the 2D TMDs were exfoliated using a facile alternative method exploiting the piezoelectric nature. The effect of the electric field in the presence of different solvent for the exfoliation of WS₂, MoS₂ and graphene. Initial investigations were confirmed through intensive optical characterisations. The increase of the efficiency is obtained only for the case of WS₂ and Dimethylformamide (DMF) which was further confirmed by vibrational, structural and optical characterisations. After a comprehensive study, we associated the efficiency with the matching of the dispersive component of the cosolvent and target materials. Besides, the electric field-assisted WS₂ nanosheets showed better HER performance with overpotential of ~ 376 mV and Tafel slope of 125 mV dec⁻¹, compare to sonication only exfoliation. Altogether the work shows the possibility of tuning electric field/solvents for exfoliation of target stratified TMDs, but more importantly, provides critical guidance regarding the choice of parameters in the exfoliation procedure in the presence of electric field.

7.1.3 Phase 3

At this phase, a facile and scalable synthesis method of ultrathin layers of naturally non-layered hematite ($\alpha\text{-Fe}_2\text{O}_3$) which cannot be obtained through conventional synthesis has been demonstrated. Less expensive and water-soluble template synthesis approach followed by annealing has been utilised to synthesise 2D nanosheets of hexagonal $\alpha\text{-Fe}_2\text{O}_3$ down to ~ 1 nm with lateral size up to $10\ \mu\text{m}$. During a thorough investigation, the growth of ultrathin nanosheets has been observed due to the close lattice matching between the crystalline template and the target material. Moreover, lattice strain-induced shape transformation to anisotropic structure has also been introduced through the simple aging process. Further investigation revealed that the presence of small lattice mismatch between template and growing material is responsible for the anisotropic shape transformation. The growth mechanisms of nanostructures (nanosheets and nanonets) have thoroughly been explained and validated in details using XRD and TEM. Electron microscopy, XRD and XPS analyses demonstrated the high purity freestanding nature of 2D nanostructures. Furthermore, electrocatalytic HER performance of both the nanosheet and nanonet of $\alpha\text{-Fe}_2\text{O}_3$ were tested in order to compare their performances. In acidic media, the nanostructures were found to require an overpotential of 800 mV to achieve $10\ \text{mA cm}^{-2}$ current density. As $\alpha\text{-Fe}_2\text{O}_3$ nanostructures required high overpotential for HER thus better electrocatalyst is needed to develop which have optimised hydrogen adsorption energy like transitional metal phosphide, so the next phase will explain the efforts towards developing unique 2D metal phosphide.

7.1.4 Phase 4

An extension of the previous project leads to the conversion of $\alpha\text{-Fe}_2\text{O}_3$ through single-step phosphorisation to produce nanostructures of iron phosphide. Structural and morphological characterisations confirmed the complete conversion of 2D hexagonal $\alpha\text{-Fe}_2\text{O}_3$ to 2D

orthorhombic FeP. Both FeP nanosheets and porous nanostructure were utilised to prepare free-standing electrode on carbon paper to be used as electrocatalyst towards HER. The FeP nanosheets show overpotential of 117 mV to achieve 10 mA cm^{-2} which is 138 mV for porous nanostructure. Moreover, the Tafel slope of nanosheets and nanonets were 56 and 60 mV dec^{-1} , respectively and both were stable for the 15 h in acidic media. FeP nanosheets have more HER active sites through the exposure of more atoms from ultrathin structure and nanopores which significantly improved the HER reaction kinetics. This suggests the high potential of the synthesised 2D metal phosphide nanostructures in various electrocatalytic applications. The influential factors in achieving high HER activity were found to be the large electrochemical active surface area of the 2D nanosheets over nanonets. These properties significantly intensified the density of catalytic sites for highly active HER performance. The prospects of the developed work will be discussed in the later section.

7.2 Future work

Significant advancements and novel outcomes presented in this thesis provide enormous opportunities for further investigations. In extend to the outcomes presented in this thesis, the following future recommendations can be conducted:

- The fundamental effect of electric field on the exfoliation efficiency of piezoelectric 2D MoS_2 described in the first section provides alternative opportunities to improve exfoliation efficiency in liquid-phase to other 2D materials those are intrinsically piezoelectric. Large piezoelectricity has theoretically been predicted in intrinsic group IV monochalcogenides (MX , $\text{M}=\text{Sn}$ or Ge , $\text{X}=\text{Se}$ or S) monolayer; therefore, the study can be extended to group IV monochalcogenides.
- Through the careful analysis of lattice parameters of different inexpensive salts as a template, numerous other 2D oxides formation can potentially be designed and synthesised.

- Environment-friendly, earth abundance and low toxicity of hematite made it an attractive material in diversified applications. More particularly, light absorption ability of hematite makes it attractive for energy conversion; therefore, ultrathin nanosheets of hematite for photoelectrocatalyst could be investigated further. Moreover, the porosity in nanonets of hematite along with the unique properties to remove arsenic could be studied in nanofiltration for water purification.
- In the study, the synthesis of only FeP nanostructures for HER has been evaluated. Apart, doping with an additional element (e.g. N, H₂, Ni) or use of multi-metal instead of single metal can tune the material properties could be explored further to optimise the hydrogen adsorption energy. Moreover, it has been found that the active materials are more vulnerable to acidic degradation; therefore, carbon encapsulation could further be incorporated and investigated to improve charge transfer and overall performance.

7.3 List of publications

List of journal publications:

1. **Liquid phase acoustic wave exfoliation of layered MoS₂: Critical impact of electric field in efficiency**
M. Mohiuddin, Y. Wang, A. Zavabeti, N. Syed, R. S. Datta, H. Ahmed, T. Daeneke, S. P. Russo, A. R. Rezk, L. Y. Yeo, K. Kalantar-Zadeh
Chemistry of Materials **2018**, 30, 5593. DOI: 10.1021/acs.chemmater.8b01506.
2. **Exploring electric field assisted van der Waals weakening of stratified crystals**
M. Mohiuddin, N. Pillai, A. Zavabeti, N. Mahmood, N. Syed, R. S. Datta, D. Jampaiah, T. Daeneke, J. Z. Ou, K. Kalantar-Zadeh
Applied Materials Today **2018**, 12, 359. DOI: 10.1016/j.apmt.2018.05.005.
3. **Synthesis of ultrathin iron phosphide from hematite towards hydrogen evolution**
M. Mohiuddin, A. Zavabeti, F. Haque, N. Syed, M. W. Khan, A. Jannat, R. Datta, K. Messalea, Nasir Mahmood, Jianzhen Ou
Under review, *Journal of Materials Chemistry A*.
4. **Atomically thin Ga₂S₃ from skin of liquid metals for electrical, optical, and sensing applications**
M. M. Y. A. Alsaif, N. Pillai, S. Kuriakose, S. Walia, A. Jannat, K. Xu, T. Alkathiri, **M. Mohiuddin**, T. Daeneke, K. Kalantar-Zadeh, J. Z. Ou, A. Zavabeti
ACS Applied Nano Materials **2019**, 2, 4665. DOI: 10.1021/acsanm.9b01133.
5. **2D SnO/In₂O₃ van der Waals heterostructure photodetector based on printed oxide skin of liquid metals**
M. M. Y. A. Alsaif, S. Kuriakose, S. Walia, N. Syed, A. Jannat, B. Y. Zhang, F. Haque, **M. Mohiuddin**, T. Alkathiri, N. Pillai, T. Daeneke, J. Z. Ou, A. Zavabeti
Advanced Materials Interfaces **2019**, 6, 1900007. DOI: 10.1002/admi.201900007.

6. **Wafer-sized ultrathin gallium and indium nitride nanosheets through the ammonolysis of liquid metal derived oxides**

N. Syed, A. Zavabeti, K. A. Messalea, E. Della Gaspera, A. Elbourne, A. Jannat, **M. Mohiuddin**, B. Y. Zhang, G. Zheng, L. Wang, S. P. Russo, E. Dorna, C. F. McConville, K. Kalantar-Zadeh, T. Daeneke

Journal of the American Chemical Society **2019**, 141, 104. DOI: 10.1021/jacs.8b11483.

7. **Exfoliation behavior of van der Waals strings: Case study of Bi₂S₃**

N. Dhar, N. Syed, **M. Mohiuddin**, A. Jannat, A. Zavabeti, B. Y. Zhang, R. S. Datta, P. Atkin, N. Mahmood, D. Esrafilzadeh, T. Daeneke, K. Kalantar-Zadeh

ACS Applied Materials & Interfaces **2018**, 10, 42603. DOI: 10.1021/acsami.8b14702.

8. **Green synthesis of low-dimensional aluminum oxide hydroxide and oxide using liquid metal reaction media: ultrahigh flux membranes**

A. Zavabeti, B. Y. Zhang, I. A. de Castro, J. Z. Ou, B. J. Carey, **M. Mohiuddin**, R. Datta, C. Xu, A. P. Mouritz, C. F. McConville, A. P. O'Mullane, T. Daeneke, K. Kalantar-Zadeh

Advanced Functional Materials **2018**, 28, 1804057. DOI: 10.1002/adfm.201804057.

9. **Printing two-dimensional gallium phosphate out of liquid metal**

N. Syed, A. Zavabeti, J. Z. Ou, **M. Mohiuddin**, N. Pillai, B. J. Carey, B. Y. Zhang, R. S. Datta, A. Jannat, F. Haque, K. A. Messalea, C. Xu, S. P. Russo, C. F. McConville, T. Daeneke, K. Kalantar-Zadeh

Nature Communications **2018**, 9, 3618. DOI: 10.1038/s41467-018-06124-1.

10. **Two dimensional PbMoO₄: A photocatalytic material derived from a naturally non-layered crystal**

R. S. Datta, J. Z. Ou, **M. Mohiuddin**, B. J. Carey, B. Y. Zhang, H. Khan, N. Syed, A. Zavabeti, F. Haque, T. Daeneke, K. Kalantar-zadeh

Nano Energy **2018**, 49, 237. DOI: 10.1016/j.nanoen.2018.04.041.

11. Ultrafast acoustofluidic exfoliation of stratified crystals

H. Ahmed, A. R. Rezk, B. J. Carey, Y. Wang, **M. Mohiuddin**, K. J. Berean, S. P. Russo, K. Kalantar-zadeh, L. Y. Yeo

Advanced Materials **2018**, 30, 1704756. DOI:10.1002/adma.201704756.

12. Bi₂O₃ monolayers from elemental liquid bismuth

K. A. Messalea, B. J. Carey, A. Jannat, N. Syed, **M. Mohiuddin**, B. Y. Zhang, A. Zavabeti, T. Ahmed, N. Mahmood, E. Della Gaspera, K. Khoshmanesh, K. Kalantar-Zadeh, T. Daeneke

Nanoscale **2018**, 10, 15615. DOI: 10.1039/C8NR03788D.

13. Sonication-assisted synthesis of gallium oxide suspensions featuring trap state absorption: test of photochemistry

N. Syed, A. Zavabeti, **M. Mohiuddin**, B. Zhang, Y. Wang, R. S. Datta, P. Atkin, B. J. Carey, C. Tan, J. van Embden, A. S. R. Chesman, J. Z. Ou, T. Daeneke, K. Kalantar-zadeh

Advanced Functional Materials **2017**, 27, 1702295. DOI: 10.1002/adfm.201702295.

14. Quasi physisorptive two dimensional tungsten oxide nanosheets with extraordinary sensitivity and selectivity to NO₂

H. Khan, A. Zavabeti, Y. Wang, C. J. Harrison, B. J. Carey, **M. Mohiuddin**, A. F. Chrimes, I. A. De Castro, B. Y. Zhang, Y. M. Sabri, S. K. Bhargava, J. Z. Ou, T. Daeneke, S. P. Russo, Y. Li, K. Kalantar-zadeh

Nanoscale **2017**, 9, 19162. 10.1039/C7NR05403C.

15. Highly active two dimensional α -MoO_{3-x} for the electrocatalytic hydrogen evolution reaction

R. S. Datta, F. Haque, **M. Mohiuddin**, B. J. Carey, N. Syed, A. Zavabeti, B. Zhang, H. Khan, K. J. Berean, J. Z. Ou, N. Mahmood, T. Daeneke, K. Kalantar-zadeh

Journal of Materials Chemistry A **2017**, 5, 24223. DOI: 10.1039/C7TA07705J.

List of conferences:

1. **Surface acoustic wave exfoliation of piezoelectric stratified MoS₂**

M. Mohiuddin, N. Syed, T. Daeneke, K. Kalantar-zadeh, MRS Spring Meeting 2018, Phoenix, Arizona, USA.

2. **Electric field exfoliation of piezoelectric two dimensional materials**

M. Mohiuddin, Jianzhen Ou, K. Kalantar-zadeh, 4th International Conference on 2D Materials and Technologies (ICON-2DMAT) 2018, Melbourne, Victoria, Australia.

3. **Microcentrifugation exfoliation of layered MoS₂**

M. Mohiuddin, A. Zavabeti, T. Daeneke, K. Kalantar-Zadeh, International Conference on Emerging Advanced Nanomaterials (ICEAN) 2018, Newcastle, NSW, Australia.